NON-ORTHOGONAL V2X COMMUNICATIONS

ZHENHUI SITU

PhD

The Hong Kong Polytechnic University

2020

The Hong Kong Polytechnic University

Department of Electronic & Information Engineering

Non-orthogonal V2X Communications

Zhenhui Situ

A thesis submitted in partial fulfilment of the requirements

for the degree of Doctor of Philosophy

October, 2019

CERTIFICATE OF ORIGINALITY

I hereby declare that this thesis is my own work and that, to the best of my knowledge and belief, it reproduces no material previously published or written, nor material that has been accepted for the award of any other degree or diploma, except where due acknowledgement has been made in the text.

_____ (Signed)

Zhenhui Situ (Name of Students)

Abstract

In a cooperative intelligent transportation system (C-ITS), sensor-assisted vehicles share the collected data with each other through vehicle-to-everything (V2X) communications. This enables high-level applications such as safety-related service and provides a high-quality driving experience. However, the increasing number of intelligent vehicles leads to serious aggregated interference and congested communications. This increases the transmission latency and degrades the quality of service (QoS). To provide low-latency and reliable communications, non-orthogonal multiple access (NOMA) is recently advocated for V2X communications. By allowing multiple terminals to share the same time and frequency channel resources, NOMA improves the spectral efficiency and reduce the transmission latency, especially for a high-dense network. However, the overlapping of signals from multiple users introduces new challenges to the receiver design. This thesis exploits NOMA operating in two basic V2X communication scenarios: information exchange in a two-way relay channel (TWRC) and message broadcasting. Two non-orthogonal technologies are investigated: physical-layer network coding (PNC) and multiuser detection (MUD). The major difference between PNC and MUD is the decoding objectives. PNC aims to decode the network-coded messages while MUD is to recover individual messages.

First, we study a TWRC operating with orthogonal frequency-division multiplexing (OFDM) modulated PNC and propose an inter-carrier interference

(ICI) aware approach that jointly achieves accurate channel estimation, signal detection, and channel decoding. In highly-mobile networks, the carrier frequency offsets (CFOs) due to high-speed motion will lead to ICI in OFDM systems. Moreover, the vehicular environment with time-frequency-selective channels further undermines accurate channel estimation for multiple users. It is also worth noting that the CFO that exists in OFDM-modulated PNC cannot be completely eliminated through CFO tracking and equalization as in conventional point-to-point transmissions. These critical issues can significantly increase the bit error rate (BER) at the receiver. To address these challenges, we first express the channel estimation, and detection and decoding as two optimization problems. Then the expectation maximization (EM) and the belief propagation (BP) algorithms are employed to resolve the two optimization problems, respectively. Simulation results verify that the proposed approach can efficiently mitigate the negative effect of ICI by exploiting both pilot and data tones in channel estimation, detection, and decoding.

The proposed ICI-aware approach is further implemented with software-defined radio (SDR). Experiment along a road-side environment was conducted on the campus. The V2X trial involved two types of nodes: terminals, which can be either vehicle or pedestrian, that aim to exchange self-information with each other, and a relay that is played by a road side unit (RSU). Each node was equipped with a universal software radio peripheral (USRP) platform for data transmission. The empirical results further verified that the proposed ICI-aware approach provides low BER and low latency compared with the conventional algorithm. Besides, the proposed scheme can decode both network-coded and individual messages. An interesting finding is that when the receiver fails to decode the network-coded messages, it is of strong possibility to recover the individual messages. This provides insights into our work on the MUD.

Broadcasting is very common in V2X communications. For instance, it

involves basic safety messages (BSMs) for safety applications and multimedia content for entertainment services. In urban areas, dense buildings obstruct the radio channel between vehicles in different road segments and non-line-of-sight (NLOS) propagation lowers the received power level. Therefore, messages that originate from adjacent roads (traveling in non-parallel directions) usually have weaker signals as compared with messages generated from vehicles on the opposite road segment (traveling in parallel directions). Besides, the high vehicular density leads to insufficient orthogonal channel resource and high interference. In this thesis, we propose to apply NOMA for V2X communications at the road intersection to enhance the spectrum efficiency and improve the package delivery ratio (PDR) performance. With NOMA, signals from more than one transmitters are decoded together and the interference from undesired users can be canceled once its message is obtained. This thesis studies two NOMA-based V2X communication schemes, namely, NOMA-V2X decoded by successive interference cancellation (SIC-V2X) and NOMA-V2X decoded by joint decoding (JD-V2X). Based on the tools developed in stochastic geometry, we derive and compare the PDR expressions for both NOMA schemes and the orthogonal multiple access (OMA) scheme. The results indicate that 1) both NOMA schemes outperform the conventional OMA scheme and the PDR of LOS/NLOS communications with two-user access increases by 51%/369%; 2) for four-user access, the proposed NOMA scheme shows 375% goodput enhancement as compared with the OMA scheme; and 3) the JD-V2X provides significant PDR enhancement compared with SIC-V2X in the high data rate regime.

Besides the tractable network model to analyze C-V2X broadcast performance operated with NOMA, the feasibility of applying NOMA to C-V2X communications is studied. Focusing on the PC5 sidelink interface that is enabled in the 3GPP Release 14 for direct communications, we discuss the im-

plementation of NOMA in the radio interface and propose two NOMA receivers based on SIC and JD techniques. Compared with the conventional C-V2X receiver operated with OMA, modifications are needed at the channel estimator, equalizer, and demodulator, as well as the inclusion of an interference canceler so that multiple users can be decoded from the overlapping signals. Besides, the proposed NOMA receivers support both single-antenna and multi-antenna systems, and the impact of the number of receiving antennas on the block error rate (BLER) is studied.

Overall, this thesis investigates non-orthogonal V2X communications. The research combines the concepts of NOMA and network coding to address the basic issues and new challenges from the increasingly high-dense vehicular networks. The algorithms proposed in this thesis are expected to provide insights into the development of ultra-reliable and low-latency V2X communications in future smart cities.

List of Publications

Journal papers:

1. Z. Situ, I. W.-H. Ho, T. Wang, S. C. Liew, and C.-K. Chau, "OFDM Modulated PNC in V2X Communications: An ICI-aware Approach against CFOs and Time-frequency-selective Channels," *IEEE Access*, vol. 7, pp. 4880–4897, Dec 2019.

2. L. Xie, I. W.-H. Ho, Z. Situ, L. Lu, and W. Lu, "Channel-Coded Physical-Layer Network Coding with OFDM Modulation," *IEEE Access*, vol. 6, pp. 22267–22280, Dec 2018.

3. Z. Situ, I. W.-H. Ho, X. Xu, Y. L. Guan, and L. Xie, "Stochastic Analysis of Urban V2X Communications: Orthogonality versus Non-orthogonality," submitted to *IEEE Transactions on Vehicular Technology*.

Conference paper:

1. Z. Situ, I. W.-H. Ho, T. Wang, and S. C. Liew, "An ICI-aware Approach for Physical-layer Network Coding in Time-frequency-selective Vehicular Channels," in *IEEE Vehicular Technology Conference (VTC)*, Jun 2018.

2. Z. Situ, and I. W.-H. Ho, "NO-V2X: Non-Orthogonal Multiple Access with Side Information for V2X Communications," in *The 3rd EAI International Conference on Smart Grid and Innovative Frontiers in Telecommunications*, Apr 2018.

Acknowledgments

Now is the time for me to finish my thesis and Ph.D study. The past four years of study at the Hong Kong Polytechnic University (PolyU) is a precious treasure in my life. Along the way, I have met many smart and friendly people who supported me to accomplish my Ph.D degree. Thus, I would like to express my sincere and heartfelt gratitude to them.

I would like to give my sincerest gratitude to my brilliant, supportive, and inspiring supervisor Dr. Ivan Wang Hei Ho. I often wrote drafts that were long and difficult to understand, but he always carefully read them, corrected the mistakes, and gave valuable comments. He spared no effort to guide me and introduced many excellent professors to help me with my research. There is no word that can fully express my gratitude to him.

I owe thanks to Prof. Liew Soung Chang for sharing his superior knowledge and offering insightful feedback on my drafts. I learned a lot from the discussions with him and other group members at the Chinese University of Hong Kong: Lu Lu, Taotao Wang, and Lizhao You.

My deep gratitude also goes to Prof. Guan Yong Liang, my host supervisor during my visit to the Nanyang Technological University (NTU). I appreciate his support on my study and life to this day. I have benefited greatly from the discussions with him and other group members at NTU: Xiaoli Xu, Yumeng Gao, Xiaobei Xu, Md. Noor-A-Rahim, and Hieu Nguyen.

I would like to thank my co-supervisor, Prof. LAU Chung-Ming, Francis,

and research fellows in PolyU. I acknowledge the Research Committee of PolyU for financial support through the entire period of my study.

There are many colleagues at PolyU I want to thank: Lingfu Xie, Yu Xie, Tanuja Shanmukhappa, Elmer Magsino, Josyl Rocamora, Danista Khan, Xinyu Wang, Yuhao Wang, Jieshi Chen, Kanghao Jia, Kai Fung Chu, Kwok-Tung Sze, Junkai Chen, Shuangnan Liu, Qingqing Zhao, and Fanlu Mo.

Last but certainly not least, I am grateful to my family, including my parents, my sister, and my fiancee Peiya Li, for their constant love and support in completing this study. They are the most powerful motivations on my way forward.

Table of contents

List of figures

List of tables

List of abbreviations

1-D One dimensional

3GPP Third generation partnership project

5GAA 5G Automotive Association

AF Amplify-and-Forward

ANC Analog network coding

AODV Ad-hoc On-demand Distance Vector

APP A posteriori probability

AWGN Additive white Gaussian noise

BEM Basis expansion model

BER Bit error rate

BF-MAC Block-fading multiple access channel

BLER Block error rate

BP Belief propagation

BPSK Binary Phase Shift Keying

BSM Basic safety message

CAM Cooperative awareness message

CDF Cumulative distributive function

CE Complex exponential

CIR Channel impulse response

CNC Channel-decoding-network-coding

CP Cyclic prefix

CRC Cyclic redundancy check

CSI Channel state information

CSMA Carrier-sense multiple access

CUE Cellular user

C-V2X Cellular V2X

CFO Carrier frequency offset

C-ITS Cooperative intelligent transportation system

DF Decode-and-Forward

DMRS Demodulation reference signal

DSRC Dedicated short-range communications

EM Expectation maximization

ETSI European Telecommunications Standards Institute

EVA Extended Vehicular A model

F2FS Femto user to femto station

FD Full duplex

FFT Fast Fourier transform

GMEDS Generalized method for exact Doppler spread

GMP Gaussian message passing

ICI Inter-carrier interference

IFFT Inverse fast Fourier transform

ISI Inter-symbol interference

JD Joint decoding

LLR Log-likelihood ratio

LOS Line-of-sight

LTE Long Term Evolution

LTE-V LTE-Vehicle

MF Mean-frequency

MIMO Multiple-input multiple-output

MIMO-SM Multiple-input multiple-output spatial modulation

MMSE Minimum mean square error

MSC Modulation and coding scheme

MSE Mean square error

MUA Multi-user access

MUD Multiuser detection

MUST Multiuser superposition transmissio

NLOS Non-line-of-sight

NOMA Non-orthogonal multiple access

NORA NOMA random access

OFDM Orthogonal frequency-division multiplexing

OFDMA Orthogonal frequency-division multiple access

OMA Orthogonal multiple access

P2P Point-to-point

PDF Probability density function

PDR Package delivery ratio

PGFL Probability generating function

PNC Physical-layer network coding

PPP Poisson point process

PRR Packets receive ratio

PSCCH Physical sidelink control channel

PSSCH Physical sidelink shared channel

QAM Quadrature amplitude modulation

QoS Quality of service

QPSK Quadrature Phase Shift Keying

RA Repeat accumulate

RB Resource block

RF Radio frequency

RHS Right hand side

ROI Range of interest

RSRP Reference signal received power

RSU Road side unit

SC Superposition coding

SC-FDM Single-carrier frequency-division multiplexing

SCI Sidelink control information

SDR Software-defined radio

SIC Successive interference cancellation

SINR Signal-to-interference-plus-noise

SISO Single-input Single-output

SPS Semi-persistent sensing

TB Transport block

TDMA Time-division multiple access

TWRC Two-way relay channel

USRP Universal soft radio peripheral

UWA Underwater acoustic

V2I Vehicle-to-Infrastructure

V2N Vehicle-to-Network

V2V Vehicle-to-Vehicle

V2X Vehicle-to-Everything

VANET Vehicular Ad-hoc Network

VBLAST Vertical bell laboratories layered space-time

VUE V2V user

WSSUS Wide-sense stationary uncorrelated scattering

XOR Exclusive or

Chapter 1

Introduction

1.1 Background

The last decades have witnessed the rapid development of Vehicle-to-Everything (V2X) communications. Since Harry Flurscheim filed the first patent regarding a radio warning system for vehicles [1], the community kept developing V2X access technologies. V2X communications enable the information exchange between vehicles and any entities. It incorporates vehicular communications such as Vehicle-to-Infrastructure (V2I), Vehicle-to-Vehicle (V2V), Vehicle-to-Network (V2N) and so on. With the support of V2X communications, vehicles can share with each other the self information collected by the on-board sensors, and they cooperate with each other to offer a safe and high-quality driving experience. All together, they form a cooperative intelligent transportation system (C-ITS) to provide various services, such as smart navigation, infotainment, usage-based insurance, parking search, and reservation, etc [2–6].

As the cornerstone of these high-level applications, V2X is expected to offer low-latency and reliable communications in high-dense dynamic environments. Among diverse families of standards, two V2X access technologies attracted most of the research interest. They are dedicated short-range communications

(DSRC) and cellular V2X (C-V2X). DSRC applies the IEEE 802.11p standard to the PHY and MAC layers [7]. C-V2X is initially standardized by the third generation partnership project (3GPP) group in Release 14 to enable support from widely deployed Long Term Evolution (LTE) networks for V2X [8]. The 5G Automotive Association (5GAA), an alliance that gathers major telecom and automobile companies, adopted C-V2X for safety and cooperative driving as its blueprint [9].

However, the growing number of on-road wireless terminals leads to serious aggregated interference. This significantly degrades the communication quality and leads to high latency [10]. Furthermore, the problem deteriorates when the line-of-sight (LOS) path between the transmitter and receiver is obstructed by buildings or other obstacles [11], which is common in dense urban areas. Traditionally, multiple transmitters are supposed to occupy different time or frequency channel resources in an exclusive manner. A receiver aims to decode signals from transmitters one at a time. Such an access manner is called orthogonal multiple access (OMA). When multiple users are using the same channel resources, the receiver considers this as collision and only the user with the strongest received power can be decoded in most cases. The radio waves from other transmitters are regarded as interference. Such a problem can be mitigated by scheduling multi-user access (MUA), but the waiting time is fatal since the contact duration for V2X communications is short. For example, [12] showed that the average contact duration in an inter-bus communication network is only around 47 s.

To meet the V2X access requests in significant volume, recent emerging wireless technologies advocate non-orthogonal multiple access (NOMA). Compared with conventional OMA where radio resources are assigned in an orthogonal manner, NOMA allows multiple users to share the spectrum resources concurrently, thus achieving high spectral efficiency and low transmission la-

tency [13]. This thesis exploits the use of NOMA in V2X communications a natural form of network coding in the physical layer. Specifically, two non-orthogonal technologies, which are physical-layer network coding (PNC) and multiuser detection (MUD), are investigated for V2X communications.

1.1.1 Physical-layer network coding (PNC)

PNC allows the electromagnetic waves from multiple transmitters to superimpose at the same physical space (i.e., same time and frequency channel resources). Such non-orthogonal mixing of radio waves is regarded as a natural form of network coding in the physical layer. Instead of decoding the individual information, PNC receivers are designed to obtain the network-coded output of multiple terminals.

The most basic application of PNC in V2X communications is a data exchange in a two-way relay channel (TWRC) as illustrated in Fig. 1.1.

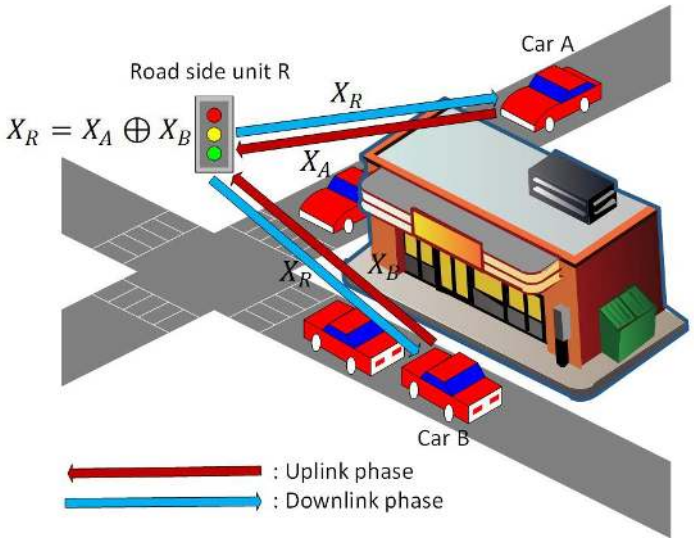

Figure 1.1: A TWRC that operates at a road intersection.

Two semi-automated cars A and B want to share with each other the traffic information recorded within their detection range. However, the radio channel between them is obstructed by buildings. The two cars thus need a road-

side unit R to forward the data for them. In traditional scheduling schemes, the concurrent transmission is not valid due to collision issue. Therefore, one node is allowed to transmit in one time slot. In the first time slot, car A sends package X_A to the relay, then the relay forwards X_A to B. Similarly, car B spends two time slots to send packages X_B to car A. This takes totally four time slots to finish the package exchange in such a TWRC. This is time-consuming and not suitable for time-critical nature of V2X communications.

A technique to reduce the latency by harnessing wireless interference is PNC. Specifically, PNC divides the data exchange into two phases: the uplink phase and downlink phase. In the uplink phase, two cars A and B simultaneously transmit signals X_A and X_B to relay R. Undergoing channels A and B respectively, signals X_A and X_B overlap at relay R. Then, R detects and decodes the overlapped signal to obtain the exclusive or (XOR) output of the two transmitted signals, $X_R = X_A \oplus X_B$. After that, relay R broadcasts X_R in the downlink phase. Finally, the two cars A and B recover their desired data with self information (e.g., car A can recover the data from car B via $X_B = X_A \oplus X_R$). The number of time slots required for the same data exchange is reduced from four to two, which indicates a 50% latency reduction.

1.1.2 Multiuser detection (MUD)

In conventional wireless communication systems, multiple terminals get rid of interference from each other by employing OMA schemes. Time-division multiple access (TDMA) and orthogonal frequency-division multiple access (OFDMA) are two examples of OMA schemes [14]. TDMA divides the channel into time subchannels. Several users share the same frequency channel, but they are assigned to transmit in different time slots. In OFDMA, multiple users are allocated with different subcarriers. They can transmit simultaneously

since the subcarriers are orthogonal to each other. Such orthogonal manner guarantees that the unwanted signals can be entirely separated from the desired signal. Thus, the modulation, encoding and decoding schemes can be designed based on single-user transmission. However, the resources allocation limits the maximum number of access users to guarantee the orthogonality.

In contrast to the traditional OMA schemes, NOMA allows multiple users to transmit concurrently on the same frequency channel by either code-domain or power-domain multiplexing. The signals undergo different radio channels and then overlap at the receiver. After that, receivers adopt MUD to extract the information from the target transmitter. Both PNC and MUD are employed to handle the superimposed signals, the difference is the decoding objectives. PNC aims to decode the network-coded information while MUD needs to acquire the individual information from multiple users.

Successive interference cancellation (SIC) is a multi-user decoder (MUD) technology that was widely considered in NOMA systems. It decodes multiple users in sequence according to the received signal strengths. The strongest user who has the highest received power level is decoded first while other users are regarded as interference. After a user is successfully decoded, the corresponding signal is subtracted from the superimposed signal for further decoding. In addition to SIC, another well-known MUD is joint decoding (JD). In JD, the overlapping signals of all transmitters are jointly decoded.

Fig. 1.2 shows the power regions of a two-user uplink additive white Gaussian noise (AWGN) channel [15]. The definitions of the notations can be found in Chapter 5. The power region that the two users can be successfully decoded with SIC is divided into two parts. The upper-left region indicates that user 2 is the strong user while the other region indicates that user 1 is the strong user. It can be observed from Fig. 1.2 that the power region of JD is larger than that of SIC. By allowing the power levels of the two users to be bal-

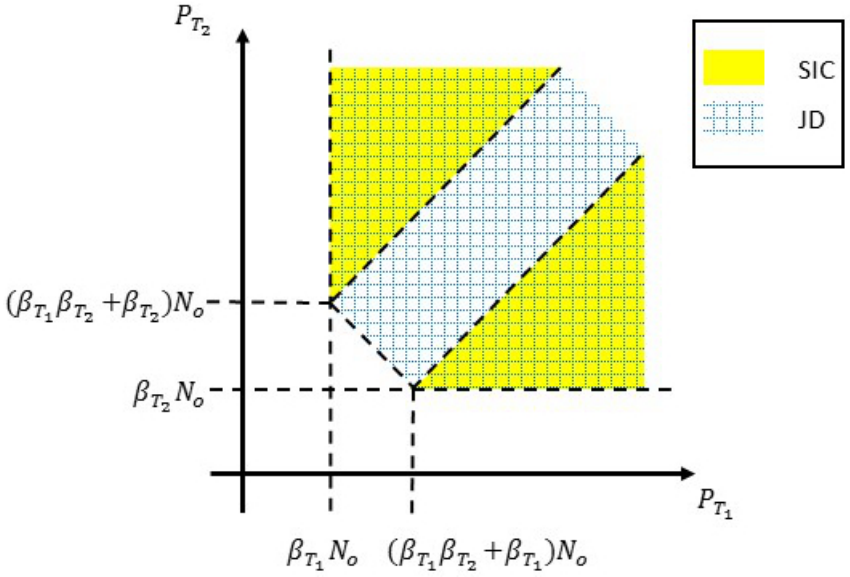

Figure 1.2: Power region of the two-user uplink AWGN channel.

anced, JD provides larger power region and higher probability to decode the two users. A similar conclusion was obtained in [16]. Since SIC decodes one user at one time, the complexity of SIC approximately shows a linear relationship to the number of users. On the other hand, the complexity for JD grows exponentially with the number of users [17]. Therefore, JD provides better performance than SIC at the cost of higher complexity.

1.2 Research Motivation and Contribution

The concept of accessing terminals non-orthogonally in vehicular networks can significantly reduce the transmission latency, especially in a high-dense dynamic environment for time-critical V2X communications. However, the superimposition of signals from multiple mobile terminals will create a lot of issues on channel estimation, signal synchronization, resource allocation, etc. To exploit the feasibility of non-orthogonal V2X communications, this thesis first studies a TWRC operated with PNC.

In both DSRC and C-V2X, OFDM was employed to modulate the trans-

mitted data. Different from the conventional point-to-point (P2P) communications, carrier frequency offset (CFO) is originated from imperfect local oscillators at the two end nodes and Doppler spreads are inevitable in PNC systems (two CFOs from the two end nodes are probably different and thus they cannot be completely eliminated). It varies the relative channel gain, which includes phase offset and power difference between the two end nodes and causes inter-carrier interference (ICI) among OFDM subcarriers [18]. Reference [19] revealed that the uncontrollable phase offset creates the XOR mapping ambiguity regardless of the noise. The minimum Euclidean distance between two points that belong to different XOR mappings does not only depend on the signal strength but also the relative channel gain [20]. In this case, ICI can lead to severe performance degradation. Operating in vehicular networks, these issues are further enlarged by the time-frequency-selective channels owing to the multi-path and high-mobility environment [21]. Most previous channel estimation algorithms for PNC such as linear interpolation [22] are designed based on the assumption of static networks. They are too simple and only provide reasonable performance under static network, but cannot track the rapidly changing channel conditions in V2X communications [21].

Basis expansion model (BEM) [23] is a powerful tool to capture the time-varying channel with a few modeling coefficients. The model facilitates channel estimation by significantly reducing the number of unknown parameters to be estimated. In addition, BEM-based estimator can track channel responses for not only desired signals but also ICI, thus providing the solution to tackle the negative effect of ICI. However, the previous BEM-based schemes used only orthogonal pilots to achieve channel estimation [23–29]. For PNC systems, multi-user access decreases the number of pilot tones for each user, thus degrading the estimation accuracy. With regard to this limitation, this thesis exploits not only orthogonal pilot tones but also non-orthogonal data tones to

achieve BEM-based channel estimation and decoding for PNC systems.

The objective of the first part of this thesis is to achieve accurate channel estimation and mitigate the ICI caused by CFO in signal detection and channel decoding in highly-mobile PNC channel. This thesis proposes an iterative scheme that can efficiently address the negative effects induced by time-frequency-selective channels and ICI in V2X communications. The salient features of the proposed algorithm are three-fold:

1. As far as we know, there is no previous investigation on time-frequency-selective channel estimation for PNC. However, double-selective channels must be considered in vehicular environments due to the multi-path nature and the Doppler effect. Based on the expectation maximization (EM) algorithm [30, 31], we firstly apply the BEM to convert the channel estimation task to solving a linear problem. Besides, the estimation is optimized by taking ICI and all tones into consideration.

2. Suffering from the detrimental effects of CFO and double-selective channels, the distance between two XOR mappings in the constellation can be very short. In this case, not only noise but also ICI will significantly affect the signal detection and channel decoding. We exploit the belief propagation (BP) algorithm [32,33] and an ICI-aware method to mitigate ICI in the detection and decoding phase.

3. Both the EM and BP algorithms can be enhanced with more number of iterations, the proposed method iterates between 1) and 2) to improve channel estimation, detection and decoding progressively. The simulation results show that the proposed approach can converge within three iterations.

Extensive simulation and experiments are conducted to evaluate the proposed approach and the results reveal that the proposed algorithm outperforms

the benchmark that simply treats ICI as Gaussian noise. In addition, although the proposed algorithm is designed for PNC systems, it can decode the individual information, which means that the approach can be employed as the MUD for NOMA systems. The results reveal that the proposed receiver is possible to acquire the individual information from one transmitter when the network-coded result cannot be decoded. Such an interesting finding leads to the next part of this thesis: message broadcasting in C-V2X communications.

Vehicles in C-V2X networks broadcast messages by direct communications. C-V2X supports both centralized and distributed resource allocations, referred to as modes 3 and 4 [34]. In mode 3, time-frequency resources are assigned by an eNodeB, which is an LTE base station in a centralized manner. By contrast, vehicles autonomously choose the radio resources for direct V2V communications in mode 4. A suitable MUD technique should be employed to guarantee acceptable NOMA performance in C-V2X communications.

For SIC, the certain power difference is required among multiple users to ensure that the interference from the weak users does not fail the signal decoding of the strong user. There is a rich body of papers on resource allocation and power control algorithms for SIC-based NOMA to guarantee the power difference [35–37]. Several recent works on NOMA in V2X communications also considered SIC-based NOMA [36, 38, 39]. They studied the power difference problem and proposed several algorithms to address the issue, which can be implemented in C-V2X mode 3 as a centralized control solution.

However, resource allocation and power control algorithms are not always available in V2X communications. For example, mode 3 is infeasible in areas without the coverage of eNodeBs. Besides, centralized control requires additional signaling overheads, which may be fatal for time-critical applications. For the delivery of relatively small-sized packages, centralized control may seriously degrade the transmission efficiency. In such cases, mode 4 that operates

in a distributed way is a better choice for V2X communications. However, the performance of NOMA operation in mode 4 uncoordinated network is unclear. To fill the gap, this thesis aims to apply NOMA to C-V2X operating in mode 4 and evaluate the performance. Stochastic geometry is exploited to capture critical performance metrics of the vehicular networks, such as the distribution of interfering vehicles, the shadow fading, and package delivery ratio (PDR), by taking the potential geometrical patterns of on-road units into consideration. To this end, this work provides a tractable network model for applying NOMA to mode 4 C-V2X in an urban area and proposes optimization methods to maximize the overall network goodput. The main contributions of the study are summarized as follows:

1. We develop a comprehensive network model with three multi-user access (MUA) schemes, including OMA, SIC-based NOMA, and JD-based NOMA, for C-V2X communications at a road intersection. This model characterizes the practical vehicular channel by considering the impact of obstacles. It enables tractable analysis for applying NOMA to C-V2X efficiently without requiring time-consuming Monte Carlo method.

2. The analytical results obtained from the network model are validated by extensive simulations, with practical settings. The results illustrate that the two NOMA schemes outperform the OMA scheme when the target user suffers poor radio channel, which might be caused by NLOS and long-distance transmission. The PDR, which is lower than 0.2 with the use of OMA, increases up to 0.55 and 0.75 with the use of SIC and JD, respectively. For the strong user with good radio channel, JD provides up to 20% and 30% PDR enhancement compared with SIC and OMA, respectively. Overall, both analytical and simulation results reveal that NOMA can significantly improve communication quality when the target

radio channel is poor.

3. Based on our analytical results, we propose a data rate optimization scheme to maximize the overall goodput, by balancing the data rate and PDR. The formulated optimization algorithm can be implemented very efficiently, which is feasible for time-critical V2X applications.

4. The implementation of NOMA in C-V2X communications is investigated. Based on the C-V2X physical layer as specified in the 3GPP Release 14, three receivers based on various receiving techniques, i.e., the conventioal OMA receiver, SIC-based NOMA receiver, and JD-based NOMA receiver, are exploited in non-orthogonal C-V2X communications. We demonstrate that NOMA can be easily implemented on the current C-V2X communications with minor modifications on the receiver.

1.3 Organization of the Thesis

The remainder of the thesis is organized as follows.

Chapter 2 introduces the basic knowledge of V2X communications, NOMA, PNC, and MUD. The related works are reviewed, from which we find the research gap to fill.

Chapter 3 discusses an ICI-aware approach that jointly achieves accurate channel estimation, signal detection, and channel decoding for OFDM modulated PNC systems in V2X communications. The channel estimation part and the detection plus decoding part are expressed as two optimization problems. They are solved with the EM and BP algorithms respectively.

Chapter 4 presents a testbed for non-orthogonal V2X communications. A TWRC, which is demonstrated in Chapter 3, is implemented using software-defined radio (SDR) [40]. The V2X trial involves vehicle, pedestrian, and road

side unit (RSU). Each node is equipped with a universal software radio peripheral (USRP) platform [41] for data transmission. The ICI-aware approach proposed in Chapter 3 is deployed for channel estimation, signal detection, and decoding.

Chapter 5 investigates a tractable network model to analyze the C-V2X communications operating in mode 4. A road intersection is considered and the communications involve both LOS and NLOS situations. The PDR of the C-V2X communications is derived according to the use of different MUD techniques: conventional OMA receiver, SIC receiver, and JD receiver. In addition, a data rate optimization algorithm is proposed to maximize the sum goodput of the three schemes.

Chapter 6 discusses the feasibility of applying NOMA to C-V2X communications. We show that the conventional OMA-based C-V2X receiver can be extended to decode multiple transmitters from the overlapping signals. According to the C-V2X communications as specified in 3GPP Release 14, both the SIC and JD based receivers are implemented and the performance is compared with the conventional OMA receiver.

Chapter 7 concludes the thesis and discusses the future work.

Chapter 2

Literature Review

This chapter is divided into four sections: the basic knowledge of V2X communications and NOMA is first presented; then we focus on a TWRC that operates with PNC, the issues caused by carrier frequency offsets (CFOs) and time-frequency-selective channels are investigated, and some existing solutions are introduced. After that, we discuss the feasibility of NOMA operating in C-V2X mode 4 and review some related works.

2.1 V2X access technologies

From 2005 to 2010, 802.11p was developed to provide suitable safety-related V2X communications against high relative speeds, high dynamics of information collection from nearby transmitters, substantial network load, and non-line-of-sight (NLOS) communications. In addition, 802.11p is expected to bridge a substantial transmission distance, which is up to 1 km. The 5.85-5.925 GHz band was allocated to 802.11p by both the US and Europe. 802.11p is basically derived from IEEE 802.11a for P2P V2X communications. Since the conventional Wi-Fi standards were designed for low-mobility networks, 802.11p provides improvements against the issues caused by the rapid motion

of vehicles.

Compared with DSRC 802.11p, C-V2X is a relatively new V2X access technology. It can benefit from the existing widespread LTE infrastructures. However, communications through infrastructural nodes potentially lead to high processing delay, and the LTE network is infeasible when a vehicle is not in the coverage area of LTE base stations. To cope with these issues, C-V2X supports direct V2X communications via the deployment of the sidelink channel over the PC5 interface. In 3GPP Release 14, two new sidelink transmission modes, which are mode 3 and 4, were proposed to support low latency V2X communications.

For both DSRC 802.11p and C-V2X, OMA is deployed for MUA. Specifically, OFDM and single-carrier frequency-division multiplexing (SC-FDM) are applied to modulate the signals by DSRC 802.11p and C-V2X, respectively. To avoid interference from undesired transmitters, DSRC 802.11p adopts carrier-sense multiple access (CSMA) [42] in distributed Vehicular Ad-hoc Networks (VANETs), and C-V2X applies semi-persistent sensing (SPS) in either centralized (mode 3) or distributed (mode 4) manner [34].

Broadcasting is the most basic communication scenario in V2X communications. For instance, all standards define safety-related messages for periodically broadcasting. In Europe, the European Telecommunications Standards Institute (ETSI) standardized cooperative awareness message (CAM) to broadcast the real-time vehicle data at a rate between 1 and 10 Hz [43]. In the US, DSRC applies the basic safety message (BSM) to share the vehicle information such as heading, speed, position with a predetermined frequency [44]. In vehicular networks, multi-hop forwarding is supported by diverse routing protocols such as Ad-hoc On-demand Distance Vector (AODV) [45]. The aforementioned TWRC is a special case of forwarding when the communication is bi-directional.

Operating in OMA, the overheads that originate from resource allocation to guarantee the orthogonality increase the transmission latency. When the resource channels cannot satisfy transmission requests in high-dense dynamic networks, the average waiting time increases to guarantee the orthogonality. Otherwise, concurrent transmission on the same resource channel causes collision in OMA. These issues are fatal to time-critical V2X communications. Thus, NOMA is advocated to decrease the latency for V2X communication by increasing spectral efficiency.

2.2 Non-orthogonal multiple access (NOMA)

NOMA can be broadly divided into two main categories: power-domain NOMA and code-domain NOMA. Appling a superposition coding (SC) strategy [46], power-domain NOMA superposes multiple users in the power domain and investigate the power difference among them. Employing user-specific spreading sequences, code-domain NOMA multiplexes the competing users in the code to obtain spares, low-density, and low-correlation properties. At the receivers, SIC and JD are two well-known MUD to decode the individual information. SIC is widely considered in the recent papers about power-domain NOMA [13,47–49] since it distinguishes and removes multiple users in sequence depending on different power levels.

A JD receiver, as discussed in the previous chapter, provides a higher PDR by allowing balanced power levels among multiple users. This strategy provides better decoding performance than SIC at the cost of higher computational complexity. PNC is a variant of NOMA that exploits network coding to enhance transmission efficiency. PNC aims to decode the network coded output of multiple users.

According to information theory, [15] revealed that superposition coding

based non-orthogonal multiplexing at the transmitter and SIC at the receiver outperforms conventional orthogonal-multiplexing and achieves the capacity region of the downlink broadcast channels. To further improve spectral efficiency, the integration of NOMA and MIMO technique is investigated [50–53]. For instance, MIMO-OMA and MIMO-NOMA were compared in [52, 53] and the advantages of MIMO-NOMA were illustrated analytically, which included both ergodic sum capacity and sum channel capacity. In additional to theory, power-domain NOMA was studied from the viewpoint of implementation. [54] considered practical NOMA schemes, which was named multiuser superposition transmission (MUST), for downlink transmissions with two users. [55] discussed several practical considerations such as signaling overhead, multiuser power allocation, user mobility, and SIC error propagation. An interesting finding was that the throughput gain of NOMA over OMA decreases as the mobility increases, and the minimum gain is around 22% when the velocity is 100 km/hr. For PNC, it was initially exploited in a TWRC and the power levels from multiple users were considered as balanced [56]. Different from power-domain NOMA where SIC was the most common MUD technique, PNC receivers were designed based on JD due to the balanced or near-balanced power levels. Table. 2.1 illustrates the PNC mapping in Fig. 1.1.

Table 2.1: PNC mapping

Symbol X_A from user A	Symbol X_B from user B	Mapping to PNC symbol X_R
1	1	1
1	-1	-1
-1	1	-1
-1	-1	1

In a PNC relay, the above mapping is first obtained through signal detection by comparing the received signal with the four possible combinations. This indicates that the symbol pair from the two users needs to be detected

jointly. For the channel decoder, there are three ways to decode the received symbols: 1) the network-coded symbol X_R is decoded; 2) symbols X_A and X_B are decoded separately; and 3) symbols X_A and X_B are decoded jointly, namely the symbol pair (X_A, X_B) is decoded [57]. No matter which scheme is deployed, the relay would broadcast the network-coded output in the downlink phase. An interesting point is that the individual information can be decoded if either schemes 2 or 3 is applied.

The next two sections reviews related works on applying PNC and MUD in V2X communications.

2.3 Physical-layer network coding (PNC)

Relay transmission is common in vehicular networks to cope with severe path loss due to NLOS and long-distance transmissions. It can achieve spatial diversity via node cooperation [58] and extends coverage without increasing transmission power. There are two common relaying strategies:

1. Amplify-and-Forward (AF): The relay node simply amplifies the received signal from the source and forwards it to the destination. This protocol converts the network into a large multiple-input multiple-output (MIMO) channel to achieve a beamforming gain, but the amplification of noise also degrades the communication performance.

2. Decode-and-Forward (DF): The relay decodes the message from the source, and then re-encodes it for the transmission to the destination. On one hand, this protocol can eliminate the interference from noise compared with AF. On the other hand, the relay may fail to forward the message when the source message cannot be decoded.

The idea of PNC was originally proposed in [56] and [59] as a subfield of

network coding [60,61]. It exploited networking to improve relay transmission performance. Similar to DF, PNC decodes the messages from the overlapping signals of multiple transmitters, but it aims to obtain the network-coded output. A simple version of PNC named analog network coding (ANC) was proposed in [62]. Similar to AF, ANC simplifies the weighted sum and forwards it. The easiest way to demonstrate the concept of PNC is a TWRC illustrated in Chapter 1. The TWRC operated with PNC indicates that the latency can be reduced by 50% compared with the conventional OMA scheme without network coding. In addition to the TWRC, PNC is feasible for other communications scenarios. For instance, [63] proposed nine PNC building blocks, with TWRC being one of them, and refer them as PNC atoms. Applying the proposed framework, a general network can be decomposed into the combination of the nine PNC atoms and achieves around 100% throughput enhancement compared with the conventional multi-hop scheduling.

VANET is a multi-hop network where relay transmissions are often seen. This attracts researchers to investigate the feasibility of applying PNC in V2X communications. The authors of [64, 65] studied the scheduling problem in PNC-based VANETs and proposed a MAC protocol named VPNC-MAC. The scheme includes setup and packet exchange phases to ensure reliable and efficient periodic beacon broadcasting. The feasibility of PNC in V2X communications was first studied in [66]. The major interest was the effect of CFO and it was found that in the worst case, PNC in V2X communications suffers only at most a 3 dB SINR penalty compared with conventional P2P communications. Since OFDM is widely used in the PHY layer of the standards belong to the 802.11 family, there are many prior works investigates the possibility of OFDM-modulated PNC [22, 67–70]. For instance, [67, 69] studied the synchronization problem due to the time difference of arrival between the two transmitters, [68] analyzed how the frequency-selective channels affect the

PNC performance. These issues are studied with the assumption of static networks. There is a limited study on channel estimation for PNC operating in high-speed motion.

OFDM divides the frequency band into multiple sub-channels, on which the data symbol is carried, to deal with non-flat fading. Theoretically, the fading in each sub-channel is flat when if the sub-channel is narrow enough. However, the vehicular motion leads to time-frequency-selective channels, and thus destroys the orthogonality and makes both channel estimation and decoding challenging [21, 71]. Admittedly, there exists a large number of papers that studied the performance of OFDM systems in double selective channels [21, 23, 71, 72]. Basically, the research interest can be divided into two parts: 1) channel estimation to accurately track the channel state information (CSI) against fast fading and CFO; and 2) robust signal detection or channel decoding against ICI and inter-symbol interference (ISI). To capture the rapid time-varying channels, there are three widely utilized statistical models: the classical Jake's model [73]; 2) the Markov models [74]; and 3) BEM [24]. BEM is employed in this thesis since it can reduce the number of parameters to estimate, thus the complexity can be reduced. There exists a large number of channel estimation algorithms that depended on these three models for P2P communications [75–77]. However, for OFDM systems operating in a non-orthogonal manner such as PNC, the impact of overlapping signals on the receiver design needs to be studied.

In terms of channel estimation in PNC, [78] customized a joint channel estimation and channel decoding framework for PNC systems. This work modeled the radio channels with two independent first-order Gauss-Markov processes [79]. The model represents the channels as finite-state Markov chains, which means that the current channel coefficient depends on the previous one. The correlations between two successive symbols were investigated via mes-

sage passing, this requires the perfect correlation coefficient. In addition, this work only considered single-carrier systems without ICI, this indicated that the channel model was not feasible for OFDM systems since the correlation between two subcarriers were not considered and the ICI induced by CFO could not be modeled.

For OFDM-based PNC, [80] proposed a blind channel estimation algorithm to capture frequency-selective channels through a non-redundant linear precoding at the two end nodes. The channels were assumed to be constant over a certain period. Thus, the temporal correlation was not studied. The authors of [22] adopted time-orthogonal (time non-overlapping) training symbols and pilots for the two end nodes. In this case, the channel estimation problem in PNC is reduced to that of traditional communication systems since the two channels are estimated separately. One problem is that the time-frequency resources assigned as either training symbols or pilots increases as the number of terminals ascents. A low-overhead channel precoding system was proposed for mobile lattice-coded PNC in [81]. Without the reference signal, the proposed scheme uses only temperature-compensated oscillators to achieve accurate channel alignment. However, the approach only considered single-path channel estimation and the ordinary walking speed in the conducted experiment was to low for V2X communications.

These above works did not consider channel estimation under time-frequency-selective channels. It is uncertain whether the prior channel estimation schemes for P2P communications [75–77] are feasible to estimate the overlapped signal or not. The BEM model, which is exploited in this thesis, is normally utilized for the discrete-time channel impulse response (CIR). The BEM model represents the time-varying channel over a short period of time as the weighted summation of deterministic basic functions. Several bases have been proposed, including complex exponential (CE) basis [24, 25], polynomial basis [26, 27],

Karhunen-Loève basis [28], and discrete prolate spheroidal functions [29].

A common method to mitigate ICI induced by CFO is interference cancellation. Before channel estimation and signal detection, ICI is removed with the use of ICI coefficients and decoded data [82,83]. Therefore, channel estimation and decoding are assumed to be conducted under the interference-free situation. The cancellation can be further divided into hard and soft cancellations depending on whether the data information is obtained from a hard (binary value) decision or a soft (mean value) decision. In [18], PNC was investigated in an underwater acoustic (UWA) two-way relay channels. There were two assumptions considered for the UWA channels: 1) the path amplitude was fixed as a constant value; 2) with a Doppler rate representing the changing rate of the delay, the path delay follows a first order kinematic model. The ICI issue was mitigated by a Gaussian message passing (GMP) based channel equalization method.

In [84], the effect of CFO was discussed in depth and ICI was considered in the form of the a posteriori probability (APP). Even though the CFOs cannot be eliminated, the paper suggested that it can be mitigated via mean-frequency (MF) compensation. The ICI problem was further mitigated via a message passing algorithm. The performance under both flat fading and frequency selective fading were analyzed. However, these works focused on CFO but assumed the channel to be known (i.e., the issue of channel estimation was not addressed). [85] investigated the use of an expectation maximization-belief propagation (EM-BP) algorithm to track the phase offset on the target subcarrier caused by CFO under both flat fading channel and frequency selective channel. However, the ICI induced by CFOs was treated as additional noise. In addition, the paper only considered the CFO between the crystal oscillators of the transmitter and receiver without the effect of the Doppler effect.

Compared with previous works, this thesis takes both channel estimation under time-frequency-selective channels, and detection plus decoding under ICI into account. These two critical issues are addressed for PNC in vehicular environments.

2.4 Multi-user detection (MUD)

One research objective of this thesis is to employ NOMA for C-V2X communications operating in mode 4, in which the network is uncoordinated and vehicles independently select radio resources to broadcast messages. In this case, NOMA is operating in random access networks. For the prior research on NOMA, which usually refers to power-domain NOMA, requires coordinations with known CSI to investigate the power difference for multiple access. This is easy to implement in a centralized network where a BS that obtains the CSIs of the terminals in its coverage. Besides uncoordinated communications, several recent works that studied the performance of NOMA random access indicated that NOMA can be employed for uncoordinated transmissions [86–90].

Choi [86] applied NOMA to multi-channel ALOHA [91, 92] with multiple sub-channels and multiple power levels, and proved that the proposed scheme achieved higher goodput than the conventional OMA-based multi-channel ALOHA. A channel-dependent selection for sub-channel and power level was exploited to mitigate the high transmission power problem. The impact of the proposed scheme on the average transmission power in terms of the number of power levels was evaluated by an upper-bound on the average transmission power. Seo et al. [87] studied NOMA random access (NORA) with multiple levels of target power based on channel inversion. This enabled that the received power at the BS can be one of the two target values to guarantee the power difference for SIC Compared with conventional random access, the

proposed scheme improved the maximum goodput from 0.368 to 0.7. NOMA random channel access with Rayleigh fading channel has been investigated in [88]. The authors of [89] studied the maximum sum rates of slotted ALOHA with two SIC receivers: ordered SIC and unordered SIC. Ordered SIC means that packets are decoded according to the order of the received power levels, and unordered SIC indicates random decoding order. The study was based on the assumption that the received SNRs follow exponential distribution. It revealed that the transmission probability and the encoding rate should be adaptively adjusted according to the SNR so that the maximum sum rate can be achieved. Besides, the analysis indicated that ordered SIC outperformed unordered SIC. [90] considered not only SIC but also JD for random access. Simulations revealed that the two techniques showed similar performance over frequency-flat block-fading multiple access channel (BF-MAC), but JD provided higher outage-limited maximum goodput than SIC. Since NOMA was mainly studied for cellular networks, [86–90] focused on a single receiver with the assumption of unicast. However, for common broadcasting in V2X communications, the performance of multiple users within a certain region should be considered.

When applying NOMA to V2X communications, the characteristics of vehicles need to be captured and studied to ensure the feasibility of NOMA in vehicular networks. Di et al. [38, 49] applied NOMA to alleviate the performance degradation in terms of latency and packet reception probability caused by the high density of vehicles. Focusing on SIC-based NOMA, they proposed a scheme including both centralized sub-channel allocation and distributed transmission power adjustment for V2X broadcasting to minimize the latency and maximize the packet reception probability. The proposed algorithm was suboptimal since the formulated problem was NP-hard. Only simulation results were provided to evaluate the performance. In addition to [38, 49], the

recent research on NOMA in V2X communications focuses on resource allocation [36, 93–96].

Yoon et al. [93] exploited a resource allocation algorithm, which consisted of joint sub-channel assignments, user pairings, and power control, to minimize the total transmission power for all terminals in the network. The problem was described as a mixed integer linear program and tackled in three low-complexity steps. In [94], a resource allocation scheme for V2V broadcasting operated with NOMA was proposed with the goal of optimizing the packets receive ratio (PRR). The vehicles were divided into multiple groups, where the members shared the same RBs, according to the moving statuses. A vehicle was assigned with the same resource unless it changed the status. In [36], the authors considered heterogeneous vehicular communications consisting of V2V, V2I, and femto user to femto station (F2FS) links. SIC-based NOMA was exploited in vehicular networks and an optimized power allocation scheme was proposed to improve the goodput and reliability. Focusing on a downlink NOMA-enabled V2X network, [96] considered the resource allocation problem for both cellular users (CUEs) and V2V users (VUEs). A joint resource allocation scheme with weighted max-min rate fairness was proposed to satisfy the fairness and variety requirements of CUEs for data service. Besides, the scheme could guarantee the reliability of V2V links by imposing minimum SINR requirements on problem formulation.

The authors in [39] studied the dynamic cell association caused by the high vehicle mobility and dynamic communication environment. The paper deployed SIC-based NOMA and proposed an algorithm to jointly optimize the cell association and power control to maximize the long-term system utility. [47] considered that the strong user served as a relay for the weak user via exploiting the side information for interference cancellation. Similar concept was extended in [97] by considering multiple-input multiple-output spatial

modulation (MIMO-SM) and V2V networks. SM was originally derived from Chau and Yu's work in [98], where the receiver decodes the signals from different transmitting antenna. [97] indicated that the robustness of SM against the temporal and spatial effects of the V2V channel had been exhibit improved by NOMA-SM compared with vertical bell laboratories layered space-time (VBLAST). Di et al. [99] exploited a full duplex (FD) NOMA scheme operated in decentralized V2X networks. Specifically, V2X communications in both urban and crowded scenarios were studied by providing the corresponding exact capacity expressions. Approximate closed-form expressions with arbitrary small errors were provided to simplify the exponential integral functions. The numerical results indicated several interesting points: 1) NOMA power and Rician factor value lead to better capacity performance as the number of V2X terminals increases; 2) the channel noise and the FD self-interference determined the effect of FD-NOMA; and 3) FD-NOMA showed the best latency performance compared with other schemes.

Most of these prior works relied on centralized control and did not consider any mathematically tractable network model, the proposed algorithms can only be evaluated via time-consuming simulation. Besides, they primarily focused on SIC receivers without much discussion on JD-based NOMA. In light of the inadequacy, it is significant to obtain a tractable network model to study the feasibility and performance of NOMA in C-V2X communications operating in mode 4. A comprehensive study should consider not only SIC decoder, which is widely assumed in NOMA systems, but also JD decoder.

Chapter 3

An ICI-aware Approach against CFOs and Time-frequency-selective Channels

This chapter studies the TWRC illustrated in Fig. 1.1. Since the downlink phase can be considered as traditional broadcasting, this work focuses on the most challenging part: the uplink phase operating in a non-orthogonal manner.

We organize this chapter as follows. The first section describes the system model of the TWRC. We discuss the proposed method in terms of two parts: the channel estimation part and the detection and decoding part in the second section. Then, the third section analyzes the computational complexity of the proposed algorithm. After that, simulation results are presented and analyzed in the fourth section. The last section concludes this chapter.

3.1 System model

In this section, we first depict the mobile radio channels adopted for the two end nodes. Then the overlapping signal at the relay is discussed and we can see the negative effect of double-selective channels and CFOs. The third and fourth subsections study the impact of relative channel gain and ICI on PNC systems. Finally, the last subsection shows how the BEM transfers the complicated superimposed signals into a simple linear equation.

3.1.1 Time-frequency-selective channels

In V2X communications, the multi-path environment and high mobility of vehicles create a lot of complexity in the mobile radio channels. The transmitted signals are propagated through multiple paths and mingle at the receiver. And the signals from different paths experience different delay and path gain. The signals suffer from delay spread and the maximum delay can be up to hundreds of ns [100]. Under high speed, signals with different incident angles have diverse Doppler shifts, and the maximum Doppler frequency in V2X communications is around 1500 Hz [101]. Previous empirical channel models [100, 101] indicate that the consideration of double-selective channels in V2X communications is necessary. In this work, we assume that the signals from the two end nodes undergo two independent time-frequency-selective channels characterized by wide-sense stationary uncorrelated scattering (WSSUS) models [102]. Specifically, the time-variant impulse response can be described as

$$h_i(\tau_i, t) = \sum_{p_i=1}^{P_i} c_{p_i}(t)\delta(\tau_i - \tau_{p_i}), \tag{3.1}$$

where $i \in \{A, B\}$ is the label for the two end nodes, P_i indicates the total number of propagation paths with different delays. t means the time, $\delta(\tau_i -$

$\tau_{p_i}) = 0$ when $\tau_i \neq \tau_{p_i}$ and $\delta(\tau_i - \tau_{p_i}) = 1$ when $\tau_i = \tau_{p_i}$. For the p_i-th path with delay τ_{p_i}, we consider non-line-of-sight (NLOS) propagation and the complex channel gain $c_{p_i}(t)$ is modeled as a Rayleigh process that follows the Jakes' power spectrum [102] with maximum Doppler frequency f_{d_i}:

$$f_{d_i} = \frac{v_i}{c} f_c, \tag{3.2}$$

where c indicates the speed of electromagnetic waves, v_i is the relative velocity between the transmitter and receiver (e.g., high speed that is up to 100 km/hr), and f_c is the carrier frequency. In addition to the Doppler spread, we assume that the imperfection of the local oscillators used to generate the radio frequency (RF) at the two end nodes A and B causes frequency offset f_{δ_i}. The imperfect local oscillators and the rapid motion of vehicles make CFO inevitable in V2X communications.

3.1.2 Superimposed OFDM signals

According to the 802.11p standard, we consider OFDM modulated PNC for V2X communications. The source data S_A and S_B, which are binary data, is first channel encoded, interleaved, and mapped to the constellation via modulation (e.g., BPSK and QPSK). After that, we obtain channel encoded and modulated data X_A and X_B. The inverse fast Fourier transform (IFFT) will then change the modulated data from the frequency domain to the time domain. After adding the cyclic prefix (CP), the time-domain signals are ready to be transmitted. Here the number of subcarriers is M and the length of CP is G. An important assumption in this work is that we assume CP can successfully cover the maximum delay so that the ISI can be eliminated. This is practicable by setting the length of CP sufficient. Let the bandwidth be B and the sampling rate is configured to be $B = 1/T_s$, where T_s indicates the

sampling interval. The duration of one symbol is $T = (M + G)T_s$. One data frame contains L symbols. The transmitted time-domain baseband discrete signals from node i at the l-th symbol are represented as

$$x_i[q + G + (l-1)(M+G)] = \frac{1}{M} \sum_{m=-M/2}^{M/2-1} X_{i,l}[m] e^{j2\pi \frac{m}{M} q}, \tag{3.3}$$

where q is the time index within a symbol, and $X_{i,l}[m]$ is the modulated information mapped from binary bit to the constellation. After up conversion, propagating through the mobile radio channels described in (3.1), and down conversion, the baseband signals from the two end nodes A and B overlap at the relay R, and we can express it as follows

$$y(t) = \sum_{i \in \{A,B\}} (x_i(t) \otimes h_i(\tau_i, t)) e^{j2\pi f_{\delta_i} t} + n(t), \tag{3.4}$$

where $\otimes$ denotes convolution operation, $n(t)$ is the complex white Gaussian noise with zero mean and variance σ_t^2. In the following, we further consider the product of $h_i(\tau_i, t)$ and the CFO due to oscillator imperfection $e^{j2\pi f_{\delta_i} t}$ to be one single component $h_i(\tau_i, t)$. This is reasonable since the hardware frequency offset can be regarded as part of the Doppler spread without loss of generality and this helps to simplify the equation. By performing fast Fourier transform (FFT) operation, the frequency-domain signal on the l-th symbol is given by

$$\boldsymbol{Y}_l = \boldsymbol{H}_{A,l} \boldsymbol{X}_{A,l} + \boldsymbol{H}_{B,l} \boldsymbol{X}_{B,l} + \boldsymbol{W}_l. \tag{3.5}$$

Here we use bold capital letters to denote arrays (e.g., vector or matrix). The above equation contains three $M \times 1$ vectors, which are $\boldsymbol{Y}_l$, $\boldsymbol{X}_{i,l}$ and $\boldsymbol{W}_l$, and two $M \times M$ matrices, which are $\boldsymbol{H}_{A,l}$ and $\boldsymbol{H}_{B,l}$. $\boldsymbol{Y}_l$ and $\boldsymbol{X}_{i,l}$ include data information of M subcarriers. $\boldsymbol{W}_l$ contains the independent noise on each

subcarrier and the noise is zero mean with variance $\sigma_f^2 = M\sigma_t^2$. $\boldsymbol{H}_{i,l}$ contains the detailed channel gains for one symbol. The diagonal elements $\boldsymbol{H}_{i,l}[m,m]$ denote complex channel responses for desired signals on the target subcarriers, while other elements are coefficients for ICI. (the non-diagonal elements should be zero when there is no CFO). The frequency-domain impulse response from subcarrier k to subcarrier m can be interpreted as follows:

$$\boldsymbol{H}_{i,l}[m,k] = \sum_{p_i=1}^{P_i} \alpha_t(m,k,l,p_i)\alpha_f(k,p_i), \tag{3.6}$$

with

$$\begin{aligned} \alpha_t(m,k,l,p_i) =& \frac{1}{M}\sum_{q=0}^{M-1} c_{p_i}((q+G)T_s + (l-1)T) \times e^{j2\pi\frac{k-m}{M}q}, \\ \alpha_f(k,p_i) =& e^{-j2\pi k\Delta f\tau_{p_i}}. \end{aligned} \tag{3.7}$$

The impulse response is the summation of impulse responses from all paths. For each path, the impulse response is the product of $\alpha_t(m,k,l,p_i)$ and $\alpha_f(k,p_i)$. $\alpha_t(m,k,l,p_i)$ is the output coefficient of the signal on the k-th subcarrier to the m-th subcarrier at the l-th symbol. It reflects the time-varying characteristic. $\alpha_f(k,p_i)$ is a phase rotation caused by delay τ_{p_i}. It shows the frequency-varying characteristic. $\Delta f = 1/(MT_s)$ is the subcarrier spacing. If only one path exists, the channel is frequency-flat, which means the amplitudes of impulse responses on all subcarriers are the same. Multi-path leads to frequency-selective channels. $\boldsymbol{H}_{i,l}[m,k]$ with $m \neq k$ indicates ICI coefficient. Previous work on channel estimation [85] considers ICI as part of the noise, but here we attempt to achieve an ICI-aware scheme for channel estimation, detection and decoding to mitigate the negative effect of CFO.

3.1.3 Relative channel gain in PNC receiver

This subsection studies the impact of relative channel gain in XOR mapping. Fig. 3.1 plots the received constellation of the superimposed QPSK signals without neither noise nor ICI.

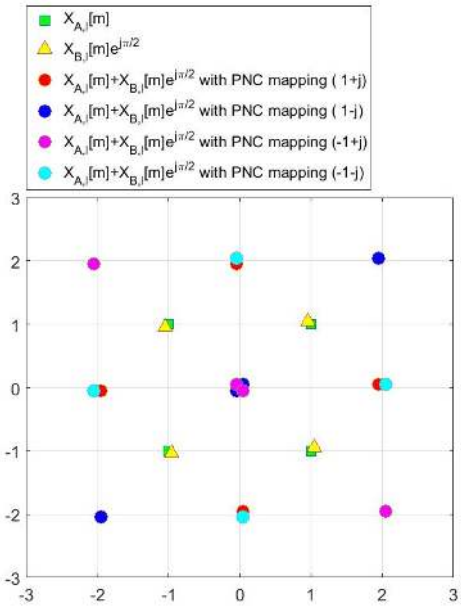

Figure 3.1: Constellation sample of PNC system (QPSK).

In this sample, the relative channel is $\frac{\boldsymbol{H}_{A,l}[m,k]}{\boldsymbol{H}_{B,l}[m,k]} = e^{j\frac{\pi}{2}}$. To highlight different XOR mappings, we purposely set the phase offset slightly larger than $\frac{\pi}{2}$. The four points that belong to XOR mapping $(1+j)$ overlap with the four points that belong to $(-1-j)$. In this case, the minimum distance d_{min} of two different XOR mapping is equal to zero even in the absence of both noise and ICI. Compared with either SNR or SINR, the power level related to the minimum distance (referred to as 'the power level' in the following), which is defined as $10\log_{10}(\frac{1}{4}d_{min}^2)$, can better illustrate the performance of PNC systems.

Fig. 3.2 and 3.3 show the power level under diverse relative channel gains. The sum power of the two users is fixed at 0 dBW and the relative channel gain

$\boldsymbol{H}_{A,l}[m,k]/\boldsymbol{H}_{B,l}[m,k]$ varies, then the minimum distance can be calculated and the power level is obtained. For BPSK modulation, the power level is only determined by the power difference regardless of the phase offset. It decreases as the power difference increases. In the region with a large power difference, the power level depends on the weak user whose power is relatively low. The power level is maximized when the amplitude ratio $|\boldsymbol{H}_{A,l}[m,k]/\boldsymbol{H}_{B,l}[m,k]|$ is equal to one. For QPSK modulation, the weak user determines the power level in the region with a large power difference as well. But phase offset causes serious power level degradation in the power-balanced region, where the amplitude ratio is between 0.5 and 2. In the near power-balanced region, either 4 degree phase offset from 84 degree to 88 degree or 0.12 amplitude ratio offset from 0.81 to 0.93 can lead to 10 dB power level degradation. The area where the power level is lower than -20 dBW is highlighted in Fig. 3.3. Therefore, XOR mapping is sensitive to the relative channel gain, which includes both the power difference and phase offset.

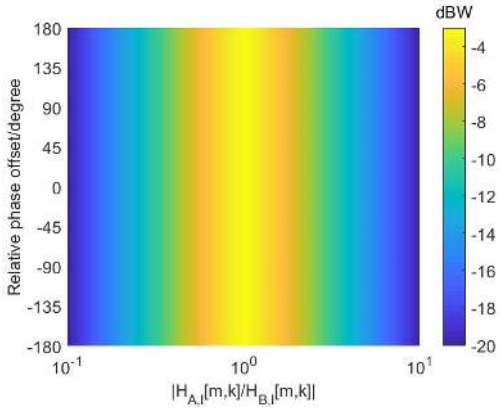

Figure 3.2: The power level under different relative channel gain (BPSK).

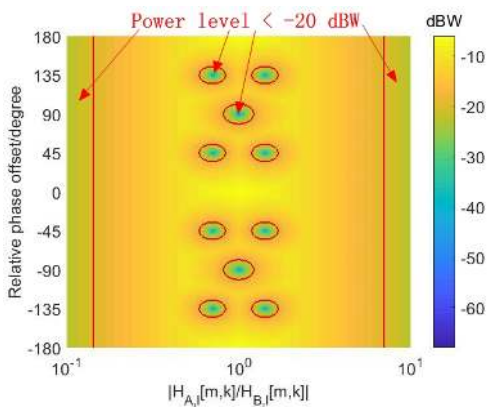

Figure 3.3: The power level under different relative channel gain (QPSK).

3.1.4 ICI in PNC receiver

The power of ICI is determined by the maximum Doppler frequency and the shape of the Doppler spectrum. For simplification, the two end nodes are assumed to share the same Doppler frequency and apply the Jakes' power spectrum. In addition, we only consider the ICI from two adjacent subcarriers since they dominate the ICI according to our study in [84]. According to Eq. (3.5) in [103], the power of ICI given normalized received power can be written as

$$P_{ICI} = \int_{-f_d}^{f_d} \underbrace{\frac{1}{\pi f_d \sqrt{1-(f/f_d)^2}}}_{\text{Jake's Doppler power spectral density}} \times \underbrace{[sinc^2(1-f) + sinc^2(-1-f)]}_{\text{ICI from adjacent subcarriers}} df. \tag{3.8}$$

The first component on the right hand side (RHS) denotes the Jake's power spectral density function. The second component represents the interference from two adjacent subcarriers. The result of (3.8) is plotted in Fig. 3.4. Similar to Fig. 3.2 and 3.3, the sum power is fixed at 0 dBW.

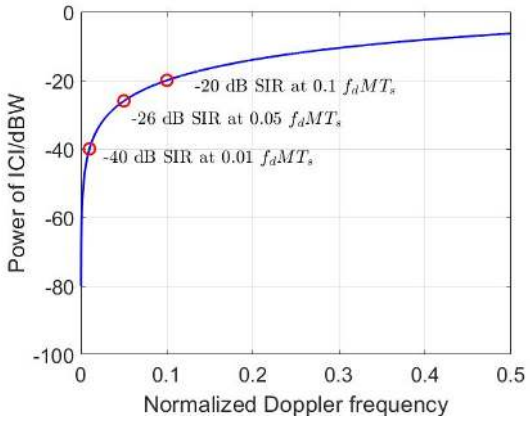

Figure 3.4: The power of ICI.

For low normalized Doppler frequency $f_dMT_s < 0.05$ in VANETs, the power of ICI is lower than -26 dBW, the corresponding SIR is 26 dB. The

power of ICI reaches -20 dBW when the normalized Doppler frequency is 0.1, and the corresponding SIR is 20 dB. Such SIR is high in conventional P2P communication systems. However, according to our study of relative channel gain in Fig. 3.3, -20 dBW ICI could be fatal to PNC systems. In the highlighted area in Fig. 3.3, ICI with $f_d M T_s = 0.1$ could already lead to error in XOR mapping.

Therefore, a robust PNC receiver in VANETs needs to accurately track the rapidly changing channel and provides ICI-aware estimation and decoding. To meet the requirement, BEM is applied in this work to facilitate the task.

3.1.5 Basis expansion model

Time-frequency-selective channels are inevitable in vehicular environment and challenging to estimate. It appears that the 802.11p pilot setup is infeasible to track the channel in rapid motion [21]. For PNC systems, each user is assigned with fewer pilot tones, which worsen the channel estimation. A strategy to address the issue of the insufficient number of pilots is to exploit the data tone to improve the estimation [78]. The study in the previous two subsections reveals that the data decoding is more challenging in PNC systems regardless of noise, the data with errors may deteriorate the channel estimation. This problem has never been studied in previous papers on BEM. In this work, we exploit the BEM to approximate the channels and it can transform (3.6) into a linear equation, which is much easier to solve. Specifically, the polynomial BEM (P-BEM) is assumed since it provides a better fit for low Doppler spreads. We can re-write the complex channel gain $c_{p_i}(t)$ of G_z OFDM symbols by applying P-BEM as

$$c_{p_i}(qT_s) = \sum_{g=1}^{G_z} \theta_{p_i,g} q^{g-1} + \xi[q], \tag{3.9}$$

where $\theta_{p_i,g}$ is a polynomial coefficient to establish the target channels, and $\xi[q]$ is the approximation error. Compared with estimating $c_{p_i}(qT_s)$ under all possible q, we can easily compute it once the polynomial coefficients are known. And thus, the output coefficient $\alpha_t(k, z, m, p_i)$ can be estimated according to (3.6). Here, we can completely reconstruct the impulse response matrix $\boldsymbol{H}$ if the delay spread τ_{p_i} is also known. Thus, the channel estimation is equivalent to calculating the delay spread τ_{p_i} and the polynomial coefficient $\theta_{p_i,g}$. The impulse response in (3.6) can be re-written after applying P-BEM as

$$\boldsymbol{H}_{i,l}[m,k] = \sum_{p_i=1}^{P_i}\sum_{g=1}^{G_z}\{e^{-j2\pi k\Delta f\tau_{p_i}}\sum_{q=0}^{M-1}(q-M+l(M+G))^{g-1}e^{j2\pi\frac{k-m}{M}q}\}\theta_{p_i,g}. \tag{3.10}$$

And we can further transform it into the linear form

$$\boldsymbol{H}_{i,l}[m,k] = \boldsymbol{\alpha}(m,k,l,i)\boldsymbol{\theta}_i, \tag{3.11}$$

with

$$\begin{aligned}
\boldsymbol{\alpha}(m,k,l,i) =& [\alpha_{p_1,1}(m,k), \alpha_{p_1,2}(m,k), ..., \alpha_{p_1,G_z}(m,k)\alpha_{p_2,1}(m,k), ..., \alpha_{P_i,G_z}(m,k)], \\
\alpha_{p_i,g}(m,k) =& e^{-j2\pi k\Delta f\tau_{p_i}}\sum_{q=0}^{M-1}(q-M+l(M+G))^{g-1}e^{j2\pi\frac{k-m}{M}q}, \\
\boldsymbol{\theta}_i =& [\theta_{p_1,1}, \theta_{p_1,2}, ..., \theta_{p_1,G_z}, \theta_{p_2,1}, ..., \theta_{P_i,G_z}]^T.
\end{aligned} \tag{3.12}$$

Here $[.]^T$ indicates transpose, and in the remainder of this chapter we use $[.]^H$ and $[.]^{-1}$ to denote hermitian transpose and inverse, respectively. Thus, we have demonstrated that the channel estimation problem for PNC in time-frequency selective channels can be considered as resolving a linear problem. And once the delay spread is known, both $\boldsymbol{\theta}^T = [\boldsymbol{\theta}_A, \boldsymbol{\theta}_B]$ and $\boldsymbol{H}$ can denote

the channel information, and thus they can be treated equivalently.

3.2 The proposed ICI-aware scheme

This chapter proposes an iterative method to jointly address two issues. The first one is to accurately estimate the complicated mobile radio channels with pilot and data tones. The second one is to detect and decode the transmitted data $\boldsymbol{S} = [\boldsymbol{S}_A, \boldsymbol{S}_B]^T$ given channel information $\boldsymbol{H}$ and received data $\boldsymbol{Y}$. $\boldsymbol{S}$ is a three-dimensional array containing element $\boldsymbol{S}_{i,l}[m]$. Similarly, $\boldsymbol{Y}$ is a two-dimensional matrix including element $\boldsymbol{Y}_l[m]$ and $\boldsymbol{H}$ is a four-dimensional array containing element $\boldsymbol{H}_{i,l}[m,k]$. Accordingly, we divide the system into two phases:

Channel estimation phase: Through exploiting the information in pilot and data tones, this phase aims to obtain the optimal channel information with the maximum a posteriori (MAP) probability $\hat{\boldsymbol{H}}_{MAP} = \arg\max_{\boldsymbol{H}} p(\boldsymbol{H}|\boldsymbol{Y}) = \arg\max_{\boldsymbol{H}} \sum_{\boldsymbol{S}} p(\boldsymbol{H}, \boldsymbol{S}|\boldsymbol{Y})$. This optimization problem is resolved by applying the EM algorithm and P-BEM.

Detection and decoding phase: With the MAP channel information $\hat{\boldsymbol{H}}_{MAP}$ calculated in the channel estimation phase, the goal of this phase is to find the MAP probability $p(\boldsymbol{S}|\hat{\boldsymbol{H}}_{MAP}, \boldsymbol{Y})$. The BP algorithm is used in this phase to mitigate the effect of ICI.

As can be seen, the detection and decoding phase requires the MAP $\hat{\boldsymbol{H}}_{MAP}$ calculated in the channel estimation phase. In turn, the calculation of $\hat{\boldsymbol{H}}_{MAP}$ requires the APP of $\boldsymbol{S}$, which is generated in the detection and decoding phase. The proposed scheme iterates between the two phases.

3.2.1 Channel estimation phase

This work aims to estimate time-frequency-selective channels. For time-varying channels, many previous works on channel estimation [75, 104] characterized the delay spread as discrete-time channel taps, and the taps can be calculated with preambles and pilots. In this work, we employ the same model, both preambles and pilots are separated from the two end nodes. Thus, we can apply the conventional methods [75] to calculate the delay taps. The complexity of the delay measurement algorithm is low, and thus feasible for time-critical applications. Notice that the availability of delay information is commonly assumed in papers on BEM-based channel estimation [76, 104] to focus on the analysis of BEM. Similarly, in this work, we focus on studying the proposed algorithm and assume that the number of paths and the corresponding delays are known in the simulation. For the experiment in the next chapter, the delay measurement algorithm [75] is implemented and the output is fed to the proposed scheme.

OFDM modulated systems divide the frequency spectrum into multiple subcarriers to carry information. Subcarriers inserted with known data are pilot tones and others are either data tones or null tones (e.g., the DC subcarrier is normally unused). The channel information $\boldsymbol{H}$ can be estimated more accurately by inserting more pilots, but this reduces the available bandwidth for data transmission. Owing to the time-frequency-selective channels and CFOs, it is difficult to track the channel information with pilots only. Our solution is to take advantage of data tones to optimize channel estimation. It can also further mitigate the negative effect of ICI.

In the EM algorithm, the transmitted data $\boldsymbol{X}$ is the latent (or hidden variable), the received signal $\boldsymbol{Y}$ is the observed data, and the channel information $\boldsymbol{H}$ is the hidden parameter. The auxiliary function in the EM algorithm is

used to calculate the expected value of the log-likelihood of the desired data given the current estimated channel. There are three stages as follows:

1. Initialization stage: find the initial channel information $\boldsymbol{H}^{init}$.

2. Expectation stage (E-stage): given the previous estimation $\boldsymbol{H}^{old}$, evaluate the auxiliary function

$$Q(\boldsymbol{H}|\boldsymbol{H}^{old}) = \sum_{\boldsymbol{S}} p(\boldsymbol{S}|\boldsymbol{Y}, \boldsymbol{H}^{old}) \log p(\boldsymbol{S}, \boldsymbol{Y}|\boldsymbol{H}). \tag{3.13}$$

3. Maximization stage (M-stage): optimize the channel parameters $\boldsymbol{H}^{new}$ by maximizing the auxiliary function

$$\boldsymbol{H}^{new} = \arg\max_{\boldsymbol{H}} Q(\boldsymbol{H}|\boldsymbol{H}^{old}). \tag{3.14}$$

For the initialization, only pilots are utilized to evaluate the channels. The procedure is similar to that of the M-stage by removing the data tones. Thus, we move to E-stage and offer more details to the calculation of the auxiliary function:

$$\begin{aligned} Q(\boldsymbol{H}|\boldsymbol{H}^{old}) &= \sum_{\boldsymbol{S}} p(\boldsymbol{S}|\boldsymbol{Y}, \boldsymbol{H}^{old}) \log p(\boldsymbol{S}, \boldsymbol{Y}|\boldsymbol{H}) \\ &= \sum_{\boldsymbol{X}} p(\boldsymbol{X}|\boldsymbol{Y}, \boldsymbol{H}^{old}) \log p(\boldsymbol{X}, \boldsymbol{Y}|\boldsymbol{H}) \\ &= \sum_{\boldsymbol{X}} p(\boldsymbol{X}|\boldsymbol{Y}, \boldsymbol{H}^{old}) \log p(\boldsymbol{Y}|\boldsymbol{X}, \boldsymbol{H}) + \sum_{\boldsymbol{X}} p(\boldsymbol{X}|\boldsymbol{Y}, \boldsymbol{H}^{old}) \log p(\boldsymbol{X}). \end{aligned} \tag{3.15}$$

The source data $\boldsymbol{S}$ is replaced with encoded data $\boldsymbol{X}$ because we care about the specific information contained in each subcarrier. The component $\sum_{\boldsymbol{X}} p(\boldsymbol{X}|\boldsymbol{Y}, \boldsymbol{H}^{old}) \log p(\boldsymbol{X})$ is irrelevant to the channel matrix $\boldsymbol{H}$. It thus can be neglected and removed in the M-stage. The auxiliary function can be

re-written as follows:

$$Q(\boldsymbol{H}|\boldsymbol{H}^{old}) \propto \sum_{\boldsymbol{X}} p(\boldsymbol{X}|\boldsymbol{Y}, \boldsymbol{H}^{old}) \log p(\boldsymbol{Y}|\boldsymbol{X}, \boldsymbol{H}), \tag{3.16}$$

where the component $p(\boldsymbol{X}|\boldsymbol{Y}, \boldsymbol{H}^{old})$ is the posteriori probability which can be calculated during the detection and decoding phase. To better analyze the auxiliary function, we re-write it as the summation of sub-auxiliary functions of individual symbols.

$$Q(\boldsymbol{H}|\boldsymbol{H}^{old}) = \sum_{l=1}^{L} Q(\boldsymbol{H}_l|\boldsymbol{H}_l^{old}). \tag{3.17}$$

The global auxiliary function is equivalent to the summation of multiple sub-auxiliary functions and the sub-auxiliary functions for individual symbols can be evaluated based on their corresponding posteriori probability $p(\boldsymbol{X}_l|\boldsymbol{Y}, \boldsymbol{H}^{old})$.

We prove in Section III that the channel information $\boldsymbol{H}$ is equivalent to the P-BEM coefficients $\boldsymbol{\theta}$ when the delay spread is known, and we further assume that the delay taps are obtained in advance in this work. Thus, the maximization of $Q(\boldsymbol{H}|\boldsymbol{H}^{old})$ is equal to the optimization of $Q(\boldsymbol{\theta}|\boldsymbol{\theta}^{old})$. In the following mathematical derivation, the optimization problem is considered in a group consisting of multiple sub-auxiliary functions. This means channel estimation runs in each group, which including G_z successive symbols. For one group, the Q function, namely the auxiliary function, is equal to the sum of G_z sub-auxiliary function

$$\begin{aligned} Q(\boldsymbol{H}|\boldsymbol{H}^{old}) \propto & \sum_{g=1}^{G_z} \sum_{\boldsymbol{X}_g} \sum_{m=-M/2}^{M/2-1} p(\boldsymbol{X}_g|\boldsymbol{Y}, \boldsymbol{H}^{old}) \times \\ & \{-|\boldsymbol{Y}_g[m] - \sum_{i} \sum_{k=-M/2}^{M/2-1} \boldsymbol{H}_{i,g}[m,k]\boldsymbol{X}_{i,g}[k]|^2/(2\sigma_f^2)\}. \end{aligned} \tag{3.18}$$

Employing the P-BEM shown in (3.11), $\boldsymbol{H}_{i,g}[m,k]$ in (3.18) can be replaced with the P-BEM coefficient as follows.

$$Q(\boldsymbol{H}|\boldsymbol{H}^{old}) \propto \sum_{g=1}^{G_z} \sum_{\boldsymbol{X}_g} \sum_{m=-M/2}^{M/2-1} p(\boldsymbol{X}_g|\boldsymbol{Y}, H^{old}) \{-|\boldsymbol{Y}_g[m] - \{\sum_{k=-M/2}^{M/2-1} [\boldsymbol{\alpha}(m,k,g,A)\boldsymbol{X}_{A,g}[k], \boldsymbol{\alpha}(m,k,g,B)\boldsymbol{X}_{B,g}[k]]\}[\boldsymbol{\theta}_A, \boldsymbol{\theta}_B]^T|^2/(2\sigma_f^2)\}. \tag{3.19}$$

Then associated derivative of the Q function can be written as follows.

$$\begin{aligned}
&\frac{dQ(\boldsymbol{H}|\boldsymbol{H}^{old})}{d\boldsymbol{\theta}} \\
=&\sum_{g=1}^{G_z} \sum_{\boldsymbol{X}_g} \sum_{m=-M/2}^{M/2-1} p(\boldsymbol{X}_g|\boldsymbol{Y}, \boldsymbol{H}^{old})(\boldsymbol{Y}_g[m] - \\
&\{\sum_{k=-M/2}^{M/2-1} [\boldsymbol{\alpha}(m,k,g,A)\boldsymbol{X}_{A,g}[k], \boldsymbol{\alpha}(m,k,g,B)\boldsymbol{X}_{B,g}[k]]\}[\boldsymbol{\theta}_A, \boldsymbol{\theta}_B]^T) \\
=&\sum_{g=1}^{G_z} \sum_{m=-M/2}^{M/2-1} (\boldsymbol{Y}_g[m] - \{\sum_{k=-M/2}^{M/2-1} [\boldsymbol{\alpha}(m,k,g,A)\hat{\boldsymbol{X}}_{A,g}[k], \boldsymbol{\alpha}(m,k,g,B)\hat{\boldsymbol{X}}_{B,g}[k]]\}\boldsymbol{\theta}).
\end{aligned} \tag{3.20}$$

To optimize the above Q function, we make the associated derivative to be zero as shown in (3.21).

$$\sum_{g=1}^{G_z} \sum_{m=-M/2}^{M/2-1} (\boldsymbol{Y}_g[m] - \{\sum_{k=-M/2}^{M/2-1} [\boldsymbol{\alpha}(m,k,g,A)\hat{\boldsymbol{X}}_{A,g}[k], \boldsymbol{\alpha}(m,k,g,B)\hat{\boldsymbol{X}}_{B,g}[k]]\}\boldsymbol{\theta}) = 0. \tag{3.21}$$

$\hat{\boldsymbol{X}}_{i,g}[k]$ is the posteriori expectation of the transmitted data after decoding. Let $\boldsymbol{Y}_G$ contains the received frequency-domain data of a group. Since each group includes G_z symbols and each symbol contains M tones, $\boldsymbol{Y}_G$ is a $(MG_z) \times 1$

vector. $\boldsymbol{A}_G$ is a $\{MG_z\} \times \{(P_A + P_B)G_z\}$ matrix with row vector

$$\sum_{k=-M/2}^{M/2-1} [\boldsymbol{\alpha}(m,k,g,A)\hat{\boldsymbol{X}}_{A,g}[k], \boldsymbol{\alpha}(m,k,g,B)\hat{\boldsymbol{X}}_{B,g}[k]]. \tag{3.22}$$

Referring to (3.21), each element in $\boldsymbol{Y}_G$ has the corresponding row vector in $\boldsymbol{A}_G$. (3.21) can be simplified as

$$\boldsymbol{Y}_G = \boldsymbol{A}_G\boldsymbol{\theta} + \boldsymbol{\Xi}, \tag{3.23}$$

where $\boldsymbol{\Xi}$ is the estimation error vector due to noise and approximation error in (3.9). We can maximize the auxiliary function by finding the optimal $\boldsymbol{\theta}$ to minimize the error $\boldsymbol{\Xi}$. To this end, we use a minimum mean square error (MMSE) estimator to achieve the optimization. According to Eq. (26) in [105], the optimal $\boldsymbol{\theta}$ is calculated as

$$\boldsymbol{\theta}^{new} = (\boldsymbol{A}_G + \boldsymbol{\Sigma}_n(\boldsymbol{A}_G^H)^{-1}\boldsymbol{\Sigma}_{\boldsymbol{\theta}}^{-1})^{-1}\boldsymbol{Y}_G, \tag{3.24}$$

where $\boldsymbol{\Sigma}_n$ and $\boldsymbol{\Sigma}_\theta$ are two covariance matrices for noise and $\boldsymbol{\theta}$, respectively. Since we assume the noise on each subcarrier is independent, the diagonal elements in $\boldsymbol{\Sigma}_n$ are $2\sigma_f^2$ and other elements are zero. Similarly, all propagation paths are uncorrelated and thus $\boldsymbol{\Sigma}_{\boldsymbol{\theta}}$ is a diagonal matrix in which the k-th diagonal element is $E(|\boldsymbol{\theta}[k]|^2)$. In each iteration of the EM algorithm, the channel estimation result from the previous iteration is used to calculate $\boldsymbol{\Sigma}_{\boldsymbol{\theta}}$.

So far, we have demonstrated the E-stage and M-stage of the EM algorithm. In the initialization stage, we can easily remove the data tones in (3.21) and perform (3.24) to obtain the channel information with pilots only. Besides, the covariance matrix $\boldsymbol{\Sigma}_{\boldsymbol{\theta}}$ is considered as an identity matrix at the beginning.

ICI compensation and equalization are common in conventional OFDM

systems, but they are separated from the estimation of channel gains. Unlike the two methods, the proposed channel estimation takes ICI into consideration and evaluate the optimal P-BEM coefficient $\boldsymbol{\theta}$ to construct the channel matrix. Thus, it is ICI-aware channel estimation. After performing channel estimation, the obtained channel information $\boldsymbol{H}$ will be used to conduct detection and decoding.

3.2.2 Detection and decoding phase

Given the estimated channel information $\boldsymbol{H}$, the proposed scheme conducts detection and decoding to acquire the transmitted data. Specifically, signals on each subcarriers are first detected and the APP of encoded data is obtained. Consequently, the APP is passed to the decoder to calculated the APP of source binary data. It means that both soft signal detection and channel decoding are performed in the proposed scheme. When CFO exists, the received signal on one subcarrier suffers ICI from other subcarriers. Traditional systems perform ICI compensation or equalization in advance, then signal detection is conducted on each subcarrier independently. This work, by contrast, detects the signal by taking the ICI into account. To study the effect of ICI, we first construct a Markov network [32, 106] to represent the received signals on one symbol. Then, the sum-product BP algorithm is employed to conduct the inference to calculate the marginal probability of the transmitted data. After that, channel decoding is performed with the BP algorithm. The Markov network for signal detection is illustrated in Fig. 3.5.

As can be seen, factors $\boldsymbol{X}_{i,l}[m]$ on the upper row are hidden factors while factors $\boldsymbol{Y}_l[m]$ on the bottom row are observed factors. Each received signal $\boldsymbol{Y}_l[m]$ is connected to the corresponding subcarrier and two neighboring subcarriers. The reason why only three subcarriers are connected is that the

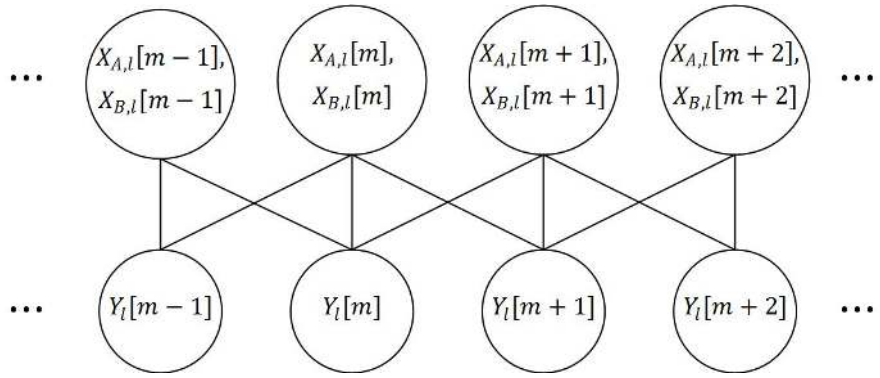

Figure 3.5: The Markov network for signal detection.

received signal on one subcarrier mainly depends on the desired signal on the corresponding subcarrier and ICI from two adjacent subcarriers according to our studies in [84]. Connecting more subcarriers cannot significantly improve the performance but exponentially increases the computational complexity. The joint APP of encoded data from three successive subcarriers can be calculated and stored in $\boldsymbol{Y}_l[m]$ as follows:

$$\begin{aligned} &p(\boldsymbol{X}_l[m-1,m,m+1]|\boldsymbol{Y}_l[m],\boldsymbol{H}_l) \propto \\ &\exp\{-|\boldsymbol{Y}_l[m]-\sum_i\sum_{u=m-1}^{m+1}\boldsymbol{H}_{i,l}[m,u]\boldsymbol{X}_{i,l}[u]|^2/2\sigma_f^2\}, \end{aligned} \tag{3.25}$$

where $\boldsymbol{X}_l[m-1,m,m+1]$ denotes $\{\boldsymbol{X}_{A,l}[m-1,m,m+1],\boldsymbol{X}_{B,l}[m-1,m,m+1]\}$ and $\boldsymbol{H}_l$ is $\{\boldsymbol{H}_{A,l},\boldsymbol{H}_{B,l}\}$. Thus, the factor $\boldsymbol{Y}_l[m]$ contains the APP $p(\boldsymbol{X}_l[m-1,m,m+1]|\boldsymbol{Y}_l[m],\boldsymbol{H}_l)$ of three successive subcarriers. The APP can be calibrated by performing the sum-product message passing algorithm. After that, marginalization is conducted so that the marginal probability hidden in factor $\boldsymbol{X}_l[m]$ is obtained. It turns out that the BP algorithm detects the received signal by considering ICI from two neighboring subcarriers.

Here we provide more details with respect to the BP algorithm. For each observed factor $\boldsymbol{Y}_l[m]$ in Fig. 3.5, it contains the self-information $p(\boldsymbol{X}_l[m-1,m,m+1]|\boldsymbol{Y}_l[m],\boldsymbol{H}_l)$ and passes the self-information to two adjacent subcar-

riers. The passed self-information is called message, and the self-information is not passed directly. For instance, when factor $\boldsymbol{Y}_l[m]$ passes a message to $\boldsymbol{Y}_l[m+1]$, since $\boldsymbol{Y}_l[m+1]$ considers subcarriers m, $m+1$ and $m+2$, $\boldsymbol{Y}_l[m]$ only needs to pass the information related to these three subcarrers. Because $\boldsymbol{Y}_l[m]$ contains information regarding subcarriers $m-1$, m and $m+1$, it needs to eliminate the information about subcarrier $m-1$ by performing marginalization. Let $\Psi_l[m]$ denotes the self-information in $\boldsymbol{Y}_l[m]$, the message generated by $\boldsymbol{Y}_l[m]$ and passed to $\boldsymbol{Y}_l[k]$ is indicated by $\zeta^l_{m\to k}$.

When the BP algorithm begins, messages are passed from the root down towards the leaves. In this work, the first message $\zeta^l_{1\to 2}$ is generated by $\boldsymbol{Y}_l[1]$ and passed to $\boldsymbol{Y}_l[2]$, then the shared variables in $\Psi_l[1]$ are kept while others are removed via variable elimination to obtain $\zeta^l_{1\to 2}$. After that, $\boldsymbol{Y}_l[2]$ updates itself to be the product of $\zeta^l_{1\to 2}$ and $\Psi_l[2]$. Then, $\boldsymbol{Y}_l[2]$ operates variable elimination and passes the new message $\zeta^l_{2\to 3}$ to the next factors $\boldsymbol{Y}_l[3]$. By continuously performing the same operation, the message is passed from the first factor to the last one. Consequently, the message is passed from the last factor back to the first one. When the bidirectional message passing is done, each factor updates itself as follows.

$$\beta_m = \Psi_l[m] \times \prod_{k \in Neighbor_m} \zeta^l_{k\to m}, \tag{3.26}$$

where β_m is the updated belief, which can be considered as the calibrated APP. After marginalizing the belief, the marginal probability of hidden factor $\boldsymbol{X}_l[m]$ is obtained as the signal detection output. The structure of the factor graph considers ICI by connecting neighboring subcarriers, then the BP algorithm can calibrate the APP by mitigating the effect of noise and ICI. The results are passed to the channel decoder to decode the source data, and the APP of encoded data can be further calibrated via channel decoding.

With the APP of encoded data obtained, this work employs a virtual decoder [107] to perform the channel-decoding-network-coding (CNC) process. For the relay R in PNC, it needs to decode the XOR output $X_R = X_A \oplus X_B$, and broadcasts X_R to the two end nodes in the downlink phase. Therefore, There are two ways to perform CNC: 1) the XOR APP is first calculated based on the output of signal detection, then the XOR output of the source data $S_R = S_A \oplus S_B$ is decoded and encoded for the downlink phase; 2) the channel decoding is performed based on the APP, which means that S_A and S_B are both decoded jointly. Then according to the decoding results, network coding and channel encoding are performed. With respect to [107], the two methods are called XOR-CD and MUD-CD respectively, and it was shown that MUD-CD outperforms XOR-CD with more than 2.5 dB SNR gain. But the complexity of MUD-CD is higher, it needs to handles sixteen possible combination values while XOR-CD has only four possible combinations given QPSK modulation.. In this work, MUD-CD is preferred since it does not only provide better performance but also the APP of data from the two end nodes, which is required in the channel estimation phase. Fig. 3.6 shows that all encoded data in a frame are connected to the virtual channel decoder to perform CNC based on MUD-CD.

In CNC, after operating channel decoding, both the improved APP of encoded data (X_A, X_B) and that of source data (S_A, S_B) are obtained. For the last iteration of the proposed scheme, the APP of source data (S_A, S_B) is used to run network coding and channel coding so that the downlink data is prepared for broadcasting. For other iterations, the APP of encoded data (X_A, X_B) is passed back for the channel estimation of the next iteration.

Since XOR is a linear operation, the virtual channel decoder can easily apply any linear channel codes such as LDPC code, lattice code, and repeat accumulate (RA) code. In this work, the RA code is employed, and the RA

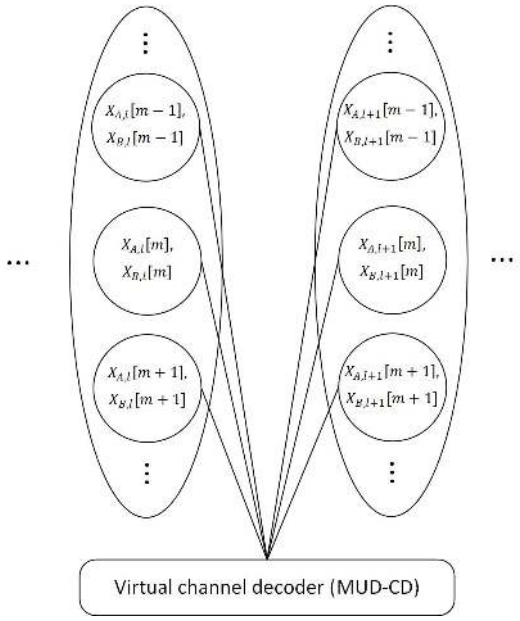

Figure 3.6: Virtual channel decoder based on MUD-CD.

decoder also applies the BP algorithm to decode the received data. However, any other linear channel codes are feasible in the proposed scheme. So far, the procedures of channel estimation, signal detection, and channel decoding have been introduced individually. Fig. 3.7 illustrates the architecture of the whole system.

The proposed method first estimates the P-BEM coefficient by constructing matrices $\boldsymbol{A}_G$, $\boldsymbol{\Sigma}_n$, $\boldsymbol{\Sigma}_\theta$, and $\boldsymbol{Y}_G$. The four matrices are discussed in (3.21) and (3.24). Then the full channel matrix $\boldsymbol{H}$ can be established according to (3.11), and the output is used for signal detection. Given the channel information and received signals, the APP of the encoded data is calculated and stored in factor $\boldsymbol{Y}_l[m]$. After that, sum-product message passing is implemented in each symbol individually and we can observe the forward messages $\zeta^l_{m\to m+1}$ and the backward messages $\zeta^l_{m+1\to m}$. After performing inference, marginalization is operated to obtain the marginal probability $p(\boldsymbol{X}_l|\boldsymbol{Y}_l, \boldsymbol{H}_l)$. This ICI-aware signal detection technique mitigates the negative effect of CFO, and then the APP is delivered to the virtual channel decoder for CNC. Channel coding can

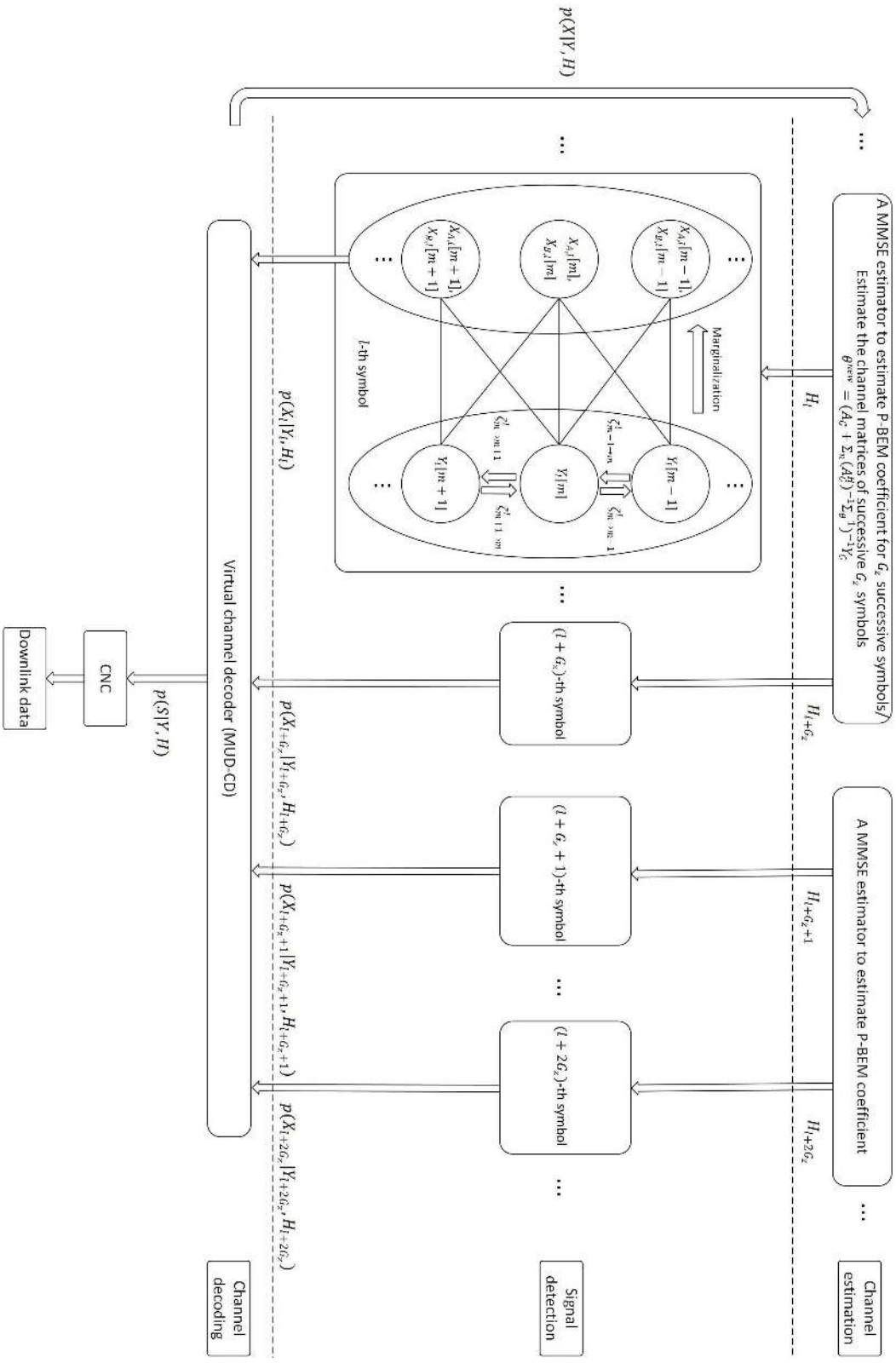

Figure 3.7: Factor graph of the proposed scheme.

significantly improve the reliability of the APPs $p(\boldsymbol{X}|\boldsymbol{Y},\boldsymbol{H})$ and $p(\boldsymbol{S}|\boldsymbol{Y},\boldsymbol{H})$. And thus we can apply the enhanced $p(\boldsymbol{X}|\boldsymbol{Y},\boldsymbol{H})$ to perform better channel estimation. The proposed system runs iteratively between the above phases and $p(\boldsymbol{S}|\boldsymbol{Y},\boldsymbol{H})$ is expected to converge at the true value. Then by simply performing network coding and channel encoding, the XOR output is prepared to be broadcasted in the downlink phase.

3.3 Complexity analysis

Here we analyze the computational complexity of the proposed scheme. We divide the proposed scheme into three parts: 1) The channel estimation part; 2) The signal detection part and 3) The channel decoding part. The complexity is summarized in Table 3.1. In addition to the ICI-aware approach, a conventional scheme (Conv) is provided for reference. The details of the algorithm are discussed in the next section. The complexity of Conv is close to the PNC prototype in [22] and the IEEE 802.11p standard.

Table 3.1: Complexity of one frame

Algorithm	ICI-aware	Conv
Channel estimation	$\mathcal{O}(MLG_z^2(M+P_A+P_B)(P_A+P_B)+$ $2ML(M+M^2G_z^2+P_AG_z+P_BG_z))$	$\mathcal{O}(2ML)$
Signal detection	$\mathcal{O}(12\Omega_A^3\Omega_B^3ML)$	$\mathcal{O}(\Omega_A\Omega_BML)$
Channel decoding	$\mathcal{O}(ML\Omega_A\Omega_B(2\Omega_A\Omega_B-1))$	$\mathcal{O}(ML\Omega_A\Omega_B(2\Omega_A\Omega_B-1))$

For the channel estimation part, the channel information is calculated via equation (3.24). Component $\boldsymbol{A}_G$ needs $\mathcal{O}(2m^2G_z)$ multiplications, where $\alpha(m,k,g,i)$ can be precomputed and stored. Similarly, component $\boldsymbol{\Sigma}_n$ can be precomputed and component $\boldsymbol{\Sigma}_\theta^{-1}$ is obtained from the previous iteration. We can see that there are three multiplications, one addition and two inverse operations in (3.24). By assuming the Moore-Penrose pseudoinverse of an $m \times n$

matrix that requires $\mathcal{O}(max(m,n)^3)$ computations, the product of an $m \times n$ matrix and an $n \times k$ matrix needs $\mathcal{O}(mnk)$ computations and the addition of the two $m \times n$ matrices requires $\mathcal{O}(mn)$ computations, the complexity of (3.24) is $\mathcal{O}(MLG_z^2(M+P_A+P_B)(P_A+P_B)+2ML(M+M^2G_z^2+P_AG_z+P_BG_z))$. The Moore-Penrose pseudoinverse is the most computationally expensive operation in the channel estimation part, but we can reduce the complexity by utilizing faster pseudoinverse algorithm, and the complexity can be further reduced by replacing the MMSE estimator with LS estimator.

For the signal detection part, based on the constructed graphical model shown in Fig. 3.5, this part has three steps: APP calculation, message passing, and marginalization. For one group containing G_z symbol, the APP calculation requires $\mathcal{O}(7ML\Omega_A^3\Omega_B^3)$ operations, where Ω_A and Ω_B are the alphabet size of modulation for two end nodes. For instance, $\Omega_i = 2$ when BPSK is applied and $\Omega_i = 4$ when QPSK is applied. Then, for the sum-product message passing algorithm, we need to compute the sum and product of APP, this step needs $\mathcal{O}(4ML\Omega_A^3\Omega_B^3)$ computations. The last step is marginalization and it takes $\mathcal{O}(ML\Omega_A^3\Omega_B^3)$ sum operations. Thus, the computational complexity of the signal detection part is $\mathcal{O}(12\Omega_A^3\Omega_B^3ML)$. The major complexity of the proposed scheme comes from the signal detection part since the factor graph connect three successive subcarriers as shown in Fig. 3.5. Connecting fewer subcarriers can significantly decrease the complexity. For instance, we can just connect one neighboring subcarrier depending on the direction of the Doppler shift or consider the data from one end node for two neighboring subcarriers [84]. By doing so, the order of Ω_A and Ω_B will be reduced from three to two.

Coming to the channel decoding part, the complexity of this part bases on the type of channel code and decoding algorithm we utilize. In this work we apply RA code and the complexity of is $\mathcal{O}(ML\Omega_A\Omega_B(2\Omega_A\Omega_B - 1))$.

We can see that the configuration affects the complexity. For example, a

large M significantly increases the complexity of the channel estimation, high-order modulation (e.g., 16-QAM) will make the signal detection dominates the complexity. We can control or reduce the complexity by adjusting the parameters in Table 3.1. For instance, we can see that the complexity of channel estimation shows a linear relationship to the square of the group size G_z^2. We will show in the next section (Fig. 3.8 and 3.9) that when G_z is reduced, the degradations in MSE and BER performances are minor.

Compared with the Conv algorithm, the proposed scheme shows higher complexity in the channel estimation and signal detection parts. However, the proposed scheme can perform individual channel estimation and signal detection in G_z successive symbols, thus the processing time can be significantly reduced with parallel computing hardware. For the implemented algorithms in MATLAB, the processing time of the proposed scheme is around 20 times of the Conv algorithm. This gap can be further decreased with optimized hardware.

3.4 Simulation results

In this section, simulation is conducted to evaluate the performance of the proposed scheme. The testbed is implemented with MATLAB and follows the 802.11p standard. Several input parameters are controlled, thus the proposed scheme is verified under different scenarios. Specifically, we consider the maximum Doppler frequency f_{d_i}, the SNR, the group size G_z and the number of iteration. Through controlling the four parameters, we observe the bit error rate (BER) of the decoded XOR data and the mean square error (MSE) of the estimated channel gain $c_{p_i}(t)$. We first show the MSE and BER results with different G_z and configure a reasonable G_z for the following simulation. Then, the convergence speed is studied by observing both the MSE and BER

after different numbers of iterations. After that, the proposed scheme and two benchmarks are compared under different f_{d_i} with both BPSK and QPSK modulations. In the following subsection, the simulation configuration is introduced.

3.4.1 Simulation configuration

In terms of the time-frequency-selective channels, two independent five-path Rayleigh fading channels are simulated for the two end nodes A and B. The empirical parameters of RTV-Urban Canyon and Canyon Oncoming cases in [101] are utilized to characterize the delay spread and the path power for the two end nodes. The tap powers of the first path for the two cases are recored as 0 dB for simplification. Thus, 100 ns delay and -3 dB tap power are additionally added to all paths for node B. For each path in both A and B, we assume that the fading spectral shapes are Jakes' power spectrum with the same normalized Doppler frequency $f_d M T_s$. Table 3.2 summarizes the fixed channel parameters for the two end nodes.

Table 3.2: Time-frequency-selective channel parameters

Path no.	Power (A)	Delay (A)	Power (B)	Delay (B)
1	0 dB	0 ns	-3 dB	100 ns
2	-11.5 dB	100 ns	-13.0 dB	201 ns
3	-19.0 dB	200 ns	-20.8 dB	301 ns
4	-25.6 dB	300 ns	-24.1 dB	400 ns
5	-28.1 dB	500 ns	-29.3 dB	500 ns

Besides the Doppler frequency, the hardware frequency offset is considered. According to our empirical measurement, we set $f_{\delta_A} = 600$ Hz and $f_{\delta_B} = -600$ Hz for the two end nodes. It indicates 0.00864 and -0.00864 normalized CFO in the simulation.

Following the 802.11p standard, the simulation adopts 10 MHz bandwidth and operates on the 5.9 GHz band. The proposed scheme only utilizes pilot tones to estimate the channel at the first iteration, the number of pilot tones should be not less than $P_A + P_B$ according to (3.24). However, the 802.11p standard, which assigns only four subcarriers as pilot tones, cannot meet the requirement. Thus, we modify the pilot and data pattern in this work. Specifically, each symbol contains 144 subcarriers, which includes 120 data tones and 24 pilot tones. The pilots are time-orthogonal for the two end nodes, 12 pilot tones are assigned to node A and the other half is assigned to node B. All pilots are uniformly inserted into the symbol. The length of CP is configured as nine, which can successfully prevent ISI in the simulation. Both BPSK and QPSK modulations are considered in the simulation. Note that the 802.11p standard uses convolutional code with coding rate 1/2, 2/3 and 3/4, which is feasible for PNC systems as it is a linear channel code. However, we employed the regular RA code with coding rate 1/3 [78] in this work since the decoder is optimized for PNC systems by jointly decoding multiple users.

Besides the proposed approach (ICI-aware), two benchmarks are simulated for comparison. One conventional benchmark (Conv) employs the linear interpolation [108] for channel estimation and regards ICI as noise in detection and decoding. Specifically, each symbol estimates the channel responses independently. Two successive pilot tones are utilized to evaluate the channel responses for the data tones between them. Another benchmark (ICI-com) applies the same P-BEM as the proposed algorithm to estimate the whole channel response matrix for desired signals and ICI coefficients. However, only pilot tones are used for channel estimation as in [104]. In addition, soft interference cancellation is performed at the beginning of each iteration, the channel estimation and decoding parts are thus conducted assuming the absence of interference. For the proposed scheme, the BP algorithm is performed

once in each signal detection and twice in each channel decoding. Table 3.3 summarizes the control variables considered in the simulation.

Table 3.3: Control parameters

G_z	2, 3, 4
Number of iteration	1,2,3,4,5
f_dMT_s	0.06,0.12
Modulation	BPSK,QPSK

3.4.2 Group size study

To select a reasonable G_z to balance the performance and computational complexity, we simulate the proposed ICI-aware approach with G_z from two to four. In this simulation, f_dMT_s is set to be 0.12 and BPSK modulation is considered. The MSE and BER results after five iterations are shown in Fig. 3.8 and 3.9. We can see that the MSE decreases as the group size G_z increases

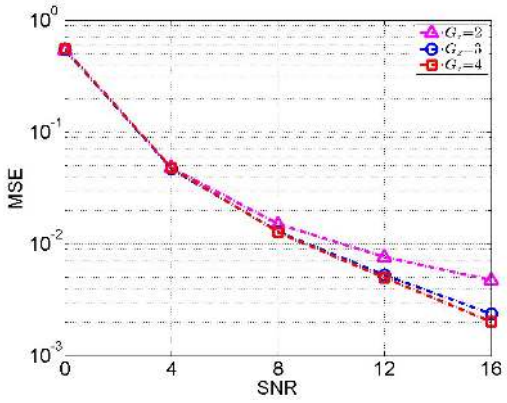

Figure 3.8: Comparison of MSE for different G_z.

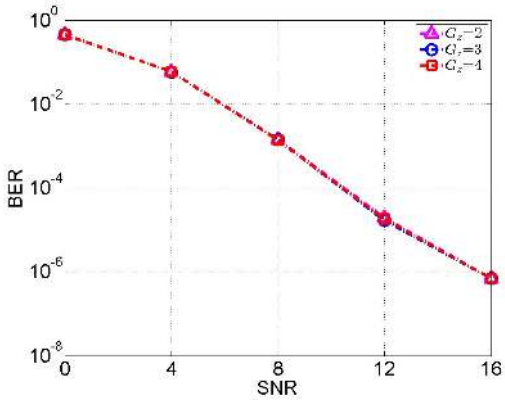

Figure 3.9: Comparison of BER for different G_z.

since a larger G_z indicates that a more complicated polynomial approximation can be constructed for fast time-varying channel. And the differences between the three curves widen when the SNR ascents. However, the gaps among them are small, especially in the low SNR regime. Compared with the MSE results,

the BER results of the three G_z values are extremely close. The three BER curves almost overlap together in Fig. 3.9. It reveals that performance with different G_z are similar. Considering the computational complexity analyzed in the previous section, we set the G_z to be two in the following simulations.

3.4.3 Convergence speed and initialization study

The proposed approach applies an iterative method for channel estimation, detection and decoding. The convergence speed is important since it determines the number of iterations required for convergence and affects the computational complexity. Applying the same configuration in the previous subsection, Fig. 3.10 and 3.11 show the simulation results.

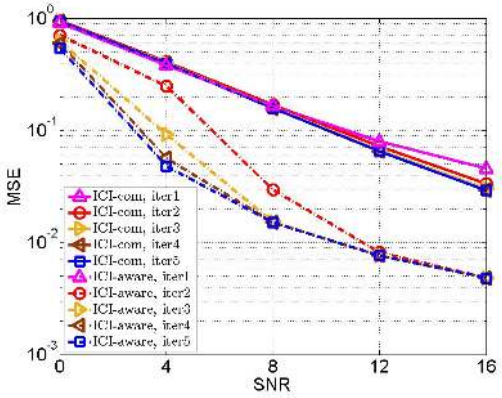

Figure 3.10: Comparison of MSE after different number of iterations.

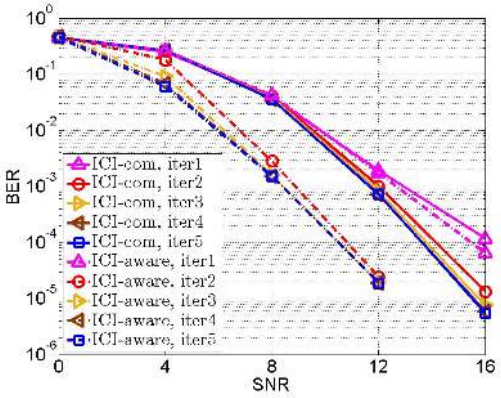

Figure 3.11: Comparison of BER after different number of iterations.

In Fig. 3.10, the MSE of the ICI-aware method becomes quite stable after three iterations. It can be seen that the proposed scheme converges quickly in the low (e.g., 0 dB SNR) and high SNR (e.g., 12 dB) regimes, even one iteration is sufficient to converge. The medium SNR regime requires more iterations to converge. The reason is that in the low SNR regime, the proposed scheme cannot estimate the channel since the noise is too strong. In the high SNR regime, the proposed scheme can efficiently evaluate the channel due to the

weak noise. For the proposed scheme, it can converge within three iterations even in the worst case for the SNR between 0 and 12 dB. Similar trend is observed in the BER results shown in Fig. 3.11. We thus confirm that the proposed scheme can converge shortly, three iterations is already enough for the medium SNR regime and one iteration is acceptable in the low and high SNR regimes. The results of the ICI-com method are illustrated for comparison. We can see that the ICI-com method shows much worse performance and the results after different number of iterations are quite close in the low and high SNR regimes. The reason is that the ICI-com method cannot efficiently evaluate the channel until the SNR reaches 12 dB. When the SNR reaches 16 dB, the ICI-com method can also converge after three iterations. Therefore, five iterations are sufficient to convergence for both the ICI-aware and ICI-com methods. We only show the results after five iterations in the remainder of this thesis.

3.4.4 Impact of velocity on BER and MSE

After studying the group size and convergence speed, this subsection aims to study the impact of vehicular velocity on BER and MSE. To highlight the effect of velocity, we consider high SNR at 24 dB and perfect local oscillators to mitigate the effect of noise and CFOs from oscillators. The results are demonstrated in Fig. 3.12 and 3.13.

The velocity varies from 10 to 1500 km/hr. According to (3.2), the corresponding normalized Doppler frequency is from 0.0008 to 0.118. The velocity has a greater influence on the Conv algorithm than the other two algorithms. In the considered velocity range, the BER of Conv increases around 10 dB while the BER of the two BEM-based algorithms increases less than 4 dB. For velocity lower than 500 km/hr ($f_d MT_s \leq 0.0393$), the MSE and BER of

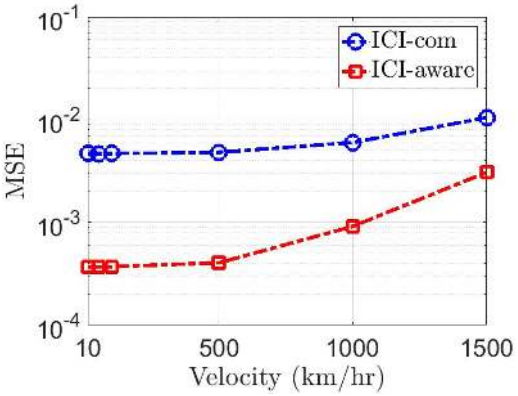

Figure 3.12: Comparison of MSE under different velocity.

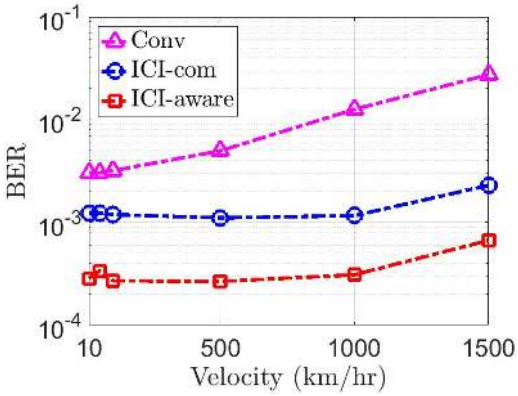

Figure 3.13: Comparison of BER under different velocity.

the two BEM-based algorithms show slight perturbation. For velocity higher than 500 km/hr, the gap between the ICI-aware and ICI-com algorithm becomes smaller. Generally, the proposed scheme shows the best MSE and BER performance and is robust against velocity.

3.4.5 Comparison with benchmarks

This subsection focuses on the comparison of the ICI-aware, ICI-com and Conv methods. The group size and the number of iterations are fixed to be two and five, respectively. Then simulations are conducted under different normalized Doppler frequencies and modulations. BPSK modulation is first considered, the MSE and BER results are illustrated in Fig. 3.14 and 3.15. We can see that the normalized Doppler frequency is configured as 0.06 and 0.12. Following the 802.11p standard, relative velocity 200 km/hr would only cause 0.0157 normalized Doppler frequency. Therefore, $f_d MT = 0.06$ and 0.12 are quite large numbers in vehicular networks and more than sufficient to verify the performance of the proposed approach. For the MSE, the Conv method does not evaluate the time-domain channel gain $C_{p_i}(t)$, only the MSE results of the ICI-com and ICI-aware methods are shown. It can be seen that the MSE of

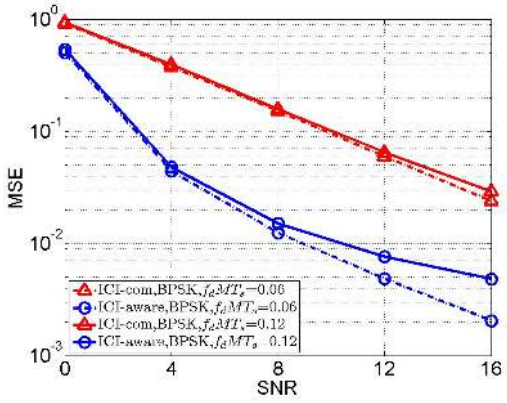

Figure 3.14: MSE results under different Doppler frequencies (BPSK modulation).

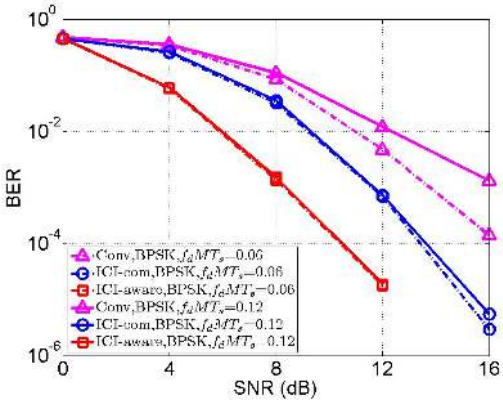

Figure 3.15: BER results under different Doppler frequencies (BPSK modulation).

the ICI-aware method is much smaller than that of the ICI-com method under different normalized Doppler frequencies. The MSE of the proposed scheme is even smaller than 0.01 when the SNR reaches 12 dB. Considering the BER results in Fig. 3.15, the proposed scheme outperforms the two benchmarks. Compared with the second-best method, it provides around 4 dB SNR gain in the medium and high SNR regimes. An interesting point is that the BER curves of the ICI-aware method under different normalized Doppler frequency are almost the same. The reason is that the proposed approach can efficiently estimate the channels with the two Doppler frequencies, the MSE results in Fig. 3.14 also proves that the estimation is accurate, and the BER is mainly dominated by noise. In general, the proposed scheme offers the best performance.

Most OFDM systems employ high-order modulation such as QPSK and 16-QAM. We also evaluate the proposed scheme under QPSK modulation. The corresponding results are shown in Fig. 3.16 and 3.17.

Comparing the results of BPSK and QPSK modulations, the MSE and BER curves of the three methods show a similar trend. The key difference is that QPSK modulation suffers around 6 dB SNR penalty. In the low SNR

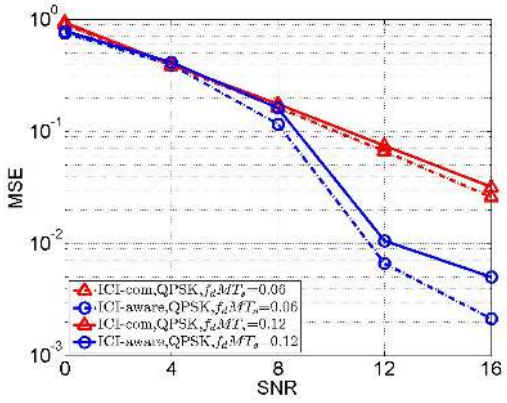

Figure 3.16: MSE results under different Doppler frequencies (QPSK modulation).

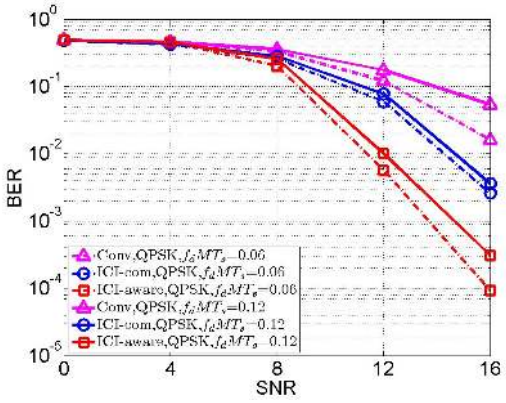

Figure 3.17: BER results under different Doppler frequencies (QPSK modulation).

regime (e.g., SNR is smaller than 8 dB), the MSE and BER results with QPSK modulation are considerably high. In the medium and high SNR regimes, the ICI-aware method outperforms the two benchmarks as with BPSK modulation.

So far, the simulation results verify that the proposed scheme provides the best performance compared with the two benchmarks. The SNR gain comes from the consideration of ICI and the employment of data tones in channel estimation, signal detection, and channel decoding. The fast convergence speed indicates that the computational complexity can be reduced by performing fewer iterations. For the high SNR regime, one iteration is acceptable for a five-path Rayleigh fading channel with 0.012 normalized Doppler frequency.

3.5 Summary

This chapter investigates the application of OFDM modulated PNC in V2X communications. The idea is to harness wireless interference to reduce latency and increase throughput in V2X communications. We aim to address two critical phenomena in this problem: the CFOs between multiple transmitters and receivers, and the time-frequency-selective channels in the vehicular environ-

ment. Our solution is to exploit an ICI-aware approach that jointly achieves accurate channel estimation, signal detection, and channel decoding against the detrimental effects caused by the two phenomena. The channel estimation and detection and decoding phases are converted into two optimization problems. The first one is solved by the EM algorithm while the second one is tackled by the BP algorithm. The effect of ICI is considered in the two phases and the channel matrix is re-established for decoding, thus we claim that the proposed overall algorithm is ICI-aware.

Simulations are conducted to evaluate the proposed scheme. We first study the tradeoff between performance and complexity of the proposed scheme and verify that the computational complexity can be reduced with minor performance degradation. Our results also indicate that the joint algorithm can converge within a small number of iterations (three to five). In the simulation that considers five-path double-selectively channels, the proposed scheme yields the lowest MSE and BER when compared with the benchmarks [104, 108].

Chapter 4

A Testbed for Non-orthogonal V2X communications

In the previous chapter, an ICI-aware approach for PNC systems is proposed to address the negative effect brought by CFOs and double-selective channels. The approach was evaluated by simulation. This chapter presents a V2X testbed to collect practical non-orthogonal signals so that the proposed approach can be further evaluated by experiment. Besides, this chapter investigates decoding not only the network-coded messages for PNC systems but also the individual messages for the conventional NOMA systems.

We organize this chapter as follows. In the first section, the software and hardware used to implement non-orthogonal V2X communications are introduced. The section also discusses several practical considerations, such as the frame format. Then, the next section discusses the two receiver schemes decoding the network-coded and individual messages, respectively. After that, the testbed for V2X field trials is shown in the third section. The experiment results are presented and analyzed. The last section concludes this chapter.

4.1 Implementation of non-orthogonal V2X communications with software-defined radio

The V2X field trials consist of three nodes, which are two transmitters and one receiver. This achieves the simplest non-orthogonal V2X communications where two users are sharing the same resource channel. The communications involve two steps:

1. Synchronization step: The receiver R broadcasts a beacon to the two transmitters A and B. After successfully identifying the beacon, the two transmitters prepare to transmit messages to the receiver.

2. Transmission step: The two transmitters transmit the message to the receiver using the same resource channel. Then, the receiver decodes the overlapping signals.

The testbed achieves the most basic non-orthogonal communication function and supports the two V2X communication scenarios in this thesis, which are information exchange in a TWRC and message broadcasting. The superimposed signals collected by the receiver can be regarded as either the network-coded messages or individual messages from two transmitters.

The communication functionality is implemented with SDR. The prototype is based on the implementation of PNC in [22]. It includes the hardware and software parts.

1. Hardware: The USRP N210 and daughterboard CBX-40 are used as radio hardware. Each USRP is connected to a laptop T470p for signal processing. In the experiment, the platform is operated at the 5.9 GHz band and the bandwidth is 5 MHz.

2. Software: The software consists of two parts: GNU radio [109] and MATLAB. Specifically, the baseband signal in the synchronization step is processed by the GNU radio that runs on the laptop T470p. We also use GNU radio for the two transmitters to transmit messages and the receiver to collect the overlapping signals in the transmission step. For comparison among different receiver schemes, the overlapping signals are collected by GUN radio and processed off-line with MATLAB.

Since the synchronization step is achieved with OMA, we focus on the transmission step operated in a non-orthogonal manner. After decoding and recognizing the beacon from the receiver, the two transmitters generate frames for transmission. Modulated with OFDM, the frame includes a preamble for synchronization and data symbols as discussed in the previous chapter. The preamble contains 160 time-domain samples, the two transmitters occupy either the first or the last 80 samples. In addition, orthogonal pilots can be used to estimate the delay spread. Thus, both the synchronization and delay spread estimation can be achieved with the traditional OMA-based algorithms. In our prototype, the algorithm in [110] is employed for synchronization and the ESPRIT method [75] to detect the number of paths and the corresponding delays.

4.2 Receiver design

The superimposed signals that collected from V2X field trials are processed with diverse receivers that implemented on MATLAB. In this section, the ICI-aware approach and the Conv method, which are introduced in the previous chapter, are employed for the off-line signal processing. In addition to the network-coded messages decoding, this chapter also considers the individual message decoding. This section studies four receiver schemes: 1) network-

coded message decoding with the ICI-aware approach; 2) individual message decoding with the ICI-aware approach; 3) network-coded message decoding with the Conv method; and 4) individual message decoding with the Conv method. The diagrams for the four receiver schemes are shown in Fig. 4.1 to 4.4.

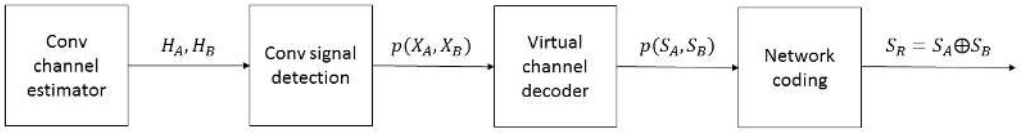

Figure 4.1: Scheme 1: Network-coded message decoding with the Conv method.

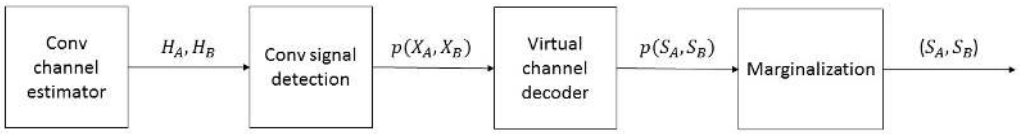

Figure 4.2: Scheme 2: Individual message decoding with the Conv method.

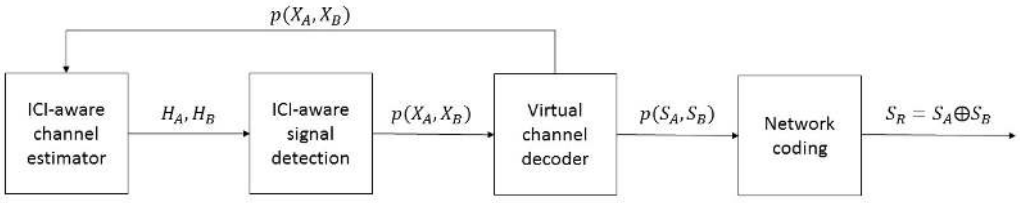

Figure 4.3: Scheme 3: Network-coded decoding with the ICI-aware approach.

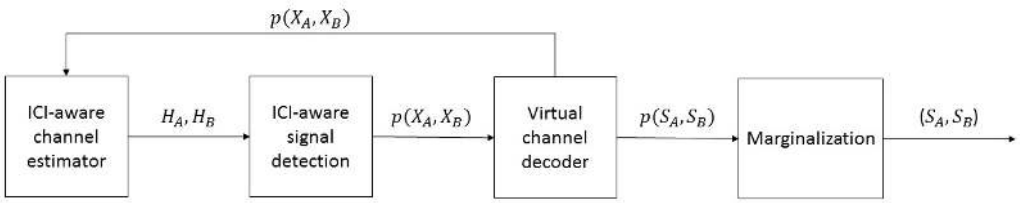

Figure 4.4: Scheme 4: Individual message decoding with the ICI-aware approach.

The previous chapter has discussed the channel estimation, signal detection, and virtual channel decoder blocks. Here we focus on the last block. For each scheme, the virtual channel decoder outputs the APP of the source data pair $p(S_A, S_B)$. For a PNC system, the APP is used to obtain the network-coded messages via network coding. For the traditional NOMA system that aims to obtain the individual information, we can replace the network-coding block with marginalization and decision block to acquire the individual source data S_A and S_B. Tables 4.1 and 4.2 illustrate the functions of the two blocks.

Table 4.1: Network coding

Output	Determination condition
$S_R = 0$	$p(S_A = 0, S_B = 0) + p(S_A = 1, S_B = 1) \geq$ $p(S_A = 0, S_B = 1) + p(S_A = 1, S_B = 0)$
$S_R = 1$	$p(S_A = 0, S_B = 0) + p(S_A = 1, S_B = 1) <$ $p(S_A = 0, S_B = 1) + p(S_A = 1, S_B = 0)$

Table 4.2: Marginalization and decision

Output	Determination condition
$S_A = 0$	$p(S_A = 0, S_B = 0) + p(S_A = 0, S_B = 1) \geq$ $p(S_A = 1, S_B = 0) + p(S_A = 1, S_B = 1)$
$S_A = 1$	$p(S_A = 0, S_B = 0) + p(S_A = 0, S_B = 1) <$ $p(S_A = 1, S_B = 0) + p(S_A = 1, S_B = 1)$
$S_B = 0$	$p(S_A = 0, S_B = 0) + p(S_A = 1, S_B = 0) \geq$ $p(S_A = 0, S_B = 1) + p(S_A = 1, S_B = 1)$
$S_B = 1$	$p(S_A = 0, S_B = 0) + p(S_A = 1, S_B = 0) <$ $p(S_A = 0, S_B = 1) + p(S_A = 1, S_B = 1)$

For the network coding block, it is based on the PNC mapping shown in Table 2.1. The network-coded output is $S_R = 0$ given either $(S_A = 0, S_B = 0)$ or $(S_A = 1, S_B = 1)$. And the output is $S_R = 1$ if either $(S_A = 0, S_B = 1)$ or $(S_A = 1, S_B = 0)$. The network coding block compares the sum probability

of the two sets of conditions to determine the final output. For individual messages decoding, the processing includes marginalization and decision. This is similar to the network coding block, the difference is that the target output is changed from $S_R = S_A \bigoplus S_B$ to (S_A, S_B).

Therefore, the ICI-aware approach that is proposed in the previous chapter is compatible with traditional NOMA systems by minor modifications.

4.3 Testbed setup

The testbed is on the Hong Kong Polytechnic University campus. A road-side environment is selected to conduct the experiment. Fig. 4.5 shows the map view of the testbed. The range of the movement of the vehicles is highlighted,

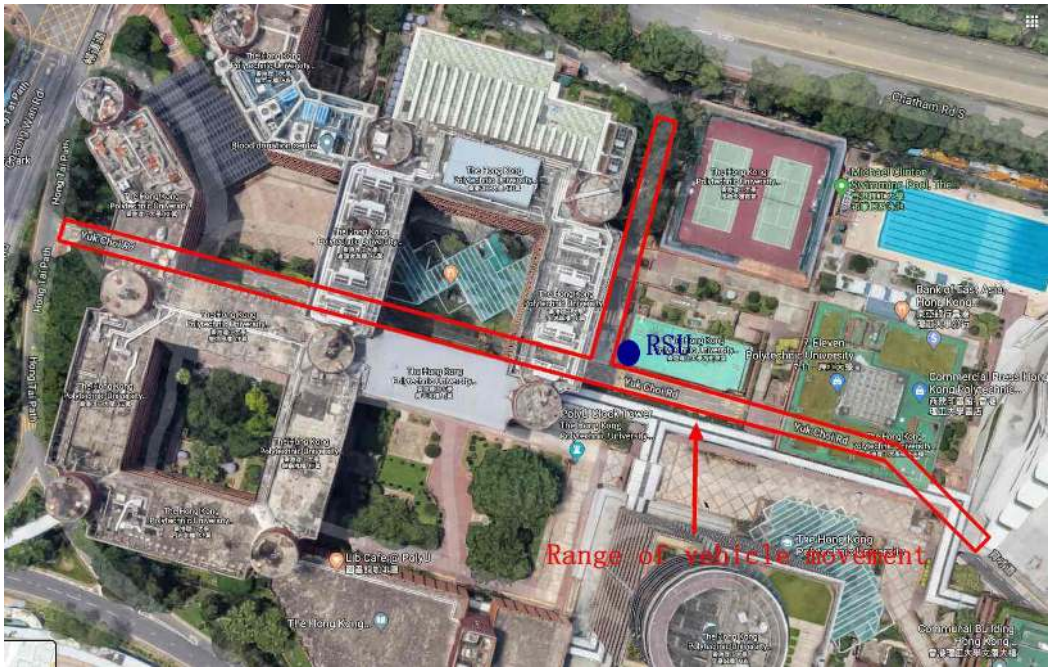

Figure 4.5: Map view of the testbed.

and the receiver is fixed at the road intersection.

The equipment for the experiment is shown in Fig. 4.6. We consider both the V2P and V2V communications through a road-side relay node and the snapshots of the two scenarios are shown in Fig. 4.7 and 4.8 respectively.

For the V2V scenario, two cars A and B go toward the road junction at a speed of around 20 km/hr. Meanwhile, they transmit data to the relay R simultaneously.

Figure 4.6: The V2X experimental setup.

Figure 4.7: The V2P communication scenario.

In the experiment, we apply the PNC prototype in [22] to collect the overlapped signal. The experiment is operated at the 5.9 GHz band and the bandwidth is 5 MHz. To meet the time-critical V2X communications, we apply BPSK modulation to reduce the computational complexity. Other configurations are the same as that in the simulation section. As discussed in the previous section, the relay R broadcasts beacons periodically to the two end

Figure 4.8: The V2V communication scenario.

nodes. After receiving a beacon, the two end nodes transmit the predefined data, which apply the same modulation scheme and channel code as that of the simulation, to the relay R simultaneously. In the uplink phase, the two end nodes transmit data with the same transmission power, regardless of the radio channel and background noise. Thus, there is no perfect power control in the experiment, and the received power from the two end nodes can either be balanced or unbalanced. This may degrade the performance since PNC is designed with the power-balanced assumption but can reduce the signaling overhead. The relay R receives and saves the raw signals from the two end nodes. We then use the proposed scheme and the Conv algorithm, which are implemented in MATLAB, to process the raw data.

4.4 Experimental results

We summarize the raw data collected from the two scenarios and process them with the Conv and ICI-aware algorithms. The two algorithms are evaluated in terms of the normalized throughput and delay. Compared with MSE and BER used in the previous chapter, the two performance metrics can better evaluate the proposed algorithm from the viewpoint of application layer. The normalized throughput is defined as the ratio between the number of recov-

ered frames and the number of transmitted frames in the uplink phase. The communication delay is the average number of time slots, which includes the time slots for re-transmission when transmission failure happens, to successfully transmit a frame in the uplink phase. Ideally, the minimum delay is one time slot per frame. Compared with the MSE of estimation and BER used in the previous chapter, the normalized throughput is a better performance metric to evaluate the proposed scheme from the viewpoint of the application layer.

According to the collected data, two taps were detected with 600 Hz Doppler frequency. The SNR varied from 0 to 12 dB. Besides the channel parameters, the experiment results were possibly affected by other uncertain factors. The normalized throughput is illustrated in Fig. 4.9.

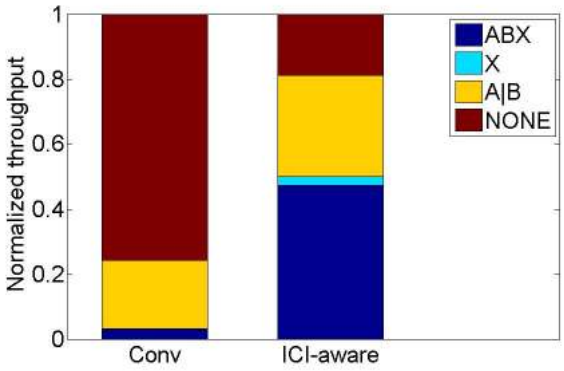

Figure 4.9: Normalized throughput of the experiment.

The normalized throughput can be divided into four partitions: 1) ABX: this partition denotes that the individual information of the two end nodes (X_A and X_B) and the XOR output ($X_A \oplus X_B$) are successfully decoded; 2) X: this partition means that only the XOR output is decoded; 3) A|B: this partition indicates that only the individual information of either user (X_A or X_B) is decoded; 4) NONE: the last partition means that no packet is successfully decoded. For PNC systems, the combination of the ABX and X partitions

represents the successful decoding rate.

Fig. 4.9 shows that the ICI-aware algorithm provides around 0.5 normalized throughput for the PNC system. By contrast, the normalized throughput of the Conv method is relatively low, which is less than 0.04. An interesting point is that the partition of A|B is fairly large. For the ICI-aware algorithm, the A|B partition occupies around 20% of the received packets. One reason could be that we did not perform power control in the experiment, it is possible that the received power of one end node is too low that the corresponding data cannot be decoded while the received power of the other user is sufficient to be successfully decoded. For PNC systems, the partition of A|B indicates failure since PNC systems only require the XOR output of the two users. But conventional NOMA [111] systems treat the individual information as important as well. This leads to our work on the individual message decoding in non-orthogonal V2X communications.

Communication delay is another significant criterion in time-critical V2X communications, thus the delay of the two algorithms are evaluated and shown in Fig. 4.10.

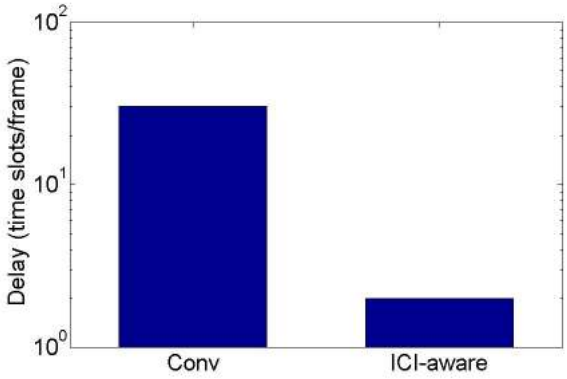

Figure 4.10: Communication delay of the experiment.

As can be seen, the delay of the ICI-aware algorithm is around 2 time slots/packet, while the theoretical minimum delay is 1 time slots/packet. By

contrast, the delay of the Conv algorithm is up to 30 time slots/packet, which is too high for time-critical V2X applications.

4.5 Summary

This chapter presents a testbed to conduct non-orthogonal V2X communications. The NOMA-based transmitters and receivers are implemented with SDR. According to the TWRC experiment enabled with PNC on the campus, the empirical results indicate that the ICI-aware approach proposed in Chapter 3 offers significant performance improvement on the normalized throughput and delay as compared with the conventional algorithm: the normalized throughput of the network-coded messages is increased from 0.04 to 0.5 and the delay is reduced from 30 time slots to 2 time slots. With minor modification, the proposed approach can also decode the individual messages. The partition that only one user can be decoded occupies around 20% of the entire throughput. This inspires us to work on the NOMA systems that focus on decoding the individual messages.

Chapter 5

Stochastic analysis of V2X communications: Orthogonality versus Non-orthogonality

This chapter studies the broadcasting performance in urban V2X communications at the road intersections. Different from network-coded messages as discussed in Chapter 3, this chapter focuses on decoding the individual messages. Based on the tools developed in stochastic geometry, we derived the PDR expressions for OMA, SIC-based NOMA and JD-based NOMA schemes.

The chapter is organized as follows. The network model, channel model, and receiver design are described in the first section. In the second section, the analytical expressions of PDR are derived and analyzed using stochastic geometry. A data rate optimization algorithm to maximize the goodput is also proposed in the second section. Then, the third section provides numerical results to validate the network model and evaluate the proposed algorithm. Finally, we summarize this chapter in the last section.

5.1 System model

The notations used in this chapter are summarized in Table 5.1.

Table 5.1: Notations

Notations	Definition
x_o	Distance between the receiver and the center point of the road intersection
x_{T_i}	Distance between the receiver and transmitter T_i
r	Communication range of interest
K	Number of users to decode for MUD
Ω_j	Distribution of target transmitters on street EW or NS ($j = 1$ or 2)
Ω	Distribution of target transmitters, $\Omega = \Omega_1 \cup \Omega_2$
$\Omega_{T_i}^{SIC}$	Set of possible transmitter combinations to decode user T_i with SIC
$\Omega_{T_i}^{JD}$	Set of possible transmitter combinations to decode user T_i with JD
λ	Density of interfering vehicles on each street (one sub-channel)
Φ_j	Distribution of interfering vehicles on street EW or NS ($j = 1$ or 2)
Υ	The set of distances between transmitters and receiver
α_j	Path loss exponent for vehicles on street EW or NS ($j = 1$ or 2)
ρ_j	Path loss for vehicles on street EW or NS ($j = 1$ or 2)
h_{T_i}	Rayleigh fading for vehicle T_i on either street EW or NS
P_{tx}	Transmitter power
P_{T_i}	Received power of transmitter T_i
$\mathcal{I}_j$	Aggregated interference from vehicles on street EW or NS ($j = 1$ or 2)
$\mathcal{R}_{T_i}^{max}$	Maximum achievable data rate of transmitter T_i
β_{T_i}	Minimum SINR to decode signal from transmitter T_i
N_o	Power level of thermal noise

5.1.1 Network model

To accurately capture the characteristic of V2X communications in urban areas, this chapter analyzes the performance of the proposed scheme using stochastic geometry [112]. This powerful tool had been widely used to model V2X communications including C-V2X [113,114]. We consider a V2X communication scenario at a road intersection as illustrated in Fig. 5.1.

All vehicles on the road intersection want to broadcast messages, which are either BSMs to share the local information such as position, heading, and speed

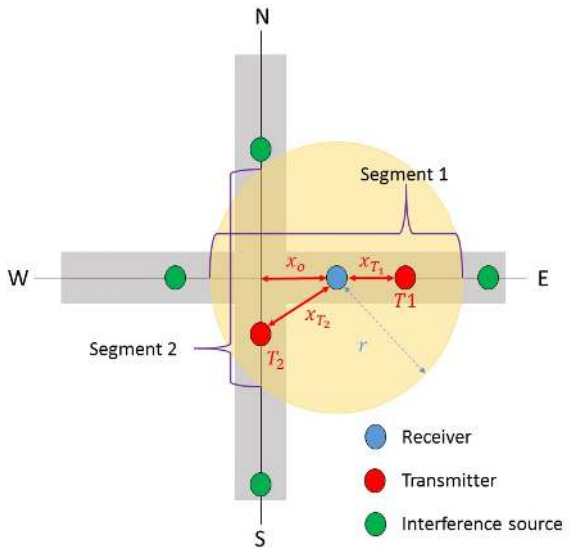

Figure 5.1: V2X communications at a road intersection.

[44] or multimedia content for infotainment service. We study the PDR of messages from transmitters within the communication range of interest (ROI) with radius r. Without loss of generality, the receiver is considered to be located on road segment E. The maximum distance between the receiver and the center point of the road intersection is assumed as x_o^{max}. We focus on the case that the ROI involves two users from the two streets NS and EW, which means $r \geq x_o^{max}$, and evaluate the PDR of message on the two segments. This chapter derives the PDR for MUD given an arbitrary number of target transmitters, based on which we can study the performance of MUD under different access scenarios. Let Ω_1 and Ω_2 denote the sets of target transmitters on streets EW and NS, respectively.

According to the standard, C-V2X applies single-carrier frequency-division multiple access and divides the time-frequency resource into multiple resource blocks (RBs). The RBs constitute sub-channels and subframes as illustrated in Fig. 5.2. One sub-channel is a group of RBs in the same sub-frame, it is used to transmit control information and data. According to the functionality, there are two types of transmissions: sidelink control information (SCI) for control

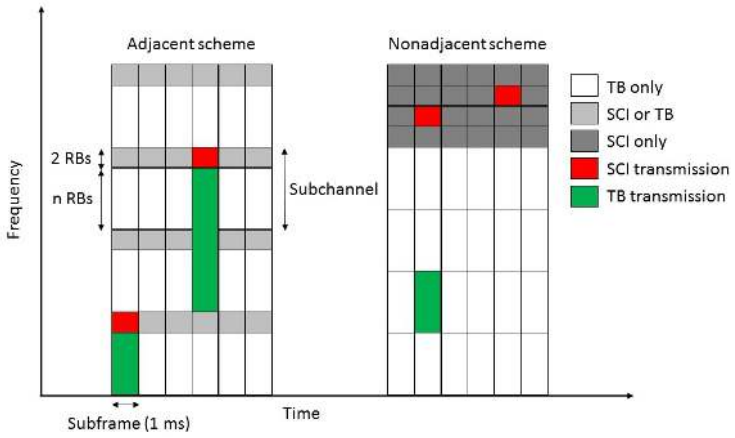

Figure 5.2: LTE-V resource blocks.

information transmission and transport block (TB) for data transmission. The SCIs and TBs are shared by all vehicles as shown in Fig. 5.1 to broadcast BSM and transmit data. When the vehicular density is high [1], the MAC protocol can be approximated as ALOHA [113]. LTE-Vehicle (LTE-V) defines adjacent and non-adjacent schemes for the resource blocks depending on whether the SCI and TB are transmitted in adjacent RBs or not.

The performance of V2X communications is analyzed using stochastic geometry in this chapter. Since the transmission range of the vehicles is much larger than the width of the road, vehicles on the two streets EW and NS can be modeled by two one dimensional (1-D) homogeneous Poisson point processes (PPPs) with the density (intensity) λ on each sub-channel. Besides the set of target transmitters $\Omega = \Omega_1 \cup \Omega_2$, the sets of interference sources on the two streets are denoted by Φ_1 and Φ_2, respectively. Let the Euclidean distances from the receiver to the center of the intersection and transmitter T_i be x_o and x_{T_i} respectively. We assume that all nodes are uniformly distributed on the road segments and the cumulative distributive functions (CDFs) of x_o and x_{T_i}

[1]The high density scenario is the most concerned since the PDR usually meets the requirement when the density is low.

are as follows:

$$F_{x_o}(x_o) = \frac{x_o}{x_o^{max}}, \tag{5.1}$$

$$F_{x_{T_i}|x_o}(x_{T_i}|x_o) = \begin{cases} \frac{x_{T_i}}{r}, & T_i \in \Omega_1 \\ \frac{\sqrt{x_{T_i}^2 - x_o^2}}{\sqrt{r^2 - x_o^2}}, & T_i \in \Omega_2 \end{cases} \tag{5.2}$$

Hence, the corresponding probability density functions (PDFs) can be written as

$$f_{x_o}(x_o) = \frac{1}{x_o^{max}}, \tag{5.3}$$

$$f_{x_{T_i}|x_o}(x_{T_i}|x_o) = \begin{cases} \frac{1}{r}, & T_i \in \Omega_1 \\ \frac{x_{T_i}}{\sqrt{(x_{T_i}^2 - x_o^2)(r^2 - x_o^2)}}, & T_i \in \Omega_2 \end{cases} \tag{5.4}$$

The PDF of transmitters on street NS (e.g., $T_i \in \Omega_2$) depends on the location of the receiver. Let T_{EW} and T_{NS} be two transmitters on streets EW and NS respectively (e.g., $T_{EW} \in \Omega_1$ and $T_{NS} \in \Omega_2$). When the receiver is located at the center point of the intersection, the PDFs of $x_{T_{EW}}$ and $x_{T_{NS}}$ become equivalent. Since the variables $x_{T_{EW}}$ and $x_{T_{NS}}$ are independent, the probability that $x_{T_{EW}} > x_{T_{NS}}$ can be written as

$$\begin{aligned} & Pr(x_{T_{EW}} > x_{T_{NS}}|x_o) \\ =& \int_{x_o}^{r} \int_{x_o}^{T_{EW}} f_{x_{T_{EW}}|x_o}(x_{T_{EW}}|x_o) \\ & \times f_{x_{T_{NS}}|x_o}(x_{T_{NS}}|x_o) dx_{T_{NS}} dx_{T_{EW}} \\ =& \frac{1}{2} + \underbrace{\frac{x_o^2}{2r\sqrt{r^2 - x_o^2}} \ln\left(\frac{x_o}{r + \sqrt{r^2 - x_o^2}}\right)}_{\text{Monotonically decreasing and negative}}. \end{aligned} \tag{5.5}$$

Given $x_o \in (0, x_o^{max})$, the second component of the result is negative and mono-

tonically decreasing. For cases that $x_o = 0$ and $x_o = x_o^{max}$, the probabilities of event $x_{T_{EW}} > x_{T_{NS}}$ are 0.5 and 0, respectively. Generally, it is more likely that $x_{T_{EW}}$ is smaller than $x_{T_{NS}}$, especially when the distance between the center of the intersection and the receiver is large. It means that vehicles on the opposite street suffer longer transmission distance.

5.1.2 Channel and interference models

The transmitted signals from the target vehicles undergo path loss and fast fading, the received power is denoted as P_{T_i}

$$P_{T_i} = h_{T_i}\overline{P}_{T_i} = \begin{cases} h_{T_i}P_{tx}\rho_1 x_{T_i}^{-\alpha_1}, & T_i \in \Omega_1 \\ h_{T_i}P_{tx}\rho_2 x_{T_i}^{-\alpha_2}, & T_i \in \Omega_2 \end{cases} \tag{5.6}$$

where P_{tx} is the transmitter power, $\alpha_j, j \in \{1, 2\}$ is the path loss exponent related to the propagation environment, and ρ_j denotes the path loss at the reference distance one meter away. h_{T_i} is caused by Rayleigh fading with unit mean $\mathbb{E}(h_{T_i}) = 1$, and it follows the exponential distribution $Pr(h_{T_i}) = e^{-h_{T_i}}$. $\overline{P}_{T_i}$ denotes the average received power level. When an obstruction exists between the two streets, the received signal on the other street suffers higher α_j, and the previous subsection shows that the transmission distance for $T_i \in \Omega_1$ is usually smaller that of $T_j \in \Omega_2$. Therefore, P_{T_i} for $T_i \in \Omega_1$ is very likely larger than P_{T_j}, for $T_j \in \Omega_2$. For OMA receiver, it decodes the message from T_j and regards the signal from T_i as noise, which leads to low SINR and PDR [11].

In addition to the signals from the NOMA group Ω, the signals from other transmitters lead to interference. Let us focus on one sub-channel, the aggre-

gated interferences from vehicles on the two streets are

$$\mathcal{I}_j = \begin{cases} \sum_{T_i \in \Phi_1} h_{T_i} P_{tx} \rho_1 x_{T_i}^{-\alpha_1}, & j = 1 \\ \sum_{T_i \in \Phi_2} h_{T_i} P_{tx} \rho_2 x_{T_i}^{-\alpha_2}, & j = 2 \end{cases} \tag{5.7}$$

The signals from interference sources have the same path loss exponents and reference power as the desired signals given in (5.6).

5.1.3 Receiver design

The current LTE-V applies OMA for V2X communications, most research works on broadcasting either assume interference-free or regard the interference from other transmitters as noise. However, the interference-free assumption is not reasonable when the density of vehicles is high, and when we decode $T_j \in \Omega_2$ in Fig. 5.1, the interference from $T_i \in \Omega_1$ has a large impact on the PDR, which will be elaborated later. To exploit the collided signals on the same sub-channel, NOMA is a potential technique to decode not only the strong user with higher power level but also the weak user with lower power level. Two types of NOMA receivers are considered in this work, which are based on SIC and JD respectively. To study a general case, we consider decoding a set of users Ω containing K transmitters (i.e., $|\Omega| = K$). The set of distances between the receiver and the transmitters in Ω is denoted by Υ. Let us denote $\Omega_{T_i}^{SIC}$ and $\Omega_{T_i}^{JD}$ as the sets of possible combinations of transmitters including user T_i that are successfully decoded by SIC and JD receivers, respectively. Specifically, the elements in $\Omega_{T_i}^{SIC}$ are vectors ω with a specific order such as $\omega = (T_a, T_b, ..., T_i)$. The vector ω includes all transmitters decoded before T_i and T_i itself. Let $\omega^{-1}(T_j)$ be the index of transmitter T_j in ω. The elements in ω belong to Ω and the last element is always T_i. $\Omega_{T_i}^{JD}$ is similar to $\Omega_{T_i}^{SIC}$, but the difference is that elements in $\Omega_{T_i}^{JD}$ are subsets without a specific order,

since decoding order is not important in JD.

OMA receiver

For the conventional OMA receiver, it decodes the message from one vehicle and regards the sum signals from other transmitters as noise. The maximum achievable rate from the transmitter T_i is

$$\mathcal{R}_{T_i}^{max} = \log_2(1 + \frac{P_{T_i}}{\sum_{j\in\Omega\setminus T_i} P_j + N_o + \mathcal{I}_1 + \mathcal{I}_2}), \tag{5.8}$$

where N_o is the noise power. Given the minimum signal-to-interference-plus-noise ratio (SINR), β_{T_i}, for successfully decoding user T_i, messages from transmitter T_i can be decoded when the following constraint is satisfied.

Lemma 1 (constraint of OMA receiver): Transmitter T_i can be successfully decoded by the OMA receiver when event $\mathcal{E}_{T_i}^{OMA}$ occurs, which is defined as

$$\mathcal{E}_{T_i}^{OMA} : \frac{P_{T_i}}{\sum_{T_j\in\Omega\setminus T_i} P_{T_j} + N_o + \mathcal{I}_1 + \mathcal{I}_2} \geq \beta_{T_i}. \tag{5.9}$$

In this chapter, the minimum SINR is assumed to be not less than 0 dB, i.e., $\beta \geq 1$. This is because practical V2X communications normally require a high data rate, which means high SINR requirement to guarantee that data are sent within short contact duration. In addition, the assumption helps simplify the derivation. In this case, at most one transmitter in the set Ω can satisfy the constraint (5.9) when there is more than one transmitter, i.e., $|\Omega| > 1$. According to the discussion above, the PDR from $T_j \in \Omega_2$ is likely lower than that of $T_i \in \Omega_1$. Therefore, the PDR from $T_j \in \Omega_2$ is lower than 0.5 even in the absence of interference and noise.

SIC receiver

SIC is widely studied and applied for NOMA due to its low complexity. It decodes the user with the highest received power first, which is known as the strongest user, and other users are regarded as interference sources. When the strong user is successfully decoded, the corresponding signal is removed via subtraction, then the weak users can be decoded in the absence of the strong user.

Lemma 2 (constraint of SIC receiver): Transmitter T_i can be successfully decoded by SIC receiver when $\exists\ \omega \in \Omega_{T_i}^{SIC}$ with a specific order such that event $\mathcal{E}_{\omega}^{SIC}$ is satisfied.

$$\mathcal{E}_{\omega}^{SIC}: \begin{cases} \frac{P_{\omega(1)}}{\sum_{T_j \in \Omega \setminus \omega(1)} P_{T_j} + N_o + \mathcal{I}_1 + \mathcal{I}_2} \geq \beta_{\omega(1)}, \\ \frac{P_{\omega(2)}}{\sum_{T_j \in \Omega \setminus \omega(1:2)} P_{T_j} + N_o + \mathcal{I}_1 + \mathcal{I}_2} \geq \beta_{\omega(2)}, \\ \quad ... \\ \frac{P_{T_i}}{\sum_{T_j \in \Omega \setminus \omega} P_{T_j} + N_o + \mathcal{I}_1 + \mathcal{I}_2} \geq \beta_{T_i}. \end{cases} \tag{5.10}$$

Generally, the SIC receiver decides the decoding order based on the power levels. For the strongest user, the SIC receiver decodes it in the same manner as the OMA receiver. According to (5.10), the strongest user is decoded first and user T_i is decoded as the last one ($\omega(|\omega|) = T_i$). Compared with the OMA receiver, the SIC receiver improves the PDR of the weak user and provides exactly the same performance for the strongest user as the OMA receiver.

JD receiver

Besides the SIC, another well-known NOMA receiver is the joint decoding receiver, which decodes multiple users simultaneously. Applying the JD receiver, the constraint to decode T_i is as follows.

Lemma 3 (constraint of JD receiver): Transmitter T_i can be successfully decoded by the JD receiver when $\exists\ \omega \in \Omega_{T_i}^{JD}$ so that event $\mathcal{E}_{\omega}^{JD}$ occurs.

$$\mathcal{E}_{\omega}^{JD}: \begin{cases} \frac{P_{\omega(1)}}{\sum_{T_j \in \Omega \setminus \omega} P_{T_j} + N_o + \mathcal{I}_1 + \mathcal{I}_2} \geq \beta_{\omega(1)}, \\ \cdots \\ \frac{P_{T_i}}{\sum_{T_j \in \Omega \setminus \omega} P_{T_j} + N_o + \mathcal{I}_1 + \mathcal{I}_2} \geq \beta_{T_i}, \\ \frac{\sum_{T_m \in \omega} P_{T_m}}{\sum_{T_j \in \Omega \setminus \omega} P_{T_j} + N_o + \mathcal{I}_1 + \mathcal{I}_2} \geq \beta_{\omega}. \end{cases} \tag{5.11}$$

The last constraint corresponds to the decoding of the joint signal, where $\beta_{\omega} = \prod_{T_j \in \omega}(1 + \beta_{T_j}) - 1$ denotes the minimum SINR of the sum rate. Other constraints in (5.11) correspond to SINR requirements for each individual user in the presence of interference from other transmitters in Ω that do not belong to ω. SIC receiver requires the same SINR for the sum rate by adding up all the constraints in (5.10). However, the independent power requirements of the JD receiver are looser than that of the SIC receiver. Therefore, JD receiver allows the power levels of multiple transmitters to be balanced and provides higher PDR than SIC receiver.

A research topic on NOMA is to guarantee the power difference between the strong and weak users, but it requires additional signaling and overheads, which leads to higher delay in V2X communications. Grant-free transmission is assumed in this work and the comparison between the two NOMA receivers is conducted. The performance of the above mentioned three kinds of receivers, i.e., OMA, SIC and JD receivers, will be analyzed rigorously in the following sections.

5.2 PDR analysis

Based on the system model in Section III, three schemes for V2X communications at a road intersection are studied in this chapter: 1) OMA-V2X; 2) SIC-V2X; and 3) JD-V2X. The PDR of these three schemes is investigated in this section.

5.2.1 OMA-V2X

According to the OMA receiver described in the previous section, the PDR of transmitter T_i given the location information Υ when OMA-V2X is applied can be written as follows.

Corollary 1 (PDR of OMA receiver): The probability of successful decoding of the signal from transmitter T_i with the OMA receiver is

$$\begin{aligned}
&\mathcal{P}_{\mathrm{OMA,T_i}}(\Upsilon, x_o) = \mathbb{E}[Pr(\mathcal{E}_{T_i}^{OMA})] \\
=&\mathbb{E}[Pr(\frac{P_{T_i}}{\sum_{T_j\in\Omega\setminus T_i} P_{T_j} + N_o + \mathcal{I}_1 + \mathcal{I}_2} \geq \beta_{T_i})] \\
\overset{(a)}{=}&\mathbb{E}[\exp(-\frac{(\sum_{T_j\in\Omega\setminus T_i} P_{T_j} + N_o + \mathcal{I}_1 + \mathcal{I}_2)\beta_{T_i}}{\overline{P}_{T_i}})] \\
=&\exp\left(-N_o\frac{\beta_{T_i}}{\overline{P}_{T_i}}\right)\mathcal{L}_{\mathcal{I}_1}(\frac{\beta_{T_i}}{\overline{P}_{T_i}})\mathcal{L}_{\mathcal{I}_2}(\frac{\beta_{T_i}}{\overline{P}_{T_i}})\prod_{T_j\in\Omega\setminus T_i}\mathcal{L}_g(\frac{\overline{P}_{T_j}\beta_{T_i}}{\overline{P}_{T_i}}) \\
=&\mathcal{C}(\frac{\beta_{T_i}}{\overline{P}_{T_i}})\prod_{T_j\in\Omega\setminus T_i}\mathcal{L}_g(\frac{\overline{P}_{T_j}\beta_{T_i}}{\overline{P}_{T_i}}),
\end{aligned} \tag{5.12}$$

where (a) follows the fact that $h_{T_i} \sim \exp(1)$. $\mathcal{L}_g(s) \triangleq \mathbb{E}(e^{-sg})$, $\mathcal{L}_{\mathcal{I}_1}(s) \triangleq \mathbb{E}(e^{-s\mathcal{I}_1})$, and $\mathcal{L}_{\mathcal{I}_2}(s) \triangleq \mathbb{E}(e^{-s\mathcal{I}_2})$ are Laplace transforms of the random fading component and random sum interference from the two streets. For simplification, $\mathcal{C}(s) \triangleq \exp(-N_o s)\mathcal{L}_{\mathcal{I}_1}(s)\mathcal{L}_{\mathcal{I}_2}(s)$ is used to represent the product of the three components. For the Rayleigh fading component, the Laplace transform

can be computed as

$$\mathcal{L}_g(s) = \mathbb{E}(e^{-sg}) = \int_0^\infty e^{-sg} \times e^{-g} dg = \frac{1}{1+s}. \tag{5.13}$$

For the interference from street EW, the Laplace transform is

$$\begin{aligned}
&\mathcal{L}_{\mathcal{I}_1}(s) = \mathbb{E}[\exp(-s \sum_{T_j \in \Phi_1} h_{T_j} P_{tx} \rho_1 x_{T_j}^{-\alpha_1}] \\
=&\mathbb{E}[\prod_{T_j \in \Phi_1} \exp(-s h_{T_j} P_{tx} \rho_1 x_{T_j}^{-\alpha_1})] \\
\overset{(b)}{=}&\exp(\lambda \int_0^\infty (\mathbb{E}[\exp(-s h_{T_j} P_{tx} \rho_1 x_{T_j}^{-\alpha_1})] - 1) d(2x_{T_j})) \\
\overset{(c)}{=}&\exp(\int_0^\infty \frac{-2\lambda}{1 + (sP_{tx}\rho_1)^{-1} x_{T_j}^{\alpha_1}} dx_{T_j}) \\
\overset{(d)}{=}&\exp(-\frac{2\pi\lambda (sP_{tx}\rho_1)^{\frac{1}{\alpha_1}}}{\alpha_1 sin(\frac{\pi}{\alpha_1})}),
\end{aligned} \tag{5.14}$$

where (b) is obtained from the probability generating function (PGFL) of PPP, (c) follows the Laplace transform of a random variable with exponential distribution in (5.13) and (d) is directly from [115].

The Laplace transform of the sum interference from street NS depends on the location of the receiver. Given the distance x_o between the receiver and the center point, the Laplace transform can be computed as

$$\begin{aligned}
&\mathcal{L}_{\mathcal{I}_2}(s) = \mathbb{E}[\exp(-s \sum_{T_j \in \Phi_2} h_{T_j} P_{tx} \rho_2 x_{T_j}^{-\alpha_2}] \\
=&\exp(\lambda \int_0^\infty (\mathbb{E}[\exp(-s h_{T_j} P_{tx} \rho_2 (x_{T_j}^2 + x_o^2)^{-\frac{\alpha_2}{2}})] - 1) d(2x_{T_j})) \\
=&\exp(\int_0^\infty \frac{-2\lambda}{1 + (sP_{tx}\rho_2)^{-1} (x_{T_j}^2 + x_o^2)^{\frac{\alpha_2}{2}}} dx_{T_j}),
\end{aligned} \tag{5.15}$$

which is monotonically increasing with x_o. This is intuitively correct that the sum interference decreases as the distance between the receiver and street NS increases, thus improving the PDR. A lower bound (5.15) can be obtained

when x_o becomes zero:

$$\mathcal{L}_{\mathcal{I}_2}(s) \leq \mathcal{L}^{LB}_{\mathcal{I}_2}(s) = \exp(-\frac{2\pi\lambda(sP_{tx}\rho_2)^{\frac{1}{\alpha_2}}}{\alpha_2 sin(\frac{\pi}{\alpha_2})}). \tag{5.16}$$

For the special case when the number of transmitters to be decoded is 2, i.e., $K = 2$ with $T_1 \in \Omega_1, T_2 \in \Omega_2$, we have the PDR of T_1 as follows.

$$\mathcal{P}_{\mathrm{OMA,T_1}}(\Upsilon, x_o) = \frac{\overline{P}_{T_1}}{\overline{P}_{T_1} + \beta_{T_1}\overline{P}_{T_2}} \mathcal{C}(\frac{\beta_{T_1}}{\overline{P}_{T_1}}). \tag{5.17}$$

5.2.2 SIC-V2X

When the SIC decoder is applied, the strongest user is decoded in the same way that of the OMA decoder, thus the same PDR is obtained. For the weak users, SIC eliminates the signal from the strongest user, and thus increases the PDR. Applying the SIC decoder, we have the following corollary.

Corollary 2 (PDR of SIC receiver): The probability of successful decoding of the signal from transmitter T_i with the SIC receiver is illustrated by (5.18) and (5.19).

$$\begin{aligned}\mathcal{P}_{\mathrm{SIC,T_i}}(\Upsilon, x_o) = \sum_{\omega \in \Omega^{SIC}_{T_i}} [\prod_{T_j \in \omega} (\overline{P}_{T_j} q_{T_j})^{-1}] \times \\ [\prod_{T_j \in \Omega \setminus \omega} (1 + \overline{P}_{T_j} \sum_{T_m \in \omega} \beta_{T_m} q_{T_m})^{-1}] \mathcal{C}(\sum_{T_j \in \omega} \beta_{T_j} q_{T_j}),\end{aligned} \tag{5.18}$$

with

$$q_{T_j} = \overline{P}^{-1}_{T_j} + \sum_{T_m = \omega(1)}^{\omega(\omega^{-1}(T_j)-1)} \beta_{T_m} q_{T_m}. \tag{5.19}$$

Proof. Please refer to Appendix A. □

Considering the special case that $K = 2$ with $T_1 \in \Omega_1, T_2 \in \Omega_2$, we have the PDR of T_1 as follows.

$$\begin{aligned}\mathcal{P}_{\mathrm{SIC,T_1}}(\Upsilon, x_o) =& \frac{\overline{P}_{T_1}}{\overline{P}_{T_1} + \beta_{T_1}\overline{P}_{T_2}} \mathcal{C}(\frac{\beta_{T_1}}{\overline{P}_{T_1}}) \\ &+ \frac{\overline{P}_{T_2}}{\beta_{T_2}\overline{P}_{T_1} + \overline{P}_{T_2}} \mathcal{C}(\frac{\beta_{T_1}}{\overline{P}_{T_1}} + \frac{\beta_{T_2}(1+\beta_{T_1})}{\overline{P}_{T_2}}).\end{aligned} \tag{5.20}$$

The first component on the RHS denotes decoding T_1 as the strong user, which is the same as (5.17). The second component denotes decoding T_1 as the weak user, in which T_2 is first decoded as the strong user and then be canceled. After that, T_1 is decoded without the interference from T_2.

5.2.3 JD-V2X

Based on (5.11), we have the following corollary for the JD receiver.

Corollary 3 (PDR of JD receiver): The probability of successful decoding of the signal from transmitter T_i with the JD receiver is shown in (5.21) and (5.22).

$$\mathcal{P}_{\mathrm{JD,T_i}}(\Upsilon, x_o) = \sum_{s=1}^{|\Omega_{T_i}^{JD}|} \sum_{\substack{\omega_{1:s} \in \Omega_{T_i}^{JD} \\ \omega_m \neq \omega_n \\ |\omega_m| \leq |\omega_n| \\ m<n}} (-1)^{s-1} \sum_{\substack{T_{j_1} \in \omega_{I_1} \\ \omega_{I_1} = \omega_1}} \cdots \sum_{\substack{T_{j_s} \in \omega_{I_s} \\ \omega_{I_s} = \omega_s \setminus \omega_{s-1}}} c(\omega_{1:s}) \tag{5.21}$$

with

$$
\begin{aligned}
c(\omega_{1:s}) &= \begin{cases} 0, & \exists\ \omega_m \not\subseteq \omega_n,\ m<n \\ \frac{a_{T_{j_1}:T_{j_s}}\mathcal{C}(b_{T_{j_1}:T_{j_s}})}{\prod_{T_m\in\Omega\setminus\omega_{1:s}}(1+\overline{P}_{T_m}b_{T_{j_1}:T_{j_s}})}, & Otherwise \end{cases} \\
a_{T_{j_1}:T_{j_s}} &= \prod_{m=1}^{s}\{(\prod_{T_n\in\omega_{I_m}}\frac{\overline{P}_{T_n}^{-1}}{\overline{P}_{T_n}^{-1}+b_{T_{j_1}:T_{j_{m-1}}}})\times(\prod_{T_l\in\omega_{I_m}\setminus T_{j_m}}\frac{\overline{P}_{T_l}^{-1}+b_{T_{j_1}:T_{j_{m-1}}}}{\overline{P}_{T_l}^{-1}-\overline{P}_{T_{j_m}}^{-1}})\}, \\
b_{T_{j_1}:T_{j_s}} &= \sum_{m=1}^{s}[\beta_{\omega_{I_m}}(\overline{P}_{T_{j_m}}^{-1}+b_{T_{j_1}:T_{j_{m-1}}})+\sum_{T_n\in\omega_{I_m}}\beta_{T_n}(\overline{P}_{T_n}^{-1}-\overline{P}_{Tj_m}^{-1})].
\end{aligned}
\tag{5.22}
$$

Proof. Please refer to Appendix B. □

For the special case that $K=2$ with $T_1\in\Omega_1, T_2\in\Omega_2$, we have the PDR of T_1 as illustrated in (5.23).

$$
\begin{aligned}
&\mathcal{P}_{\mathrm{JD,T_1}}(\Upsilon,x_o) \\
=&\frac{\overline{P}_{T_1}}{\overline{P}_{T_1}+\beta_{T_1}\overline{P}_{T_2}}\mathcal{C}(\frac{\beta_{T_1}}{\overline{P}_{T_1}})+\frac{\overline{P}_{T_1}}{\overline{P}_{T_1}-\overline{P}_{T_2}}\mathcal{C}(\frac{\beta_{T_1}(1+\beta_{T_2})}{\overline{P}_{T_1}}+\frac{\beta_{T_2}}{\overline{P}_{T_2}}) \\
&+\frac{\overline{P}_{T_2}}{\overline{P}_{T_2}-\overline{P}_{T_1}}\mathcal{C}(\frac{\beta_{T_1}}{\overline{P}_{T_1}}+\frac{\beta_{T_2}(1+\beta_{T_1})}{\overline{P}_{T_2}})-\frac{\overline{P}_{T_1}}{\overline{P}_{T_1}+\beta_{T_1}\overline{P}_{T_2}}\mathcal{C}(\frac{\beta_{T_1}(1+\beta_{T_2})}{\overline{P}_{T_1}}+\frac{\beta_{T_2}}{\overline{P}_{T_2}}).
\end{aligned}
\tag{5.23}
$$

5.2.4 Average PDR at the intersection region

According to the individual analysis of the three receivers, the average PDR is obtained as follows.

Corollary 4 (Average PDR): For each kind of receiver, the average probability of successful decoding of the signal from transmitter T_i at the road

intersection can be obtained from the individual PDR as

$$\mathcal{P}_{\text{receiver,T}_\text{i}} = \int_0^{x_o^{max}} \int_{x_{T_K}^{min}}^{x_{T_K}^{max}} ... \int_{x_{T_1}^{min}}^{x_{T_1}^{max}} \mathcal{P}_{\text{receiver,T}_\text{i}}(\Upsilon, x_o) \\ f_{x_{T_1}}(x_{T_1})...f_{x_{T_K}}(x_{T_K})f_{x_o}(x_o)dx_{T_1}...dx_{T_K}dx_o, \tag{5.24}$$

where the integral interval depends on the network topology. For the road intersection in this chapter, the integral interval of a transmitter depends on which street it belongs to and the distance between the receiver and the center point. For instance, the integral intervals of $x_{T_i}, T_i \in \Omega_1$ and $x_{T_j}, T_j \in \Omega_2$ are $[0, r]$ and $[x_o, r]$, respectively. In the next section regarding simulation studies, we consider different scenarios and analyze the performance of the three schemes.

5.2.5 Optimization of the data rate

In practice, a wireless communication system detects the power level of noise plus interference in the background and prefers an appropriate data rate so that the goodput can be maximized. The goodput is defined as the number of useful information bits delivered by the network per unit of time that excludes re-transmitted data packets as well as protocol overhead bits. For conventional OMA schemes, the optimization aims to maximize the goodput for a single broadcaster. However, NOMA-based systems decode multiple users simultaneously, and thus the optimization needs to jointly satisfy the minimum SINR for multiple transmitters. To optimize the PDR and common data rate so that the overall goodput is maximized for multiple users, we propose a data rate selection algorithm for the three V2X schemes. The optimization problem

is characterized as follows:

$$\begin{aligned} \mathcal{R}^{opt} &= \arg\max_{\mathcal{R}} (\sum_{T_i \in \Omega} \mathcal{P}_{\mathrm{T_i}}) \mathcal{R} \\ s.t., \mathcal{R} &\in [\mathcal{R}_{min}, \mathcal{R}_{max}] \end{aligned} \tag{5.25}$$

where $\mathcal{P}_{\mathrm{T_i}}$ can be $\mathcal{P}_{\mathrm{OMA,T_i}}$, $\mathcal{P}_{\mathrm{SIC,T_i}}$, or $\mathcal{P}_{\mathrm{JD,T_i}}$ depending on the decoder design.

The PDR for the three V2X schemes is expressed in equations (5.12), (5.18), and (5.21), respectively. The average PDR is difficult to obtain as it involves multiple integrals. However, the optimization problem in (5.25) only involves one design variable with a fixed interval, hence we can solve the problem via the single-variable optimization algorithm [116]. In this chapter, golden section search and parabolic interpolation are applied to identify the optimal data rate.

5.3 Numerical results

This section discusses the numerical results for the three V2X schemes, and the analytical results are validated through simulation. In particular, the PDR performance at an intersection under diverse configurations is investigated, and the performance of the proposed data rate optimization is evaluated and its impact is studied. We consider the ROI with radius $r = 200$ m, vehicles with maximum distance $x_o^{max} = 100$ m away from the center point of the road intersection are studied. All transmitters broadcast with the same transmission power at 10 dBW with a bandwidth of 10 MHz. The reference path loss is 54.85 dB for LOS propagation and 54.55 dB for NLOS propagation. The path loss exponent is 1.67 for the LOS case and 1.90 the NLOS case as suggested in [117]. The noise power spectral density is assumed to be -93 dBm/Hz. We define the reference SNR [118] as the average received SNR from the transmitter located at the cell edge. For LOS and NLOS cases, the reference SNRs are 10 dB and

5 dB, respectively. The number of users to decode, K, is first fixed as two with $T_1 \in \Omega_1, T_2 \in \Omega_2$, and the scenario with more number of transmitters follows. For the sake of intuition, T_1 is considered as the LOS user while T_2 is regarded as the NLOS user.

5.3.1 Impact of interfering vehicular density

In addition to the noise, interference from other transmitters degrades the PDR performance. To study the impact of interference, we vary the density of transmitters in single sub-channel and obtain the analytical and simulation results as shown in Fig. 5.3. Specifically, we consider the C-V2X resource blocks in Fig. 5.2 with 10 MHz bandwidth and 100 ms scheduling period according to the standard [34], and assume 100 sub-channels per scheduling period. By fixing the data rate at 1.6 bps/Hz ($\beta = 2$ according to (5.8)), each user can transmit $\frac{10^7 \times 0.1 \times 1.6}{100 \times 8} = 2000$ bytes packet give one sub-channel. This is sufficient for not only 344 bytes BSM broadcasting [119] but also the HD 720 video streaming when the transmitter is assigned with 25 sub-channels. The interfering vehicular density on each street varies from 1 car per km to 215 cars per km (e.g., 0.01 car per km per sub-channel to 2.15 cars per km per sub-channel). This range is sufficient to study the practical density of interfering vehicles.

For both LOS and NLOS users, the simulation results of the three schemes match with the analytical results. This validates the theoretical analysis in the previous section. The gap among the three schemes decreases as the interfering vehicular density increases. Compared with the NLOS user, the PDR curves of the LOS user are relatively close under the three schemes. In the low interference regime (interfering vehicular density is 1 car per km), JD provides the highest PDR at 0.9, followed by SIC that shows PDR at 0.7. Compared

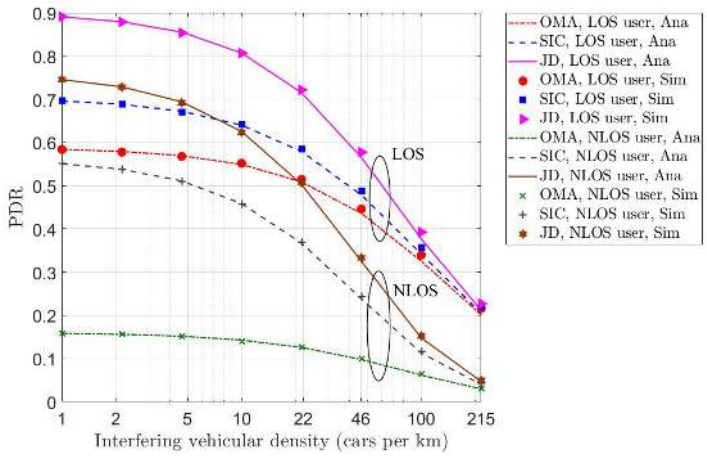

Figure 5.3: PDR under different interfering vehicular density.

with the two NOMA schemes, the OMA decoder gives the lowest PDR at around 0.6. When the interfering vehicular density reaches 100 cars per km, the three schemes provide similar PDR at around 0.34. For the NLOS user, the gaps among the three schemes are quite large. The PDR of OMA is lower than 0.2 even in the low interference regime. The two NOMA schemes provide better performance. SIC shows 0.55 PDR in the low interference regime, and JD can provide an additional 0.2 PDR improvement. Fig. 5.3 verifies that NOMA can significantly improve the PDR of transmitters suffering from NLOS propagation.

5.3.2 Impact of data rate

This subsection studies the impact of the data rate. For the sake of brevity, the data rate is denoted in unit Mbps give the 10 MHz bandwidth. For instance, the data rate is equivalent to 16 Mbps when $\beta = 2$. We consider interfering vehicular density at 10 cars per km and vary the data rate from 10 to 35 Mbps (i.e., $\beta \in [1, 10]$). Fig. 5.4 compares the PDR performance of the three schemes.

Similar to the study on interfering vehicular density, the OMA scheme

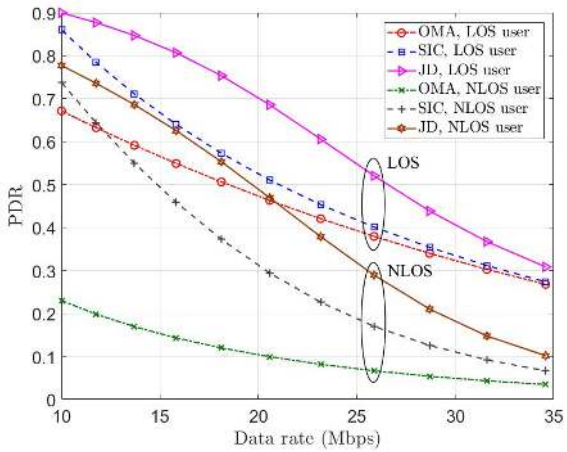

Figure 5.4: PDR under different data rate.

shows low PDR for the NLOS user due to relative low received signal strength as compared with the LOS user. The maximum PDR of OMA is lower than 0.23 when the data rate is equal to 10 Mbps. In contrast, the two NOMA schemes have PDR higher than 0.7 given the same data rate. Compared with the SIC scheme, the JD scheme shows around 0.4 and 0.2 PDR enhancements for the LOS and NLOS users, respectively. However, the performance gap between the two NOMA schemes is minor when the data rate is low (e.g., 10 Mbps). The results imply that the JD decoder is preferred for higher PDR, but the SIC decoder could be a better choice when the data rate is low due to similar performance and lower complexity.

5.3.3 Impact of the number of users

After studying the two-user scenario, this subsection evaluates the goodput performance with multiple users. We consider the case with 10 cars per km and $\beta = 2$. The number of transmitters to decode on each street varies from zero to two, and the results up to four users are illustrated in Fig. 5.5.

The analytical results are denoted by the red text while the simulation results are denoted by the blue text. $N_{NS} = |\Omega_2|$ and $N_{EW} = |\Omega_1|$ denote the

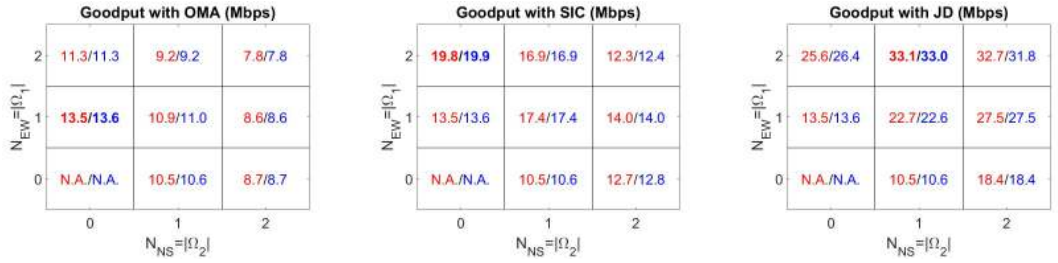

(a) Goodput with OMA. (b) Goodput with SIC. (c) Goodput with JD.

Figure 5.5: Goodput performance under different number of transmitters. The analytical results are denoted by the red text and the simulation results are denoted by the blue text. The maximal goodput results are highlighted with bold text.

number of access users on streets NS (e.g., NLOS users) and EW (e.g., LOS users), respectively. This further confirms that our model is feasible for multiple transmitters. For the three schemes, JD achieved the maximum goodput at 33.1 Mbps in the three-user case, SIC obtains the maximum goodput at 14.7 Mbps with two-user access, and OMA gets the maximum goodput at 13.5 Mbps with single-user access. Since it is difficult for OMA and SIC receivers to satisfy the requirement of power difference between the strongest user and the sum of other users plus noise when the number of users is large, JD is the best solution when the number of users is larger than two.

5.3.4 Optimal data rate and maximum goodput

This subsection is to evaluate the proposed data rate optimization algorithm. We first consider the two-user case, the optimal data rate and the corresponding maximum goodput are illustrated in Fig. 5.6 and 5.7.

To maximize the total goodput, we can see that the optimal data rate for the three schemes are $\mathcal{R}_{OMA}^{opt} \geq \mathcal{R}_{JD}^{opt} \geq \mathcal{R}_{SIC}^{opt}$. Applying the optimal data rate, the two NOMA schemes show significant improvement compared with the OMA scheme, especially in the low density regime. When the interfering vehicular density is lower than 10 cars per km, the JD scheme provides more

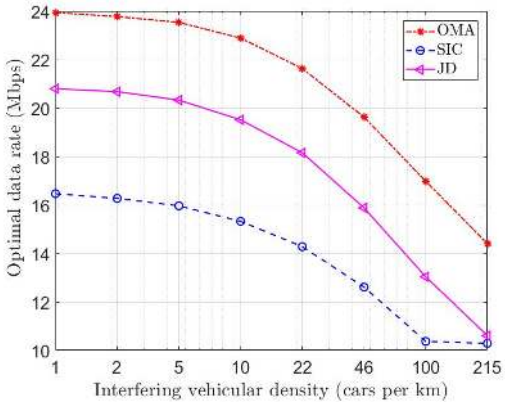

Figure 5.6: Optimal data rate under different interfering vehicular density.

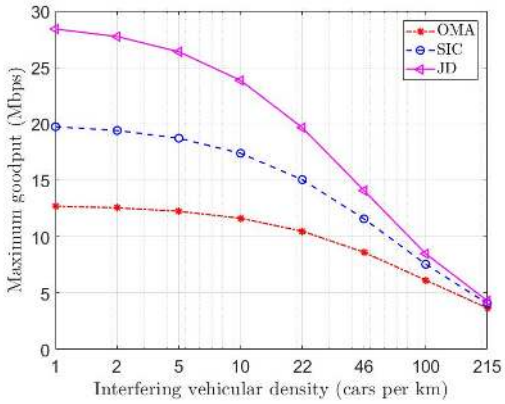

Figure 5.7: Maximum goodput under different interfering vehicular density.

than 100% goodput enhancement compared with the OMA scheme. In the same regime, the SIC scheme shows around 50% improvement. When the interfering vehicular density is equal to 10 cars per km, the goodput distribution of the two-user case under different data rate is shown in Fig. 5.8. Via exhaustive search, we can observe that the maximum goodput and the corresponding optimal data rate match the results provided by the optimization algorithm. It can be seen that the sum goodput first increases as the data rate increases. This means that the interference plus noise is acceptable due to the low data rate, namely low minimum SINR requirement, thus the increasing data rate leads to better goodput performance. After achieving the maximum value, the goodput begins to decreases because the high data rate transmission is sensi-

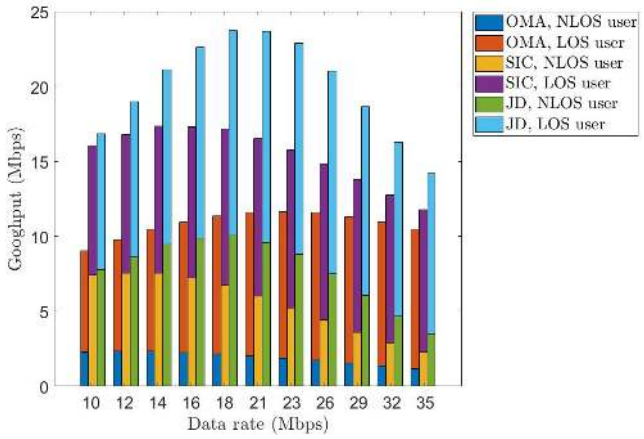

Figure 5.8: Goodput performance under different data rate.

tive to the interference. In this case, a higher data rate leads to lower PDR and worse goodput performance. The distribution of the maximized goodput in Fig. 5.7 is illustrated in Fig. 5.9.

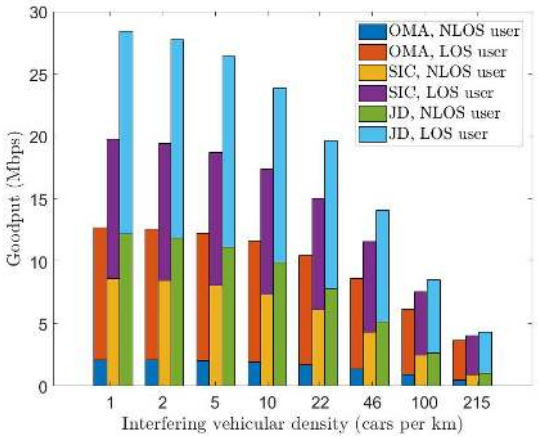

Figure 5.9: Goodput distribution under different interfering vehicular density.

We have the following observations: 1) the goodput of the NLOS user with OMA receiver is much smaller than others. This is because the OMA scheme applies the highest data rate to maximize the goodput as shown in Fig. 5.6. In this case, the majority of the goodput comes from the LOS user, and thus the goodput of the NLOS user is relatively low; 2) for both the SIC and JD schemes, it can be observed that the goodput of the LOS and NLOS users

is close, especially in the low density regime. It implies that the two NOMA schemes provide better fairness compared with the OMA scheme; 3) in the high density regime, the overall goodput of the three schemes becomes similar, and the goodput is mainly from the LOS user (the strong user); 4) points 1) to 3) indicate that the development of a hybrid protocol can potentially enhance NOMA-based V2X communications for different communication scenarios.

We then fix the interfering vehicular density at 10 cars per km and study the impact of the number of users. The maximum goodput is shown in Fig. 5.10. For the OMA scheme, the maximum goodput is achieved with single-user

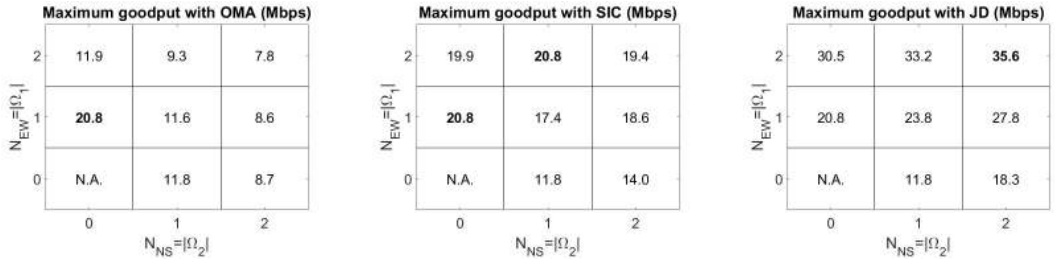

(a) Maximum goodput with OMA.

(b) Maximum goodput with SIC.

(c) Maximum goodput with JD.

Figure 5.10: Maximum goodput under different numbers of transmitters with the optimal data rate.

access from street EW. An interesting point is that the maximum goodput of the SIC scheme is the same as that of the OMA scheme, but it can be obtained via not only single-user access but also three-user access (two users from street EW and one user from street NS). It further proves that SIC provides better fairness than OMA. Compared with OMA and SIC, the JD scheme offers much higher goodput, especially for a large number of access users. We can observe that the maximum goodput of JD is achieved in the four-user scenario. For the other two schemes, the maximum goodput is obtained with a smaller number of users. Therefore, it again verifies that the JD scheme is the best choice given a large number of transmitters. For four-user access, the goodput improvement

is 375% and 84% when compared with OMA and SIC, respectively.

5.4 Summary

This chapter presents a tractable network model to analyze C-V2X broadcast performance operating in mode 4. Specifically, the road intersection scenario is considered and the communications can be divided into two categories: 1) LOS communications between vehicles on the same street; 2) NLOS communications between vehicles on different streets. We derive the PDR expressions of these two types of communications for various receiving techniques, i.e., the conventional OMA receiver, SIC receiver, and JD receiver. The analytical and simulation results reveal that the NOMA schemes generally outperform the OMA scheme, especially for the users suffering from NLOS propagation and long transmission distance. Several interesting points are obtained from the results: 1) For applications requiring high data rate, JD scheme is always the best choice; 2) For low data rate applications, the SIC scheme requires relatively low complexity and has similar performance compared with the JD scheme; 3) In the extremely low SINR regime, all the three receiving schemes have similar performance and thus the OMA receiver should be applied due to the lowest complexity; 4) Where there is a large number of users (i.e., $K > 2$), JD is the best solution to provide high goodput; 5) As implied from points 1) to 4), we note that the development of a hybrid protocol for NOMA-based V2X communications is valuable to meet the requirements of diverse scenarios. Besides the performance analysis, we also propose a data rate optimization scheme to maximize the sum goodput. The goodput distribution among the users implies that both the SIC and JD schemes offer good fairness among multiple users, which cannot be achieved by the OMA scheme due to the low PDR of the weak users.

Chapter 6

Feasibility Study of C-V2X communications with NOMA

This chapter aims to investigate the integration of NOMA and C-V2X communications. There are two radio interfaces supported by the LTE-V standard: the cellular interface and the PC5 interface. The first one supports V2I communications and the second one, which is based on direct LTE sidelink, supports V2V communications. In this chapter, the PC5 sidelink interface is deployed to enable direct communications so that the packets are not required to pass through the eNodeB. We focus on the physical layer and discuss the implementation of NOMA in the PC5 sidelink interface.

6.1 Physical layer of C-V2X

In C-V2X communications, the time-frequency resource pool is divided into RBs as shown in Fig. 5.2 in the previous chapter and is modulated with SC-FDMA. According to the standard, C-V2X supports the 10 and 20 MHz bandwidth. For each channel, it is divided into sub-frames, RBs, and sub-channels. The smallest resource that can be assigned to a user is a RB. It

consists of 12 sub-carriers with 15 kHz bandwidth, thus, the entire bandwidth of a RB is 180 kHz. In LTE-V, sub-channels are defined as a group of RBs in the same sub-frame. Depending on the communication requirement, one sub-channel can be assigned with different number of RBs. Sub-channels are utilized to transmit control information and data. There are two types of channels in LTE-V:

1. Physical sidelink shared channel (PSSCH): It is utilized to transmit TBs that contain a full packet to be transmitted, such as the BSM and multimedia content for infotainment service. Since the packet size to be transmitted for each user varies, one user can occupy multiple TBs. Thus, the channel resource cannot be assigned orthogonally in a congested vehicular network, especially when some users are transmitting large packets for video streaming. To solve the problem, we utilize NOMA for TBs transmission over PSSCH, and NOMA-based receivers are employed to decode the overlapping messages from multiple users.

2. Physical sidelink control channel (PSCCH): It is used to transmit SCI messages. Basically, the information contained in SCI is used for TB transmission, and all TBs are associated with the corresponding SCIs. This is also known as the scheduling assignment. For instance, the SCI contains the PSCCH resource allocation for the TB, the modulation and coding scheme (MSC) utilized to transmit the TB, and the resource reservation interval for SPS. The SCI messages include the necessary information to decode the data in TBs, thus the failure of SCI decoding means that the corresponding TB transmission fails. Each SCI message occupies two RBs, the size of SCI is relatively small compared with that of TBs. Since SCI contains the critical information for TB transmission and it only needs a small amount of channel resource, we use OMA for

SCI transmission over PSCCH.

For PSCCH and PSSCH, LTE-V provides two sub-channelization schemes as illustrated in 5.2: adjacent and nonadjacent schemes.

1. Adjacent scheme: For the adjacent scheme, SCI and the associated TB occupy adjacent RBs. For each transmission, the first two RBs of the first sub-channel are allocated to the SCI. And the associated TB is transmitted in the following RB, it can occupy multiple sub-channels depending on its size. If the number of occupied sub-channels is larger than one, the first two RBs of the following sub-channels are also used for TB transmission.

2. Nonadjacent scheme: For the non-adjacent scheme, the entire resource pool is divided into two pools for PSCCH and PSSCH. The two pools are dedicated to transmit either SCIs or TBs.

In the proposed NOMA-based C-V2X communication schemes, the non-adjacent scheme is employed since OMA-based SCI and NOMA-based TB transmissions are considered in this work, the non-adjacent scheme enables independent resource allocations for PSCCH and PSSCH depending on either OMA or NOMA is used.

In each sub-frame, there are 14 symbols and four of them are dedicated to demodulation reference signals (DMRSs). Specifically, the third, sixth, ninth, and 12th symbols are selected as pilot symbols, the receivers use the DMRSs to estimate the radio channels and combat negative effect caused by the time-frequency-selective channels. Compared with 802.11p where the first symbol and four out of 52 sub-carriers in data symbols are allocated for pilots, C-V2X allocates a larger partition of resource for channel estimation, thus it is expected to provide better robustness against the negative effect caused

by the rapid motion of vehicles. In terms of modulation, SCIs are always modulated with QPSK while TBs can be modulated with either QPSK or 16-QAM. Besides, the normal cyclic prefix is employed against inter-symbol-interference (ISI) and turbo coding is used to improve the block error rate (BLER) performance.

6.2 Receiver design

After introducing the physical layer of C-V2X, this section aims to investigate the NOMA-based receiver design. Because the SCI is assumed to transmit orthogonally over PSCCH, this chapter assumes perfect SCI transmission and focuses on the non-orthogonal TB transmissions. Firstly, the conventional OMA receiver is introduced.

6.2.1 OMA receiver for C-V2X communications

Fig. 6.1 shows the block diagram of the conventional OMA receiver.

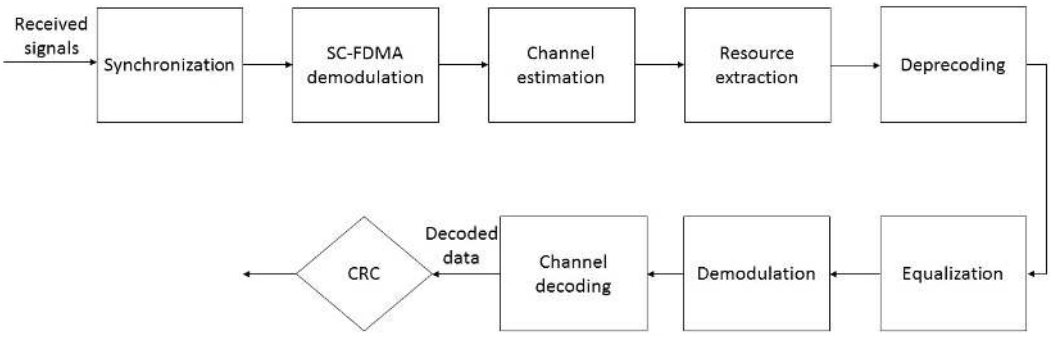

Figure 6.1: Block diagram of the OMA receiver.

After receiving the signals, the first step is to perform synchronization, the synchronized signals are then sent to the SC-FDMA demodulation block. After that, the DMRSs are extracted to perform channel estimation. Chapters 3 and 4 have proposed and evaluated a robust channel estimation scheme for

the overlapping signals, we assume perfect channel estimation and compare the performance of OMA, SIC-based NOMA, and JD-based NOMA receivers. After channel estimation, the data on the desired TB is extracted. The resource allocation information is obtained from the corresponding SCI messages. The next step is to perform deprecoding, namely the IFFT operation. Then, equalization is conducted to reverse the distortion incurred by the radio channel. Specifically, a minimum mean square error (MMSE) equalizer is employed in this work. Let X be the transmitted symbol, H is the channel, N is the complex white Gaussian noise with zero mean and variance N_o, the desired signal Y is

$$Y = HX + N. \tag{6.1}$$

Given M receiving antennas, H, N, and Y are $M \times 1$ matrices. After the MMSE equalization, the output signal $\hat{X}$ is as follows.

$$\hat{X} = (H^H H + N_o I)^{-1} H^H Y. \tag{6.2}$$

Where I is the identity matrix, and we utilize $[.]^{-1}$ and $[.]^H$ to denote the inverse and hermitian transpose, respectively. Let $W = (H^H H + H_o I)^{-1} H^H$ and the variance of noise after MMSE equalization as $\hat{N}_o = WW^H N_o$. The output signal is then demodulated to obtain the log-likelihood ratio (LLR).

$$LLR(X(i)) = \log [\frac{p(X(i) = 0|Y)}{p(X(i) = 1|Y)}]. \tag{6.3}$$

With

$$p(X(i) = j|Y) \propto \sum_{X(i)=j} \exp (-\frac{|X - \hat{X}|^2}{\hat{N}_o}). \tag{6.4}$$

Where $X(i)$ denotes the i-th bit of the transmitted symbol. To reduce the computational complexity, we employ a simple log-max approximation as follows.

$$LLR(X(i)) = \log\left[\frac{p(X(i)=0|Y)}{p(X(i)=1|Y)}\right]. \tag{6.5}$$

With

$$\sum_{X(i)=j} \exp\left(-\frac{|X-\hat{X}|^2}{\hat{N}_o}\right) \approx \max_{X(i)=j} \exp\left(-\frac{|X-\hat{X}|^2}{\hat{N}_o}\right). \tag{6.6}$$

The demodulated soft LLR is used for channel decoding and the result is passed to perform cyclic redundancy check (CRC).

For non-orthogonal C-V2X communications, the receivers need to decode multiple users from the superimposed signals. We propose two NOMA receivers based on SIC and JD, respectively.

6.2.2 SIC-based NOMA receiver for C-V2X communications

The block diagram of the SIC-based NOMA receiver is illustrated in Fig. 6.2.

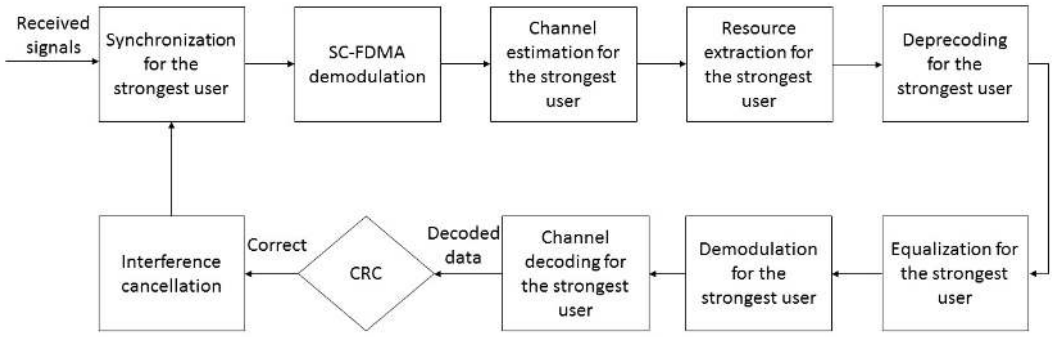

Figure 6.2: Block diagram of the SIC-based NOMA receiver.

In terms of the SIC-based NOMA receiver, the block diagram is basically the same as that of the OMA receiver. For instance, equalization is performed for the strongest user while the interference from other users is regarded as noise. Assuming that the overlapping signals from K transmitters and the user index k determines the decoding order, namely the received power level P_k from user k follows $P_i \geq P_k, \forall i \leq k$, without loss of generality. For user k, the MMSE equalization is performed as

$$\hat{X_k} = [H_k^H H_k + (N_o + \sum_{i=k+1}^{K} P_i)I]^{-1} H_k^H Y. \tag{6.7}$$

Where H_k is the channel information for user k. The summation of power from users $k+1$ to K are regarded as part of the noise. It can be observed that the channel decoding result is passed to the CRC check. Once the desired packet of user k is decoded correctly, it is used to perform interference cancellation and thus, the decoding of the remaining users can be performed in the absence of interference from user k.

6.2.3 JD-based NOMA receiver for C-V2X communications

For the JD-based NOMA receiver, the block diagram is shown in Fig. 6.3.

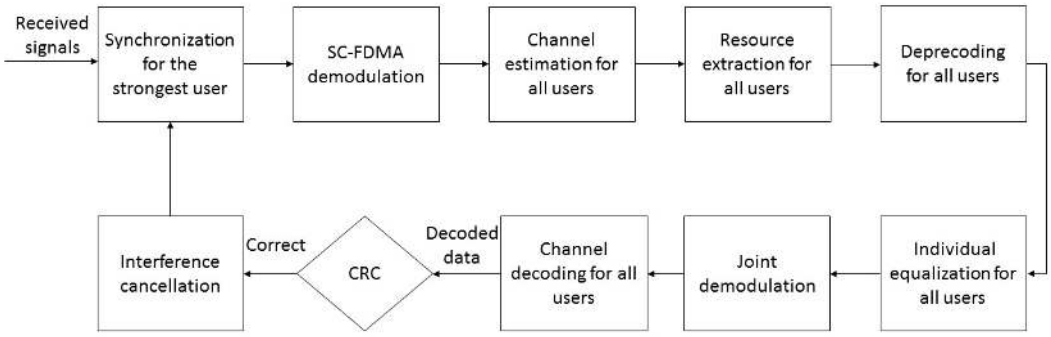

Figure 6.3: Block diagram of the JD-based NOMA receiver.

For the synchronization, the frame offset of the strongest user is evaluated and we perform the corresponding synchronization for all users. In this work, we consider that K users occupy the same RBs for TB transmissions, thus we can conduct the same SC-FDMA demodulation, resource extraction, and deprecoding for all users. Besides, individual channel decoding is adopted to reduce the computational complexity. Even though joint channel decoders, like the virtual channel decoder adopted in Chapter 4, are expected to provide better performance, this work focuses on the equalization and demodulation parts and the joint channel decoder design is a potential research direction. Since it is possible that only a portion of users is successfully decoded after the first iteration, the JD-based NOMA receiver includes interference cancellation to eliminate the signals from the decoded users so as to reduce the computational complexity of the following iterations. When no user can be decoded after an iteration, the receiver is interrupted.

Since the LLRs of individual users are required to perform the conventional channel decoding, this work proposes an individual equalization scheme for all users and performs joint demodulation to obtain the LLRs of individual users by taking the transmitted signals from remaining users into consideration.

In terms of individual equalization, the proposed scheme makes uses of the channel information from all users and aims to minimize the mean square error. For the first iteration, we aim to minimize the mean square error of user k as follows.

$$\min_{W_k} \mathbb{E}\{(W_k Y - X_k)(W_k Y - X_k)^H\}. \tag{6.8}$$

Let $G_k = [H_1, H_2, ..., H_{k-1}, H_{k+1}, ..., H_K]$ denotes the channel information of the remaining users. By solving the optimization problem in (6.8), the

optimal matrix W_k can be obtained as follows.

$$W_k = [I + H_k^H (N_o + G_k G_k^H)^{-1} H_K]^{-1} H_k^H (N_o I + G_k G_k^H)^{-1}. \tag{6.9}$$

It can be observed that compared with the SIC-based equalizer in (6.7) where the average power P_i over the whole sub-channel from user i is regarded as part of the noise, the proposed JD-based equalizer takes the exact channel information of all the remaining users into consideration to minimize the mean square error. Since the optimal transformation matrices for all users can vary, the transformation matrices W_k for all users and the signals Y are sent from the equalizer to the joint demodulator.

Similar to the joint APP (3.25) in Chapter 3, the proposed joint demodulator obtains the APP for user k as

$$p(X_k(i) = j|Y) \propto \max_{X_k(i)=j, X_1, X_2, \ldots X_{k-1}, X_{k+1}, \ldots, X_K} \exp\left(-\frac{|W_k Y - (\sum_{z=1}^{K} W_k H_z X_z)|^2}{N_o}\right). \tag{6.10}$$

Similar to (6.5), the joint demodulator obtains the LLR for user k as follows.

$$LLR(X_k(i)) = \log\left[\frac{p(X_k(i) = 0|Y)}{p(X_k(i) = 1|Y)}\right]. \tag{6.11}$$

6.3 Simulation results

After introducing the C-V2X physical layer and the receiver design, we have shown that NOMA can be easily implemented on the current C-V2X communications with minor modifications on the receiver. This section aims to evaluate NOMA-based C-V2X communications. The simulation configuration is first introduced, then the simulation results are shown and the three schemes

are evaluated.

6.3.1 Simulation configuration

Following the LTE-V standard, we employ 10 MHz bandwidth and the total number of RBs is 50. QPSK modulation is adopted for TB transmission. The transmitters are assumed to be equipped with a single transmit antenna and the receivers are assumed to be equipped with either single or two receiving antennas. In terms of the radio model, the MIMO multi-path fading model as specified in TS 36.101 [120] and TS 36.104 [121] is adopted. Specifically, the delay profile follows the Extended Vehicular A model (EVA) in [120,121]. The generalized method for exact Doppler spread (GMEDS) in [122] is utilized to model the Rayleigh fading, and the maximum Doppler frequency is 500 Hz. Since this work focuses on random access without power control, all transmitters transmits with the same transmission power and the SNR is defined as the ratio of transmit signal power from each user to the noise power. The transmitted signals from all transmitters undergo independent radio channel. For each user, the summation of the powers of the taps defined in the delay profile follows independent exponential distribution exp(1). When the number of receiving antenna is larger than one, we consider two types of correlations between the transmission antenna and receiving antennas: low or no and high correlations as defined in [120].

6.3.2 Non-orthogonal C-V2X communications with a single receiving antenna

We first consider the single receiving antenna case, the SNR is varied from 0 to 10 dB. The single-user case with OMA receiver is also simulated as a benchmark. In this case, the three receivers are expected to provide the same

performance and the lowest average BLER can be obtained due to interference-free communications. Then, the number of transmitters is increased from two to four, the results are illustrated in Table 6.1.

Table 6.1: Average BLER results with a single receiving antenna.

SNR/dB		0	5	10
1-user	OMA	0.48	0.18	0.05
2-user	OMA	0.74	0.54	0.44
	SIC	0.69	0.37	0.18
	JD	0.60	0.23	0.06
3-user	OMA	0.85	0.74	0.68
	SIC	0.82	0.58	0.40
	JD	0.72	0.35	0.09
4-user	OMA	0.91	0.85	0.82
	SIC	0.90	0.77	0.63
	JD	0.83	0.52	0.22

It can be observed that the JD receiver provides the lowest BLER among the three receivers, followed by the SIC receiver. The gaps among the three receivers increase as the SNR increases. Besides, the gap between the JD receiver and the other receivers ascend when the number of user increases. For the 4-user case at 10 dB SNR, the BLER of the JD receiver is 0.22 while that of the other schemes are higher than 0.6. These results are similar to our analytical results in the previous chapter. JD receiver is the best choice given a large number of transmitters. Comparing the single-user case with OMA receiver and 4-user case with JD receiver, the average BLER difference is lower than 0.2 given high SNR at 10 dB and is higher than 0.3 given 0 dB SNR. This indicates that although NOMA can improve the spectrum efficiency and provides low BLER in the high SNR regime, we should carefully control the number of access users in the low SNR regime to guarantee reasonable BLER for practical applications.

6.3.3 Non-orthogonal C-V2X communications with two receiving antennas

In addition to the single receiving antenna, the two receiving antenna case is simulated. We first consider the high correlation between the two inputs and the simulation results are shown in Table 6.2.

Table 6.2: Average BLER results with two receiving antennas (high correlation).

SNR/dB		0	5	10
1-user	OMA	0.25	0.08	0.03
2-user	OMA	0.57	0.42	0.37
	SIC	0.45	0.20	0.09
	JD	0.35	0.11	0.04
3-user	OMA	0.74	0.66	0.63
	SIC	0.62	0.39	0.27
	JD	0.46	0.15	0.04
4-user	OMA	0.86	0.80	0.78
	SIC	0.79	0.60	0.48
	JD	0.59	0.23	0.05

For the results in Table 6.1 and 6.2, the BLER performances of the three receivers are improved by adopting a larger number of receiving antennas. Generally, the JD receiver still gives the best performance, but the gap between JD and SIC receivers is slightly shortened when the number of access users is lower than four. For instance, the BLER difference of the two receivers in the 2-user case with 5 dB SNR is reduced by 0.05 as compared with the single antenna case. This is because the SIC receiver requires certain power differences among multiple users and multiple receiving antennas increases the probability that the power difference is met. Then, the correlation between the two input is configured as low or no, and the results are shown in Table 6.3. We can observe that performance gap between the SIC and JD receivers is further

shortened given a lower correlation between the two inputs, within which the power difference can be met more easily. This reveals that the performance gap between the SIC and JD receivers can be reduced by employing a larger number of receiving antennas. Given multiple input channels with low correlation, the SIC receiver can provide similar performance as the JD receiver while requiring relatively low computational complexity.

Table 6.3: Average BLER results with two receiving antennas (low correlation).

SNR/dB		0	5	10
1-user	OMA	0.22	0.07	0.02
2-user	OMA	0.43	0.28	0.22
	SIC	0.31	0.10	0.04
	JD	0.27	0.08	0.03
3-user	OMA	0.58	0.46	0.41
	SIC	0.41	0.15	0.06
	JD	0.32	0.09	0.03
4-user	OMA	0.69	0.60	0.57
	SIC	0.51	0.24	0.13
	JD	0.38	0.11	0.03

Comparing the three schemes, the JD-based NOMA receiver provides the best BLER performance at the cost of the highest computational complexity. By contrast, the traditional OMA receiver requires the lowest computational complexity but offers the worst BLER performance. According to the simulation results, the selection of the receiver design depends on the computation capacity of the equipment, the wireless channel state, and the performance requirement.

6.4 Summary

This chapter presents the implementation of NOMA in C-V2X communications as specified in 3GPP Release 14. Based on the PC5 sidelink interface that supports direct communications without forwarding by the eNodeBs, we propose two NOMA receivers for C-V2X communications: SIC-based receiver and JD-based receiver. The two schemes are based on the conventional OMA-based C-V2X receiver with minor modifications. Several interesting points are obtained from the simulation results: 1) the results with a single receiving antenna verify our conclusion in the previous chapter. For example, the JD receiver provides the best performance as compared with OMA and SIC receivers, the performance gap is enlarged as the number of users increases; and 2) the performance gap between the SIC and JD receivers can be reduced by adopting a larger number of receiving antennas, especially when the correlation among multiple inputs is low.

Chapter 7

Conclusion and Future Work

This chapter concludes the main contributions of the thesis and discusses several potential future research directions.

7.1 Conclusion

This thesis exploits the application of NOMA in V2X communications to provide low-latency and reliable communications for time-critical applications in vehicular networks. By allowing multiple users to transmit concurrently, the waiting time caused by scheduling MUA can be significantly reduced. By harnessing the useful information contained in the superimposed signals, NOMA is also expected to improve the transmission success rate, especially for the weak user whose power level is relatively low among others. In this thesis, we focused on two basic V2X communication scenarios which were information exchange in a TWRC and message broadcasting, and that were operated with two NOMA techniques: PNC and MUD. This was a theoretical-plus-practical investigation that considered theoretical performance analysis of non-orthogonal V2X communications and practical NOMA implementation according to the standards including both 802.11p and C-V2X. The general contributions of

this thesis are reiterated as follows:

1. In Chapter 3, an ICI-aware approach was proposed to jointly estimate the channel information, detect the received signals, and perform channel decoding for PNC systems in V2X communications under the negative effect of ICI. The work followed the 802.11p standard and thus OFDM was employed to modulate the transmitted signals. Not only the pilot but also data tones were exploited to improve the channel estimation performance. By taking the ICI caused by CFOs and time-frequency-selective channels into consideration, we converted the channel estimation and detection plus decoding into two optimization problems, and they were addressed by the EM algorithm and the BP algorithm, respectively. The simulation results indicated that: 1) the proposed scheme could converge in five iterations, the computational complexity could be reduced by adopting three iterations with minor performance degradation; 2) the proposed approach yielded lower MSE of estimation results and BER as compared with the benchmarks given five-path double-selectively empirical channels.

2. In Chapter 4, a testbed for non-orthogonal V2X communications was presented. We utilized SDR, which included GNU radio as the software and USRP as the hardware, to implement the NOMA-based transmitters and receivers. The testbed could collect empirical data via vehicle, pedestrian, and infrastructure, to evaluate the proposed algorithms. In the conducted experiment, the TWRC as introduced in Chapter 3 has been achieved by the testbed. Besides the network-coded messages, the individual messages from the two end nodes were decoded with minor modification based on the ICI-aware approach. The empirical results revealed that: 1) the proposed scheme in Chapter 3 yielded higher nor-

malized throughput and lower latency compared with the traditional algorithm, the normalized throughput gap of the network-coded message was around 0.45 and the delay of the conventional scheme was 15 times of that of the proposed approach; 2) The partition that only one user can be decoded occupied around 20% of the normalized throughput, the proposed scheme in Chapter 3 can be used for NOMA to decode the individual messages.

3. In Chapter 5, we have proposed a tractable network model to analyze the theoretical performance of the broadcasting in C-V2X communications operating in mode 4. The model supported the traditional OMA receiver and two NOMA receivers based on SIC and JD techniques. We considered the road intersection scenario that includes both LOS and NLOS communications due to the obstruction of buildings, which was common in the urban areas. The analytical results revealed some interesting points: 1) the JD scheme was the best solution to provide high PDR for applications with high data rate; 2) the SIC scheme needs relatively low computational complexity and provides similar PDR performance as compared with the JD scheme for applications with low data rate; 3) for the communications suffering severe interference and noise, the OMA scheme should be selected due to the lowest complexity and similar performance as the other two schemes; 4) the JD receiver was the best choice given a large number of transmitters; and 5) to satisfy the requirement of applications under diverse situations as discussed from 1) to 4), it is valuable to develop a hybrid protocol for non-orthogonal V2X communications. In addition, a data rate optimization scheme has been presented to maximize the sum goodput from multiple transmitters. The results indicated that the two NOMA schemes provided good fairness among all

transmitters. The OMA scheme can hardly decode the weak users and thus it cannot guarantee good fairness.

4. In Chapter 6, we have exploited the feasibility of implementing NOMA in C-V2X communications. Based on the PC5 sidelink interface that was specified in 3GPP Release 14 for direct communications, we have shown that NOMA can be implemented with minor modifications on the OMA-based C-V2X receivers. Two NOMA receivers based on the SIC and JD techniques were proposed and evaluated. In addition, the proposed receivers supported multiple receiving antennas. According to the simulation results, we found that: 1) given a single receiving antenna, the simulation results further verified our conclusion in Chapter 5. For instance, the JD receiver showed the best performance, followed by the SIC receiver, the OMA receiver provided the highest BLER. Besides, either a larger number of transmitters or a higher SNR increased the performance gaps among the three schemes; 2) compared with the single receiving antenna case, employing a larger number of antennas shortened the performance gap between the SIC and JD receivers, and the gap was further shortened when the correlation among multiple inputs was low.

7.2 Future work

After summarizing the previous work on non-orthogonal V2X communications, several future research directions can be summarized as follows:

1. The proposed network model in Chapter 5 assumes the simple ALOHA protocol in the MAC layer. We plan to include the SPS as specified in the C-V2X standard in our model and investigates the corresponding performance. Furthermore, while cooperating with NOMA, the SPS pro-

tocol can be optimized, such as to discover the optimal reference signal received power (RSRP) threshold to harness the interference.

2. Besides the distributed resource allocation in mode 4, the centralized manner in mode 3 should be exploited for C-V2X communications since it is expected to provide better performance as compared with mode 4. To satisfy the communication requirements of all users, the eNodeB that obtains the information of vehicles within its coverage should consider the channel information between the transmitters and receivers, and carefully control the number of users who share the same resource channel. Based on the proposed network model, we plan to investigate a centralized resource allocation algorithm for non-orthogonal C-V2X communications.

3. Most discussion in this thesis focuses on SISO systems, the MIMO systems should be exploited for non-orthogonal V2X communications. Chapter 6 shows that the two NOMA schemes are significantly enhanced by adopting multiple receiving antennas, especially for the SIC-based receiver. This inspires us to include MIMO in the proposed network model and ICI-aware approach.

Appendices

Appendix A

Proof of Corollary 2

Proof. Since the fast fading follows Rayleigh distribution $h_{T_i} \sim \exp(1)$. For the CDF of the corresponding expected power level can be obtained as follows.

$$Pr(P_{T_i} \geq X_{T_i}) = Pr(h_{T_i} \geq \frac{X_{T_i}}{\overline{P}_{T_i}}) = 1 - \exp(-\frac{X_{T_i}}{\overline{P}_{T_i}}). \tag{A.1}$$

Then we have the PDF of the power level

$$f(X_{T_i}) = Pr(P_{T_i} = X_{T_i}) = \frac{1}{\overline{P}_{T_i}} \exp(-\frac{X_{T_i}}{\overline{P}_{T_i}}). \tag{A.2}$$

According to the inclusion-exclusion principle, the probability of the union of multiple events in Corollary 2 can be written as

$$\begin{aligned}
&\mathcal{P}_{\mathrm{SIC,T_i}}(\Upsilon, x_o) = \mathbb{E}[Pr(\bigcup_{\omega \in \Omega_{T_i}^{SIC}} \mathcal{E}_{\omega}^{SIC})] \\
&= \sum_{\omega \in \Omega_{T_i}^{SIC}} \mathbb{E}[Pr(\mathcal{E}_{\omega}^{SIC})] - \sum_{\omega_1 \in \Omega_{T_i}^{SIC}, \omega_2 \in \Omega_{T_i}^{SIC}, \omega_1 \neq \omega_2} \mathbb{E}[Pr(\mathcal{E}_{\omega_1}^{SIC} \cap \mathcal{E}_{\omega_2}^{SIC})] \\
&+ ... \\
&+ (-1)^{|\Omega_{T_i}^{SIC}|-1} \mathbb{E}[Pr(\bigcap_{\omega \in \Omega_{T_i}^{SIC}} \mathcal{E}_{\omega}^{SIC})],
\end{aligned} \tag{A.3}$$

The principle is also feasible for the JD receiver by simply replacing the set $\Omega_{T_i}^{SIC}$ and event $\mathcal{E}_{\omega}^{SIC}$ with $\Omega_{T_i}^{JD}$ and $\mathcal{E}_{\omega}^{JD}$. For the components without intersection, we assume there are Y users in ω and the corresponding power are denoted by X_{T_y} for user T_y. In addition, the user index y determines the decoding order. Let X_{ω} and $X_{\omega\backslash 1:y}$ denote the sum power of the users in set ω and set $(T_{y+1}, T_{y+2}, ..., T_Y)$. According to Lemma 2, the success probability of event $\mathcal{E}_{\omega}^{SIC}$ is calculated as

$$\begin{aligned}\mathbb{E}[Pr(\mathcal{E}_{\omega}^{SIC})] =&\mathbb{E}[\int_{\beta_{T_Y}N}^{\infty} f(X_{T_Y})dX_{T_Y} \times \int_{\beta_{T_{Y-1}}(N+X_{T_{Y-1}})}^{\infty} f(X_{T_{Y-1}})dX_{T_{Y-1}} \\ &\times ... \\ &\times \int_{\beta_{T_1}(N+X_{\omega\backslash 1})}^{\infty} f(X_{T_1})dX_{T_1}].\end{aligned} \tag{A.4}$$

where $N = N_o + \mathcal{I}_1 + \mathcal{I}_2$ is the interference plus noise. For the integral regarding X_{T_1}, we can easily calculate

$$\int_{\beta_{T_1}(N+X_{\omega\backslash 1})}^{\infty} f(X_{T_1})dX_{T_1} = e^{-\overline{P}_{T_1}^{-1}\beta_{T_1}(N+X_{\omega\backslash 1})}. \tag{A.5}$$

Then for X_{T_2}, we have

$$\begin{aligned}&\int_{\beta_{T_2}(N+X_{\omega\backslash 1:2})}^{\infty} e^{-\overline{P}_{T_1}^{-1}\beta_{T_1}(N+X_{\omega\backslash 1})} f(X_{T_2})dX_{T_2} \\ =&(1+\overline{P}_{T_2}\overline{P}_{T_1}^{-1}\beta_{T_1})^{-1} e^{-(N+X_{\omega\backslash 1:2})(\beta_{T_1}\overline{P}_{T_1}^{-1}+\beta_{T_2}(\overline{P}_{T_2}^{-1}+\beta_{T_1}\overline{P}_{T_1}^{-1}))}.\end{aligned} \tag{A.6}$$

Assuming the integral regarding X_{T_y} is

$$[\prod_{j=1}^{y}(\overline{P}_{T_y}q_{T_y})^{-1}]e^{-(N+X_{\omega\backslash 1:y})(\sum_{j=1}^{y}\beta_{T_y}q_{T_y})}, \tag{A.7}$$

with

$$q_{T_y} = \overline{P}_{T_y}^{-1} + \sum_{j=1}^{y-1} \beta_{T_y} q_{T_y}. \tag{A.8}$$

(A.5) and (A.6) match (A.7) when $y = 1$ and 2, respectively. Assuming (A.7) is feasible for user T_{y-1}, we have the integral of user T_y as follows.

$$\begin{aligned}
&\int_{\beta_{T_y}(N+X_{\omega\setminus 1:y})}^{\infty} [\prod_{j=1}^{y-1} (\overline{P}_{T_j} q_{T_j})^{-1}] e^{-(N+X_{\omega\setminus 1:y-1})(\sum_{j=1}^{y-1} \beta_{T_j} q_{T_j})} \times f(X_{T_y}) dX_{T_y} \\
=&\int_{\beta_{T_y}(N+X_{\omega\setminus 1:y})}^{\infty} [\prod_{j=1}^{y-1} (\overline{P}_{T_j} q_{T_j})^{-1}] e^{-(N+X_{\omega\setminus 1:y})(\sum_{j=1}^{y-1} \beta_{T_j} q_{T_j})} \\
&\times \overline{P}_{T_y}^{-1} e^{-(\overline{P}_{T_y}^{-1} + \sum_{j=1}^{y-1} \beta_{T_j} q_{T_j}) X_{T_y}} dX_{T_y} \\
=&[\prod_{j=1}^{y-1} (\overline{P}_{T_j} q_{T_j})^{-1}] e^{-(N+X_{\omega\setminus 1:y})(\sum_{j=1}^{y-1} \beta_{T_j} q_{T_j})} \times \\
&\overline{P}_{T_y}^{-1} (\overline{P}_{T_y}^{-1} + \sum_{j=1}^{y-1} \beta_{T_j} q_{T_j})^{-1} e^{-(N+X_{\omega\setminus 1:y})\beta_{T_y}(\overline{P}_{T_y}^{-1} + \sum_{j=1}^{y-1} \beta_{T_j} q_{T_j})} \\
=&[\prod_{j=1}^{y} (\overline{P}_{T_j} q_{T_j})^{-1}] e^{-(N+X_{\omega\setminus 1:y})(\sum_{j=1}^{y} \beta_{T_j} q_{T_j})}.
\end{aligned} \tag{A.9}$$

(A.9) matches the assumption of (A.7). Then the final result can be obtained by making $y = Y$.

We now consider the case with S subsets $\mathbb{E}[Pr(\bigcap_{s=1}^{S} \mathcal{E}_{\omega_s}^{SIC})]$. Given $\beta \geq 1$, the first user to be decoded must be the strongest user. Thus, the first element for all subsets must be the same. Otherwise, the corresponding events cannot happen concurrently. Consequently, all subsets must be the same (i.e., elements and the orders are the same), otherwise, the corresponding events cannot occur simultaneously. Therefore, we come to the conclusion that the expectation of the intersection of S subsets $\mathbb{E}[Pr(\bigcap_{s=1}^{S} \mathcal{E}_{\omega_s}^{SIC})]$ is equal to zero. According to the above proof, we have (5.18) and (5.19). □

Appendix B

Proof of Corollary 3

Proof. Similar to (A.3), we apply the inclusion-exclusion principle for the JD decoder.

$$\begin{aligned}
&\mathcal{P}_{\mathrm{JD,T_i}}(\Upsilon, x_o) = \mathbb{E}[Pr(\bigcup_{\omega\in\Omega_{T_i}^{JD}} \mathcal{E}_\omega^{JD})] \\
&= \sum_{\omega\in\Omega_{T_i}^{JD}} \mathbb{E}[Pr(\mathcal{E}_\omega^{JD})] - \sum_{\omega_1\in\Omega_{T_i}^{JD},\omega_2\in\Omega_{T_i}^{JD},\omega_1\neq\omega_2} \mathbb{E}[Pr(\mathcal{E}_{\omega_1}^{JD} \cap \mathcal{E}_{\omega_2}^{JD})] \\
&+ ... \\
&+ (-1)^{|\Omega_{T_i}^{JD}|-1}\mathbb{E}[Pr(\bigcap_{\omega\in\Omega_{T_i}^{JD}} \mathcal{E}_\omega^{JD})].
\end{aligned} \tag{B.1}$$

According to Lemma 3, the success probability of event $\mathcal{E}_\omega^{JD}$ is calculated

as

$$\begin{aligned}
&\mathbb{E}[Pr(\mathcal{E}_{\omega}^{JD})] \\
=&\mathbb{E}[\int_{\beta_{T_Y}N}^{\infty} f(X_{T_Y})dX_Y \int_{\beta_{T_{Y-1}}N}^{\infty} f(X_{T_{Y-1}})dX_{T_{Y-1}}... \\
&\int_{\beta_{T_1}N}^{\infty} f(X_{T_1})dX_{T_1} - \int_{\beta_{T_Y}N}^{N(\beta_\omega - \sum_{j=1}^{Y-1}\beta_{T_j})} f(X_{T_Y})dX_{T_Y} \\
&\times \int_{\beta_{T_{I-1}}N}^{N(\beta_\omega - \sum_{j=1}^{Y-2}\beta_{T_j}) - X_{\omega\setminus 1:Y-1}} f(X_{T_{I-1}})dX_{T_{I-1}}... \\
&\times \int_{\beta_{T_1}N}^{\beta_\omega N - X_{\omega\setminus 1}} f(X_{T_1})dX_{T_1}],
\end{aligned} \tag{B.2}$$

where the positive component denotes the probability that all transmitters satisfy the individual constraints in Lemma 3, and the negative component is for eliminating the probability that the sum power does not meet the requirement regarding the sum rate given that the individual power requirements are satisfied.

For the positive item on the RHS, we have

$$\begin{aligned}
&\int_{\beta_{T_Y}N}^{\infty} f(X_{T_Y})dX_{T_Y} \int_{\beta_{T_{Y-1}}N}^{\infty} f(X_{T_{Y-1}})dX_{T_{Y-1}}... \int_{\beta_{T_1}N}^{\infty} f(X_{T_1})dX_{T_1} \\
=&e^{-N(\sum_{j=1}^{Y}\beta_i\overline{P}_{T_y}^{-1})}.
\end{aligned} \tag{B.3}$$

For the negative item on the RHS, we have the integral of X_{T_1} as follows.

$$\int_{\beta_{T_1}N}^{\beta_\omega N - X_{\omega\setminus 1}} f(X_{T_1})dX_{T_1} = e^{-N\beta_1\overline{P}_{T_1}^{-1}} - e^{-N\beta_\omega\overline{P}_{T_1}^{-1}+\overline{P}_{T_1}^{-1}X_{\omega\setminus 1}}. \tag{B.4}$$

For X_{T_2}, we have

$$\begin{aligned}&\int_{\beta_{T_2}N}^{N(\beta_\omega-\beta_{T_1})-X_{\omega\setminus 1:2}}(e^{-N\beta_1\overline{P}_{T_1}^{-1}}-e^{-N\beta_\omega\overline{P}_{T_1}^{-1}+\overline{P}_{T_1}^{-1}X_{\omega\setminus 1}})\times f(X_{T_2})dX_{T_2}\\ =&e^{-N(\beta_{T_1}\overline{P}_{T_1}^{-1}+\beta_{T_2}\overline{P}_{T_2}^{-1})}-\frac{\overline{P}_{T_2}}{\overline{P}_{T_2}-\overline{P}_{T_1}}e^{-N(\beta_\omega\overline{P}_{T_2}^{-1}+\beta_1(\overline{P}_{T_1}^{-1}-\overline{P}_{T_2}^{-1}))+\overline{P}_{T_2}^{-1}X_{\omega\setminus 2}}\\ &-\frac{\overline{P}_{T_1}}{\overline{P}_{T_1}-\overline{P}_{T_2}}e^{-N(\beta_\omega\overline{P}_{T_1}^{-1}+\beta_2(\overline{P}_{T_2}^{-1}-\overline{P}_{T_1}^{-1}))+\overline{P}_{T_1}^{-1}X_{\omega\setminus 2}}.\end{aligned}\tag{B.5}$$

Assuming that after the integral regarding $X_{T_{y-1}}$, we have

$$\begin{aligned}&e^{-N(\sum_{j=1}^{y-1}\beta_{T_j}\overline{P}_{T_j}^{-1})}-\sum_{j=1}^{y-1}([\prod_{m=1,m\neq j}^{y-1}\frac{\overline{P}_{T_m}^{-1}}{\overline{P}_{T_m}^{-1}-\overline{P}_{T_j}^{-1}}]\\ &\times e^{-N[\beta_\omega\overline{P}_{T_j}^{-1}+\sum_{m=1,m\neq j}^{y-1}\beta_{T_m}(\overline{P}_{T_m}^{-1}-\overline{P}_{T_j}^{-1})]}e^{\overline{P}_{T_j}^{-1}X_{\omega\setminus y-1}}).\end{aligned}\tag{B.6}$$

Applying (B.6), we can obtain that the integral regarding X_{T_y} matches the assumption. Therefore, the assumption stands and we obtain $\mathbb{E}[Pr(\mathcal{E}_\omega^{JD})]$ in (5.21).

For the intersection of S subsets $\mathbb{E}[Pr(\bigcap_{s=1}^{S}\mathcal{E}_{\omega_s}^{JD})]$ with the assumption $\beta\geq 1$, any two subsets ω_i and ω_j cannot occur concurrently when there exists T_a and T_b so that $T_a\in\omega_i, T_a\notin\omega_j$ and $T_b\in\omega_j, T_b\notin\omega_i$. Assuming $|\omega_1|\leq|\omega_2|\leq ...|\omega_{S-1}|\leq|\omega_S|$ without loss of generality, the expectation is not equal zero only when S subsets satisfy $\omega_1\subseteq\omega_2\subseteq ...\omega_{S-1}\subseteq\omega_S$. Let ω_{I_s} denote the intersection of ω_s and ω_{s-1}. For $s=1$, $\omega_{I_1}=\omega_1$. In this case, ω_{I_1} is decoded jointly and other users are regarded as noise. After decoding ω_{I_1}, ω_{I_2} is decoded with the absence of ω_{I_1} and the remaining users are regarded as noise. This is similar to the SIC decoder in Corollary 2. The expectation $\mathbb{E}[Pr(\bigcap_{s=1}^{S}\mathcal{E}_{\omega_s}^{JD})]$ is equal to the probability that all subsets ω_{I_s} are decoded with this strategy.

Assuming that after the integral regarding $\omega_{I_{s-1}}$, we have

$$\sum_{T_{j_1}\in\omega_{I_1}} ... \sum_{T_{j_{s-1}}\in\omega_{I_{s-1}}} a_{T_{j_1}:T_{j_{s-1}}} e^{-b_{T_{j_1}:T_{j_{s-1}}}(N+X_\Omega-\sum_{m=1}^{s-1}X_{\omega_{I_m}})}, \tag{B.7}$$

with

$$\begin{aligned} a_{T_{j_1}:T_{j_{s-1}}} &= \prod_{m=1}^{s-1}\{(\prod_{T_n\in\omega_{I_m}} \frac{\overline{P}_{T_n}^{-1}}{\overline{P}_{T_n}^{-1}+b_{T_{j_1}:T_{j_{m-1}}}}) \times (\prod_{T_l\in\omega_{I_m}\setminus T_{j_m}} \frac{\overline{P}_{T_l}^{-1}+b_{T_{j_1}:T_{j_{m-1}}}}{\overline{P}_{T_l}^{-1}-\overline{P}_{T_{j_m}}^{-1}})\}, \\ b_{T_{j_1}:T_{j_{s-1}}} &= \sum_{m=1}^{s-1}[\beta_{\omega_{I_m}}(\overline{P}_{T_{j_m}}^{-1}+b_{T_{j_1}:T_{j_{m-1}}}) + \sum_{T_n\in\omega_{I_m}} \beta_{T_n}(\overline{P}_{T_n}^{-1}-\overline{P}_{Tj_m}^{-1})]. \end{aligned} \tag{B.8}$$

With the similar method in (A.7), the assumption in (B.7) can be proved. According to the above proof, we have (5.21) and (5.22). □

Bibliography

[1] F. Harry, "Radio warning system for use on vehicles," Dec. 28 1926, US Patent 1,612,427.

[2] M. Gerla and L. Kleinrock, "Vehicular networks and the future of the mobile internet," *Computer Networks*, vol. 55, no. 2, pp. 457–469, 2011.

[3] M. Amadeo, C. Campolo, and A. Molinaro, "Enhancing IEEE 802.11 p/WAVE to provide infotainment applications in VANETs," *Ad Hoc Networks*, vol. 10, no. 2, pp. 253–269, 2012.

[4] R. E. Barone, T. Giuffrè, S. M. Siniscalchi, M. A. Morgano, and G. Tesoriere, "Architecture for parking management in smart cities," *IET Intelligent Transport Systems*, vol. 8, no. 5, pp. 445–452, 2013.

[5] A. Bazzi, B. M. Masini, A. Zanella, and G. Pasolini, "IEEE 802.11 p for cellular offloading in vehicular sensor networks," *Computer Communications*, vol. 60, pp. 97–108, 2015.

[6] C. M. Silva, B. M. Masini, G. Ferrari, and I. Thibault, "A survey on infrastructure-based vehicular networks," *Mobile Information Systems*, vol. 2017, 2017.

[7] "IEEE 1609 family of standards for wireless access in vehicular environments," 2016.

[8] 3rd Generation Partnership Project, "Release 14," *URL http://www.3gpp.org/release-14*, 2016.

[9] G. A. Association, "The Case for Cellular V2X for Safety and Cooperative Driving," *URL http://5gaa.org/pdfs/5GAA-whitepaper-23-Nov-2016.pdf*.

[10] S.-h. Sun, J.-l. Hu, Y. Peng, X.-m. Pan, L. Zhao, and J.-y. Fang, "Support for vehicle-to-everything services based on LTE," *IEEE Wireless Communications*, vol. 23, no. 3, pp. 4–8, 2016.

[11] M. Noor-A-Rahim, G. M. N. Ali, H. Nguyen, and Y. L. Guan, "Performance Analysis of IEEE 802.11 p Safety Message Broadcast With and Without Relaying at Road Intersection," *IEEE Access*, vol. 6, pp. 23 786–23 799, 2018.

[12] I. W.-H. Ho, R. J. North, J. W. Polak, and K. K. Leung, "Effect of transport models on connectivity of interbus communication networks," *Journal of Intelligent Transportation Systems*, vol. 15, no. 3, pp. 161–178, 2011.

[13] S. R. Islam, N. Avazov, O. A. Dobre, and K.-S. Kwak, "Power-domain non-orthogonal multiple access (NOMA) in 5G systems: Potentials and challenges," *IEEE Communications Surveys & Tutorials*, vol. 19, no. 2, pp. 721–742, 2017.

[14] A. Goldsmith, *Wireless communications*. Cambridge university press, 2005.

[15] D. Tse and P. Viswanath, *Fundamentals of wireless communication*. Cambridge university press, 2005.

[16] S. Chen, K. Peng, H. Jin, and J. Song, "Analysis of outage capacity of NOMA: SIC vs. JD," *Tsinghua Science and Technology*, vol. 21, no. 5, pp. 538–543, 2016.

[17] Y. Zhang, K. Peng, J. Song, and Y. Sun, "Channel coding for NOMA schemes with a JD or SIC receiver," *2017 13th International Wireless Communications and Mobile Computing Conference (IWCMC)*, pp. 1599–1603, 2017.

[18] Z. Wang, J. Huang, S. Zhou, and Z. Wang, "Iterative receiver processing for OFDM modulated physical-layer network coding in underwater acoustic channels," *IEEE Transactions on Communications*, vol. 61, no. 2, pp. 541–553, 2013.

[19] H. Pan, L. Lu, and S. C. Liew, "Network-Coded Multiple Access with High-Order Modulations," *IEEE Transactions on Vehicular Technology*, vol. 66, no. 11, pp. 9776–9792, 2017.

[20] T. Koike-Akino, P. Popovski, and V. Tarokh, "Optimized constellations for two-way wireless relaying with physical network coding," *IEEE Journal on Selected Areas in Communications*, vol. 27, no. 5, 2009.

[21] Z. Zhao, X. Cheng, M. Wen, B. Jiao, and C.-X. Wang, "Channel estimation schemes for IEEE 802.11p standard," *IEEE intelligent transportation systems magazine*, vol. 5, no. 4, pp. 38–49, October 2013.

[22] L. Lu, T. Wang, S. C. Liew, and S. Zhang, "Implementation of physical-layer network coding," *Physical Communication*, vol. 6, pp. 74–87, 2013.

[23] Z. Tang, R. C. Cannizzaro, G. Leus, and P. Banelli, "Pilot-assisted time-varying channel estimation for OFDM systems," *IEEE Transactions on Signal Processing*, vol. 55, no. 5, pp. 2226–2238, 2007.

[24] G. B. Giannakis and C. Tepedelenlioglu, "Basis expansion models and diversity techniques for blind identification and equalization of time-varying channels," *Proceedings of the IEEE*, vol. 86, no. 10, pp. 1969–1986, 1998.

[25] M. K. Tsatsanis and G. B. Giannakis, "Modelling and equalization of rapidly fading channels," *International journal of adaptive control and signal processing*, vol. 10, no. 2-3, pp. 159–176, 1996.

[26] K. Teo, S. Ohno, and T. Hinamoto, "Kalman channel estimation based on oversampled polynomial model for OFDM over doubly-selective channels," *IEEE 6th Workshop on Signal Processing Advances in Wireless Communications, 2005.*, pp. 116–120, 2005.

[27] H. Hijazi and L. Ros, "Joint data QR-detection and Kalman estimation for OFDM time-varying Rayleigh channel complex gains," *IEEE Transactions on Communications*, vol. 58, no. 1, pp. 170–178, 2010.

[28] M. Visintin, "Karhunen-Loève expansion of a fast Rayleigh fading process," *Electronics Letters*, vol. 32, no. 18, pp. 1712–1713, 1996.

[29] T. Zemen and C. F. Mecklenbrauker, "Time-variant channel equalization via discrete prolate spheroidal sequences," *The Thrity-Seventh Asilomar Conference on Signals, Systems & Computers, 2003*, vol. 2, pp. 1288–1292, 2003.

[30] A. P. Dempster, N. M. Laird, and D. B. Rubin, "Maximum likelihood from incomplete data via the EM algorithm," *Journal of the Royal Statistical Society: Series B (Methodological)*, vol. 39, no. 1, pp. 1–22, 1977.

[31] M. R. Gupta, Y. Chen *et al.*, "Theory and use of the EM algorithm," *Foundations and Trends® in Signal Processing*, vol. 4, no. 3, pp. 223–296, 2011.

[32] F. R. Kschischang, B. J. Frey, and H.-A. Loeliger, "Factor graphs and the sum-product algorithm," *IEEE Transactions on information theory*, vol. 47, no. 2, pp. 498–519, 2001.

[33] J. S. Yedidia, W. T. Freeman, and Y. Weiss, "Understanding belief propagation and its generalizations," *Exploring artificial intelligence in the new millennium*, vol. 8, pp. 236–239, 2003.

[34] R. Molina-Masegosa and J. Gozalvez, "LTE-V for sidelink 5G V2X vehicular communications: a new 5G technology for short-range vehicle-to-everything communications," *IEEE Vehicular Technology Magazine*, vol. 12, no. 4, pp. 30–39, 2017.

[35] B. Di, L. Song, and Y. Li, "Sub-channel assignment, power allocation, and user scheduling for non-orthogonal multiple access networks," *IEEE Transactions on Wireless Communications*, vol. 15, no. 11, pp. 7686–7698, 2016.

[36] S. Guo and X. Zhou, "Robust power allocation for NOMA in heterogeneous vehicular communications with imperfect channel estimation," *Personal, Indoor, and Mobile Radio Communications (PIMRC), 2017 IEEE 28th Annual International Symposium on*, pp. 1–5, 2017.

[37] J. Zhao, Y. Liu, K. K. Chai, Y. Chen, and M. Elkashlan, "Joint subchannel and power allocation for NOMA enhanced D2D communications," *IEEE Transactions on Communications*, vol. 65, no. 11, pp. 5081–5094, 2017.

[38] B. Di, L. Song, Y. Li, and Z. Han, "V2X Meets NOMA: Non-Orthogonal Multiple Access for 5G-Enabled Vehicular Networks," *IEEE Wireless Communications*, vol. 24, no. 6, pp. 14–21, 2017.

[39] L. Qian, Y. Wu, H. Zhou, and S. Shen, "Dynamic cell association for non-orthogonal multiple-access V2S networks," *IEEE J. Sel. Areas Commun*, vol. 35, no. 10, pp. 2342–2356, 2017.

[40] J. Mitola, "Software radios: Survey, critical evaluation and future directions," *IEEE Aerospace and Electronic Systems Magazine*, vol. 8, no. 4, pp. 25–36, 1993.

[41] M. Ettus, "Universal software radio peripheral," *URL http://www.ettus.com*.

[42] M. I. Hassan, H. L. Vu, and T. Sakurai, "Performance analysis of the IEEE 802.11 MAC protocol for DSRC safety applications," *IEEE Transactions on vehicular technology*, vol. 60, no. 8, pp. 3882–3896, 2011.

[43] E. ETSI, "302 637-2 V1. 3.1-Intelligent Transport Systems (ITS); Vehicular Communications; Basic Set of Applications; Part 2: Specification of Cooperative Awareness Basic Service," *ETSI, Sept*, 2014.

[44] J. B. Kenney, "Dedicated short-range communications (DSRC) standards in the United States," *Proceedings of the IEEE*, vol. 99, no. 7, pp. 1162–1182, 2011.

[45] C. Perkins, E. Belding-Royer, and S. Das, "Ad hoc on-demand distance vector (AODV) routing," Tech. Rep., 2003.

[46] T. M. Cover and J. A. Thomas, *Elements of information theory*. John Wiley & Sons, 2012.

[47] J.-B. Kim and I.-H. Lee, "Non-orthogonal multiple access in coordinated direct and relay transmission," *IEEE Communications Letters*, vol. 19, no. 11, pp. 2037–2040, 2015.

[48] S. Timotheou and I. Krikidis, "Fairness for non-orthogonal multiple access in 5G systems," *IEEE Signal Processing Letters*, vol. 22, no. 10, pp. 1647–1651, 2015.

[49] B. Di, L. Song, Y. Li, and G. Y. Li, "Non-orthogonal multiple access for high-reliable and low-latency V2X communications in 5G systems," *IEEE Journal on Selected Areas in Communications*, vol. 35, no. 10, pp. 2383–2397, 2017.

[50] Z. Ding, F. Adachi, and H. V. Poor, "The application of MIMO to non-orthogonal multiple access," *IEEE Transactions on Wireless Communications*, vol. 15, no. 1, pp. 537–552, 2015.

[51] Y. Lan, A. Benjebboiu, X. Chen, A. Li, and H. Jiang, "Considerations on downlink non-orthogonal multiple access (NOMA) combined with closed-loop SU-MIMO," *2014 8th International Conference on Signal Processing and Communication Systems (ICSPCS)*, pp. 1–5, 2014.

[52] M. Zeng, A. Yadav, O. A. Dobre, G. I. Tsiropoulos, and H. V. Poor, "On the sum rate of MIMO-NOMA and MIMO-OMA systems," *IEEE Wireless Communications Letters*, vol. 6, no. 4, pp. 534–537, 2017.

[53] ——, "Capacity comparison between MIMO-NOMA and MIMO-OMA with multiple users in a cluster," *IEEE Journal on Selected Areas in Communications*, vol. 35, no. 10, pp. 2413–2424, 2017.

[54] "TP for Classification of MUST Schemes," *document R1-154999*, 2015.

[55] A. Benjebbour, Y. Saito, Y. Kishiyama, A. Li, A. Harada, and T. Nakamura, "Concept and practical considerations of non-orthogonal multiple access (NOMA) for future radio access," *2013 International Symposium on Intelligent Signal Processing and Communication Systems*, pp. 770–774, 2013.

[56] S. Zhang, S. C. Liew, and P. P. Lam, "Hot Topic: Physical-layer Network Coding," *Proceedings of the 12th Annual International Conference on Mobile Computing and Networking*, pp. 358–365, 2006.

[57] L. F. Xie, I. W.-H. Ho, Z. H. Situ, L. Lu, and W. Lu, "Channel-Coded Physical-Layer Network Coding With OFDM Modulation," *IEEE Access*, vol. 6, pp. 22 267–22 280, 2018.

[58] Y. Zou, J. Zhu, X. Wang, and V. C. Leung, "Improving physical-layer security in wireless communications using diversity techniques," *IEEE Network*, vol. 29, no. 1, pp. 42–48, 2015.

[59] P. Popovski and H. Yomo, "The anti-packets can increase the achievable throughput of a wireless multi-hop network," *Communications, 2006. ICC'06. IEEE International Conference on*, vol. 9, pp. 3885–3890, 2006.

[60] R. Ahlswede, N. Cai, S.-Y. Li, and R. W. Yeung, "Network information flow," *IEEE Transactions on information theory*, vol. 46, no. 4, pp. 1204–1216, 2000.

[61] S.-Y. Li, R. W. Yeung, and N. Cai, "Linear network coding," *IEEE transactions on information theory*, vol. 49, no. 2, pp. 371–381, 2003.

[62] S. Katti, S. Gollakota, and D. Katabi, "Embracing wireless interference: Analog network coding," *ACM SIGCOMM Computer Communication Review*, vol. 37, no. 4, pp. 397–408, 2007.

[63] J. He and S.-C. Liew, "Building blocks of physical-layer network coding," *IEEE Transactions on Wireless Communications*, vol. 14, no. 5, pp. 2711–2728, 2015.

[64] E. D. N. Ndih and S. Cherkaoui, "Reliable broadcasting in VANETs using physical-layer network coding," *2012 International Conference on Communications and Information Technology (ICCIT)*, pp. 363–368, 2012.

[65] Ndih, Eugène David Ngangue and Cherkaoui, Soumaya, "Mac for Physical-Layer Network Coding in VANETs," *International Journal of Business Data Communications and Networking (IJBDCN)*, vol. 8, no. 4, pp. 84–106, 2012.

[66] I. W.-H. Ho, S. C. Liew, and L. Lu, "Feasibility study of physical-layer network coding in 802.11 p VANETs," *2014 IEEE International Symposium on Information Theory*, pp. 646–650, 2014.

[67] F. Rossetto and M. Zorzi, "On the design of practical asynchronous physical layer network coding," *2009 IEEE 10th Workshop on Signal Processing Advances in Wireless Communications*, pp. 469–473, 2009.

[68] H. Yan and H. H. Nguyen, "Adaptive physical-layer network coding in two-way relaying with OFDM," *2013 IEEE Global Communications Conference (GLOBECOM)*, pp. 4244–4249, 2013.

[69] L. Lu and S. C. Liew, "Asynchronous physical-layer network coding," *IEEE Transactions on Wireless Communications*, vol. 11, no. 2, pp. 819–831, 2011.

[70] D. Wübben, "Joint channel decoding and physical-layer network coding in two-way QPSK relay systems by a generalized sum-product algo-

rithm," *2010 7th International Symposium on Wireless Communication Systems*, pp. 576–580, 2010.

[71] F. Nyongesa, K. Djouani, T. Olwal, and Y. Hamam, "Doppler shift compensation schemes in VANETs," *Mobile Information Systems*, vol. 2015, 2015.

[72] T. Zemen and A. F. Molisch, "Adaptive reduced-rank estimation of non-stationary time-variant channels using subspace selection," *IEEE Transactions on Vehicular Technology*, vol. 61, no. 9, pp. 4042–4056, 2012.

[73] W. C. Jakes and D. C. Cox, *Microwave mobile communications*. Wiley-IEEE Press, 1994.

[74] S. Lin, Z. Zhong, L. Cai, and Y. Luo, "Finite state Markov modelling for high speed railway wireless communication channel," *2012 IEEE Global Communications Conference (GLOBECOM)*, pp. 5421–5426, 2012.

[75] B. Yang, K. B. Letaief, R. S. Cheng, and Z. Cao, "Channel estimation for OFDM transmission in multipath fading channels based on parametric channel modeling," *IEEE transactions on communications*, vol. 49, no. 3, pp. 467–479, 2001.

[76] E. P. Simon, L. Ros, H. Hijazi, and M. Ghogho, "Joint carrier frequency offset and channel estimation for OFDM systems via the EM algorithm in the presence of very high mobility," *IEEE Transactions on Signal Processing*, vol. 60, no. 2, pp. 754–765, 2012.

[77] L. Bernadó, T. Zemen, F. Tufvesson, A. F. Molisch, and C. F. Mecklenbräuker, "Delay and Doppler spreads of nonstationary vehicular channels for safety-relevant scenarios," *IEEE Transactions on Vehicular Technology*, vol. 63, no. 1, pp. 82–93, 2014.

[78] T. Wang and S. C. Liew, "Joint channel estimation and channel decoding in physical-layer network coding systems: An EM-BP factor graph framework," *IEEE Transactions on Wireless Communications*, vol. 13, no. 4, pp. 2229–2245, 2014.

[79] C. C. Tan and N. C. Beaulieu, "On first-order Markov modeling for the Rayleigh fading channel," *IEEE Transactions on Communications*, vol. 48, no. 12, pp. 2032–2040, 2000.

[80] X. Liao, L. Fan, and F. Gao, "Blind channel estimation for OFDM modulated two-way relay network," *2010 IEEE Wireless Communication and Networking Conference*, pp. 1–5, 2010.

[81] Y. Tan, S. C. Liew, and T. Huang, "Mobile Lattice-Coded Physical-Layer Network Coding With Practical Channel Alignment," *IEEE Transactions on Mobile Computing*, vol. 17, no. 8, pp. 1908–1923, 2018.

[82] M. Wu, F. Ludwig, M. Woltering, D. Wübben, A. Dekorsy, and S. Paul, "Analysis and implementation for physical-layer network coding with carrier frequency offset," *Smart Antennas (WSA), 2014 18th International ITG Workshop on*, pp. 1–8, 2014.

[83] M. Woltering, D. Wubben, and A. Dekorsy, "Physical layer network coding with gaussian waveforms using soft interference cancellation," *Vehicular Technology Conference (VTC Spring), 2015 IEEE 81st*, pp. 1–5, 2015.

[84] L. F. Xie, I. W. H. Ho, S. C. Liew, L. Lu, and F. C. M. Lau, "The Feasibility of Mobile Physical-Layer Network Coding with BPSK Modulation," *IEEE Transactions on Vehicular Technology*, vol. 66, no. 5, pp. 3976–3990, May 2017.

[85] T. Wang, S. C. Liew, and L. You, "Joint phase tracking and channel decoding for OFDM PNC: Algorithm and experimental evaluation," *Proceedings of the 2014 ACM workshop on Software radio implementation forum*, pp. 69–76, 2014.

[86] J. Choi, "NOMA-based random access with multichannel ALOHA," *IEEE Journal on Selected Areas in Communications*, vol. 35, no. 12, pp. 2736–2743, 2017.

[87] J. B. Seo, B. C. Jung, and H. Jin, "Non-Orthogonal Random Access for 5G Mobile Communication Systems," *IEEE Transactions on Vehicular Technology*, vol. 67, no. 8, pp. 7867–7871, 2018.

[88] J.-B. Seo, B. C. Jung, and H. Jin, "Performance Analysis of NOMA Random Access," *IEEE Communications Letters*, vol. 22, no. 11, pp. 2242–2245, 2018.

[89] Y. Li and L. Dai, "Maximum sum rate of slotted Aloha with successive interference cancellation," *IEEE Transactions on Communications*, vol. 66, no. 11, pp. 5385–5400, 2018.

[90] Y. Zhang, K. Peng, Z. Chen, and J. Song, "SIC vs. JD: Uplink NOMA techniques for M2M random access," *Communications (ICC), 2017 IEEE International Conference on*, pp. 1–6, 2017.

[91] W. Yue, "The effect of capture on performance of multichannel slotted ALOHA systems," *IEEE Transactions on Communications*, vol. 39, no. 6, pp. 818–822, 1991.

[92] D. Shen and V. O. Li, "Performance analysis for a stabilized multichannel slotted ALOHA algorithm," *14th IEEE Proceedings on Personal,*

Indoor and Mobile Radio Communications, 2003. PIMRC 2003., vol. 1, pp. 249–253, 2003.

[93] T. Yoon, T. H. Nguyen, X. T. Nguyen, D. Yoo, B. Jang *et al.*, "Resource allocation for NOMA-based D2D systems coexisting with cellular networks," *IEEE Access*, vol. 6, pp. 66 293–66 304, 2018.

[94] Y. Xu and X. Gu, "Resource Allocation for NOMA-based V2V System," *2018 International Conference on Network Infrastructure and Digital Content (IC-NIDC)*, pp. 239–243, 2018.

[95] S. Guo and X. Zhou, "Robust Resource Allocation With Imperfect Channel Estimation in NOMA-Based Heterogeneous Vehicular Networks," *IEEE Transactions on Communications*, vol. 67, no. 3, pp. 2321–2332, 2018.

[96] H. Zheng, H. Li, S. Hou, and Z. Song, "Joint resource allocation with weighted max-min fairness for NOMA-enabled V2X communications," *IEEE Access*, vol. 6, pp. 65 449–65 462, 2018.

[97] Y. Chen, L. Wang, Y. Ai, B. Jiao, and L. Hanzo, "Performance analysis of NOMA-SM in vehicle-to-vehicle massive MIMO channels," *IEEE Journal on Selected Areas in Communications*, vol. 35, no. 12, pp. 2653–2666, 2017.

[98] Y. A. Chau and S.-H. Yu, "Space modulation on wireless fading channels," vol. 3, pp. 1668–1671, 2001.

[99] D. Zhang, Y. Liu, L. Dai, A. K. Bashir, A. Nallanathan, and B. Shim, "Performance Analysis of FD-NOMA-based Decentralized V2X Systems," *IEEE Transactions on Communications*, vol. 67, no. 7, pp. 5024–5036, 2019.

[100] A. F. Molisch, F. Tufvesson, J. Karedal, and C. F. Mecklenbrauker, "A survey on vehicle-to-vehicle propagation channels," *IEEE Wireless Communications*, vol. 16, no. 6, pp. 12–22, 2009.

[101] M. A. Ingram, "Six time-and frequency-selective empirical channel models for vehicular wireless LANs," *IEEE Vehicular Technology Magazine*, vol. 2, no. 4, pp. 4–11, 2007.

[102] M. Pätzold, M. Patzold, and M. Paetzold, *Mobile fading channels*. Wiley Online Library, 2002, vol. 14.

[103] Y. Li and L. J. Cimini, "Bounds on the interchannel interference of OFDM in time-varying impairments," *IEEE Transactions on Communications*, vol. 49, no. 3, pp. 401–404, 2001.

[104] H. Hijazi and L. Ros, "Polynomial estimation of time-varying multipath gains with intercarrier interference mitigation in OFDM systems," *IEEE Transactions on Vehicular Technology*, vol. 58, no. 1, pp. 140–151, 2009.

[105] B. Zhou and Q. Chen, "A tutorial on Minimum Mean Square Error Estimation," 2015.

[106] H.-A. Loeliger, J. Dauwels, J. Hu, S. Korl, L. Ping, and F. R. Kschischang, "The factor graph approach to model-based signal processing," *Proceedings of the IEEE*, vol. 95, no. 6, pp. 1295–1322, 2007.

[107] S. C. Liew, S. Zhang, and L. Lu, "Physical-layer network coding: Tutorial, survey, and beyond," *Physical Communication*, vol. 6, pp. 4–42, 2013.

[108] S. Coleri, M. Ergen, A. Puri, and A. Bahai, "Channel estimation techniques based on pilot arrangement in OFDM systems," *IEEE Transactions on broadcasting*, vol. 48, no. 3, pp. 223–229, 2002.

[109] "GNU Software Radio project," available at http://www.gnu.org/software/gnuradio/.

[110] T. M. Schmidl and D. C. Cox, "Robust frequency and timing synchronization for OFDM," *IEEE transactions on communications*, vol. 45, no. 12, pp. 1613–1621, 1997.

[111] Y. Saito, Y. Kishiyama, A. Benjebbour, T. Nakamura, A. Li, and K. Higuchi, "Non-orthogonal multiple access (NOMA) for cellular future radio access," *Vehicular Technology Conference (VTC Spring), 2013 IEEE 77th*, pp. 1–5, 2013.

[112] J. G. Andrews, F. Baccelli, and R. K. Ganti, "A tractable approach to coverage and rate in cellular networks," *IEEE Transactions on communications*, vol. 59, no. 11, pp. 3122–3134, 2011.

[113] Z. Tong, H. Lu, M. Haenggi, and C. Poellabauer, "A Stochastic Geometry Approach to the Modeling of DSRC for Vehicular Safety Communication," *IEEE Trans. Intelligent Transportation Systems*, vol. 17, no. 5, pp. 1448–1458, 2016.

[114] M. N. Sial, Y. Deng, J. Ahmed, A. Nallanathan, and M. Dohler, "Stochastic Geometry Modeling of Cellular V2X Communication over Shared Channels," *IEEE Transactions on Vehicular Technology (Early Access)*, 2019.

[115] I. S. Gradshteyn and I. M. Ryzhik, *Table of integrals, series, and products*. Academic press, 2014.

[116] G. E. Forsythe, C. B. Moler, and M. A. Malcolm, "Computer methods for mathematical computations," 1977.

[117] H. Fernández, L. Rubio, V. M. Rodrigo-Peñarrocha, and J. Reig, "Path loss characterization for vehicular communications at 700 MHz and 5.9 GHz under LOS and NLOS conditions," *IEEE Antennas and Wireless Propagation Letters*, vol. 13, pp. 931–934, 2014.

[118] H. S. Dhillon, H. Huang, H. Viswanathan, and R. A. Valenzuela, "Fundamentals of throughput maximization with random arrivals for M2M communications," *IEEE Transactions on Communications*, vol. 62, no. 11, pp. 4094–4109, 2014.

[119] M. A. Javed, D. T. Ngo, and J. Y. Khan, "Distributed spatial reuse distance control for basic safety messages in SDMA-based VANETs," *Vehicular Communications*, vol. 2, no. 1, pp. 27–35, 2015.

[120] 3GPP TS 36.101, "Evolved Universal Terrestrial Radio Access (E-UTRA); User Equipment (UE) Radio Transmission and Reception," *3rd Generation Partnership Project; Technical Specification Group Radio Access Network*.

[121] 3GPP TS 36.104, "Evolved Universal Terrestrial Radio Access (E-UTRA); Base Station (BS) Radio Transmission and Receptionn," *3rd Generation Partnership Project; Technical Specification Group Radio Access Network*.

[122] M. Patzold, C.-X. Wang, and B. O. Hogstad, "Two new sum-of-sinusoids-based methods for the efficient generation of multiple uncorrelated Rayleigh fading waveforms," *IEEE Transactions on Wireless Communications*, vol. 8, no. 6, pp. 3122–3131, 2009.